First-principles study of the phase diagram of Potassium

Giulia Boucher

A thesis submitted in partial fulfillment
of the requirements for the degree of
Doctor of Engineering
of
University College London

Department of Chemistry

August, 2018

I, Giulia Boucher, confirm that the work presented in this thesis is my own. Where information has been derived from other sources, I confirm that this has been indicated in the thesis.

Abstract

This thesis is a computer simulation project to calculate the phase diagram of potassium as a function of pressure from 0 to 100 GPa and temperature from 0 to 1200 K. The project required the application of both electronic structure techniques and classical molecular dynamics simulations to compute the free energies of solid and liquid phases. To compute the melting properties, the coexistence was used, either with a classical potential fitted to the *ab initio* data or directly with the *ab initio* potential. Tests were also carried out using the Z method, however, this method cannot compute melting properties but can provide an estimate of the upper bound of the melting temperature. The phase transitions of the solid structures of potassium were determined from 0 to 100 GPa at temperatures ranging from 0 to 450K using first-principles calculations of the free energies. The calculations were carried out within the density functional theory framework with the generalised gradient approximation and the projector augmented wave method as implemented in VASP. The quasi-harmonic contribution to the free energy of the solids was calculated using the small displacement method. To determine the melting temperature of each solid phase of potassium, the coexistence method with a potential was used but proved unsuccessful for most phases. Therefore, the direct coexistence was used but was deemed computationally too expensive. As aforementionned, the Z method was tested in order to obtain an approximation of

the melting temperature and assess the performance of the method.

Acknowledgements

This thesis could not have been possible without the financial support of the Atomic Weapon Establishment. I am especially indebted to Dr. Shailesh Mehta. I would also like to thank my supervisor Prof. Dario Alfè for his continous support, patience and immense knowledge.

I am grateful to all of those with whom I have had the pleasure to work with from both the Earth Sciences and Chemistry Departments. I would also like to thank all the members of staff at UCL. My sincere thanks also go to Dr. David Scanlon, Prof. Ian Wood and Prof. Lidunka Vočadlo for their support, guidance and insightful comments.Thanks also go to all the students of the Center for Doctoral Training in Molecular Modelling and Materials Science who have made my experience enjoyable.

I would also like to thank my parents whose love and continued encouragements are invaluable in all my life's endeavors. I am beholden to them for their patience and supporting me through all the ups and downs of my research. Finally, but in no means least, thanks also to my loving, supportive and patient partner whose moral support during the final stages of my research is greatly appreciated.

Rien ne donne l'assurance que la vérité ; rien ne donne le repos que la recherche sincère de la vérité

Pascal, Pensées (1670)

Contents

List of Figures

List of Tables

1 Introduction

High pressure and temperature studies of elements are of great interest given the various possible applications such as those in geophysics and astrophysics. For instance when bombarded by neutrons the stable isotopes of lithium (Li) produce tritium, which can then used in deuterium-tritium fuel; sodium (Na) is being used in vapor lamps; rubidium (Rb) and cesium (Cs) are produced when the nuclei of heavy elements in stars capture free neutrons and francium (Fr) is synthesized in supernovae. Potassium (K) is present in meteorites, stars and dust in the interstellar medium. Brown dwarfs are also known to have an excess of K in their atmospheres at temperatures ranging from 600 to 3000K [1]. The study of the phase diagram of K also presents interest in two other fields. First, this thesis was sponsored by the Atomic Weapon Establishment (AWE). Since the UK signed the Comprehensive Test Ban Treaty in 1996 all nuclear testing ended thus rendering computer simulations invaluable to insure the safety and predictability of the UK's nuclear deterrent. Indeed, the AWE relies on these computer simulations to be able to predict how systems will react under extreme conditions. This study therefore can contribute to benchmarking computational methods for the AWE.Second, a potential application of this study is Geophysics. The Earth's magnetic field is generated from the liquid outer core composed of iron and other impurities and spans about 2400 km. The magnetic field, which protects the Earth from solar winds, is constantly changing but recently has shown signs of weakening. ESA launched the Swarm Mission in 2013 to study the weakening of the magnetic field. The geodynamo mechanism which produces the magnetic field relies on convective currents. One of the many energy sources of the liquid outer core is ra-

diogenic heating which is thought to be due to potassium [2], uranium and thorium. Both experiments and *ab initio* calculations have shown that at high temperature and pressure, potassium and iron form a liquid solution [3, 4]. The understanding of the Earth's magnetic field therefore relies on our better understanding of these energy sources and hence determining the amount of potassium in the core. The phase diagram of potassium will give a first insight into the conditions under which it is stable.

There is a consensus that at ambient conditions the alkali metals are well described by the nearly free electron model (see for e.g. [5]). Under these conditions alkali metals crystallize in the body-centered cubic structure (bcc) with lattice parameters $a = 3.5091$ Å (Li), $a = 4.2906$ Å (Na), $a = 5.703$ Å (Rb) and $a = 6.141$ Å (Cs) at room temperature [6]. Upon compression they transform into a face-centered cubic structure (fcc) with lattice parameters $a = 3.9$ Å at 8 GPa (Li), $a = 3.5348$ Å at 85.6 GPa (Na), $a = 5.224$ Å at 11.9 GPa (Rb) and $a = 5.984$ Å at 4.1 GPa (Cs) [6]. Alhough the group I elements are considered as simple metals due to the fact that they only have one electron in the conduction band, upon further pressure increase there is a departure from the nearly free electron model as the alkali metals transform into open and complex structures as seen in Figure 1. It is clear from Figure 1 that K shares atomic arrangements with both the lighter Na and the heavier Rb but also has unique features especially the post-fcc phase, which is not a distortion of the bcc structure as Na and Rb but a composite one (a hexagonal hP4 structure has also been observed at these pressures).

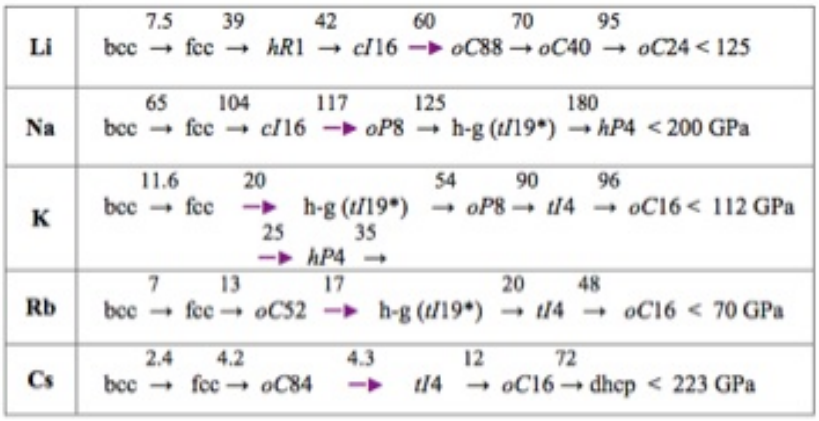

Figure 1: Sequences of phase transformations upon pressure increase of the alkali metals. The crystal structures are denoted by the Pearson symbols except for bcc and fcc defined above. h-g stands for host-guest and * stands for the rounding up of the non-integer number of atoms. Bold arrows stand for supposed core ionization. Numbers above the arrows specify the transition pressures in GPa.*Figure taken from [7]*

Experimentally, K has been studied up to 112 GPa at 0 K, where the volume is 0.15 of the initial atomic volume making it the largest compression amongst elements [7]. This large compression stems from the fact that the larger the element's volume at ambient conditions the higher the compressibility and Figure 2 shows how much larger the volume of K at ambient pressure is compared to other elements. Furthermore, compression leads to changes in the electronic structure making the electron levels overlap. The latter has been used to explain the structural peculiarities of K aforementioned - the $3d$ electron band in K is just above the valence band $4s$ and hence under pressure there is an $s - d$ transition whereas for the heavier Rb the d levels are in their cores so the transitions start at a lower pressure and the fcc phase of the lighter Na is stable until a much higher pressure as the $3d$ level is much further away from its $3s$ valence band.

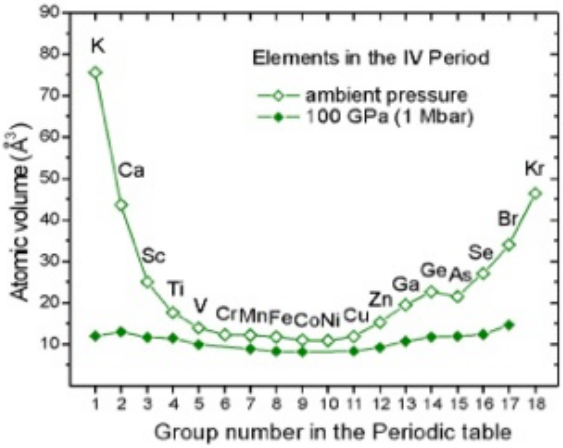

Figure 2: Atomic volumes with respect to the group number for the elements in the IV period at two pressures which shows that K has a very large compressibility. *Figure taken from [7]*

1.1 bcc phase

Experiments (see for e.g, [8], [9], [10]) have shown that K adopts a bcc structure at ambient conditions with lattice parameter $a = 5.32$ Å [11]. Various calculations have also been carried out in order to determine the structural properties of the bcc phase of K and a summary of those are given in Table 1.

Table 1: Structural properties for bcc K at T=0K determined by *ab initio* calculations

a (Å)	B_0 (GPa)	Method [Reference]
5.29	3.68	Full-potential linear augmented plane-wave [12]
5.22	4.30	Pseudopotential plane-wave [12]
5.30	6.08	Projector augmented wave method [12]
5.03	5.4	Full potential linearized augmented plane-wave [13]
5.04	4.8	LDA [14]
5.27	3.6	GGA PBE [14]
5.10	4.3	Pseudopotential method [15]
5.05	4.7	Augmented plane-wave with LDA [16]
5.33	**2.96**	**Experimental x-ray diffraction [10]**

Upon compression the bcc structure transforms into a fcc one at about 11 GPa [8]. These results have also been confirmed by *ab initio* studies (e.g, [17] found the transition pressure to be at 11.6 GPa using a full-potential linear muffin-tin orbital method [18] and the generalised-gradient approximation (GGA PBE) [19])

Xie et al. [12] studied the electronic structure, lattice dynamics and elastic constants of the bcc phases of the alkali metals in order to examine the

mechanisms responsible for the phase transition to fcc, which was previously explained mainly by electronic structure studies [20]. The calculations of Xie et al. [12] were conducted within the framework of the density-functional theory (DFT) [21] with the electron-correlation described by the GGA PBE. The full-potential linear augmented plane-wave method was adopted along with 32 768 k-points to determine the energies, density of states (DOS) and Fermi surfaces (FS). For the lattice dynamics calculation they employed two methods: first, the linear response method within the density functional perturbation theory via the pseudopotential plane-wave method with a kinetic energy cutoff of 80 Ry and a 20x20x20 Monkhorst-Pack grid; second, the direct 4x4x4 supercell calculation with 64 atoms where the electron-ion interaction was expressed via the projector augmented wave (PAW) method [22] and the plane-wave cutoff was of 800 eV. Their results for the 3D FS are shown in Figure 3, from which it can be seen that at ambient pressure, the nearly free electron model is indeed valid given the spherical nature of the FS. At 10 GPa the FS starts touching the Brillouin Zone (BZ) at the point N. At the same point it was shown that there was an increase of the optical conductivity under pressure increase, attributed to the formation of nearly parallel bands near the point N [20]. Figure 3 also shows that at 15 GPa there are increased necks along the ΓN direction, which was described by Degtyareva [23] as the indication of a Hume-Rothery effect where, when the planes of the BZ form near the Fermi level, it allows a pseudogap to open thus reducing the overall electronic energy.

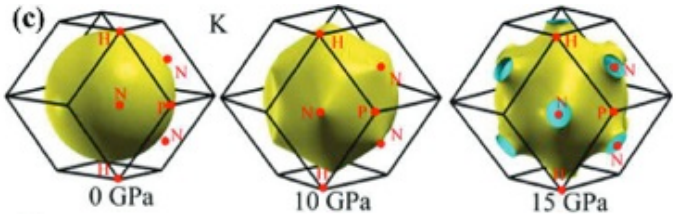

Figure 3: FS of bcc K at 0, 10 and 15 GPa. This Figure shows that at 0 GPa the FS is spherical and thus represents well the nearly free electron model, however, at 15 GPa it is no longer spherical which indicates a departure from that model. *Figure taken from [12]*

The deformation of the FS was explained by an $s - d$ transition, which is clearly evident from the results of [12] in Figure 4 showing the DOS, where the d contribution starts to dominate at 10 GPa.

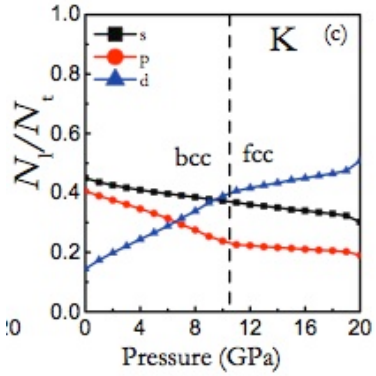

Figure 4: Angular momentum-decomposed DOS / total DOS at Fermi level for bcc K as a function of pressure. *Figure taken from [12]*

Furthermore, Figure 5 shows their calculated phonon frequencies where there is a softening along the $[0\xi\xi]$ direction and at 15 GPa the frequencies become imaginary suggesting a structural instability. As the slope of the phonon dispersion (as q goes to 0) is correlated with the elastic constants, Xie et al. [12] calculated the latter for bcc K at ambient pressure. Their results are shown in Figure 6 where C' beomes negative at 15 GPa, which is thus associated with

the phonon softening.

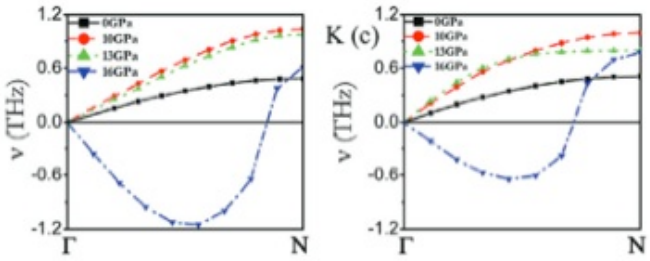

Figure 5: Transverse acoustic phonon frequencies of bcc K as a function of pressure along the $[0\xi\xi]$ direction. The left panel shows the results from the DFPT method and the right panel shows the results from supercell method. *Figure taken from [12]*

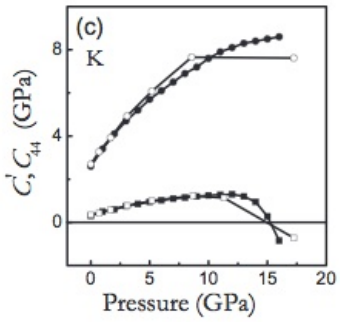

Figure 6: Elastic constants of C' and C_{44} for bcc K as a function of pressure. The open squares (C') and circles (C_{44}) are from previous studies for comparison and the solid ones are the results of [12]. *Figure taken from [12]*

They conclude that as a result of this C' instability associated with the softening of the phonon modes, there is a transition from bcc to fcc as described by Bain's path [24], that is there is a martensitic phase transition due to a continuous displacement of atoms in the unit cell. In other words there is a continuous change of the ratio c/a [13] so that $c/a = \sqrt{2}$ for fcc and $c/a = 1$ for bcc. Figure 7 shows the total energy as a function of the ratio c/a: at 0

GPa there are two minima (at $c/a = \sqrt{2}$ and $c/a = 1$) and it was found that fcc was more energetically favourable at zero pressure and temperature but at ambient temperature bcc was found to be the most stable; upon pressure increase the minimum at $c/a = 1$ vanishes as fcc is again more favourable [12].

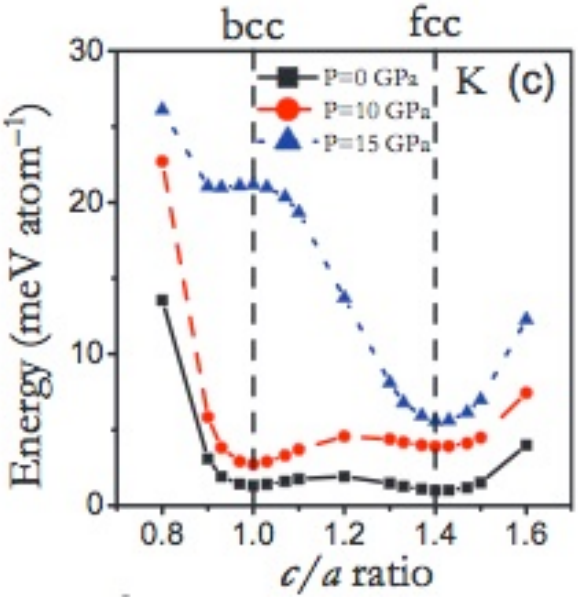

Figure 7: Total energy as a function of the ratio c/a at 0, 10 and 15 GPa. *Figure taken from [12]*

It is worth noting that although experimentally the bcc structure has been found to be the most stable these results were obtained at room temperature and *ab initio* studies have shown that at zero temperature different phases are more stable. For instance, Kang et al. [14] calculated the energies (at zero pressure and temperature) of the bcc, fcc and hcp structures of K by the means of DFT with both the local-density approximation (LDA) [25] and GGA. Their results show that for both methods the most stable structure is the

hcp one. Moreover, Alouani et al. [20] calculated the enthalpy of the bcc and fcc phases of K using the linear muffin-tin orbitals [26] including the scalar-relativistic effects. Their results are shown in Figure 8 where it can be seen that the transition bcc-fcc occurs at 10.74 GPa and that at zero temperature the bcc phase is the most stable one. They found the equilibrium lattice constant to be 5.14 Å for the bcc lattice at $T = 0$ K and the bulk modulus at the same temperature was found to be $B_0 = 3.97$ GPa.

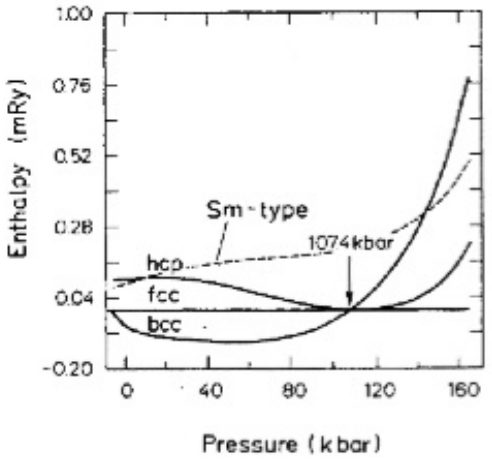

Figure 8: Enthalpy as a function of pressure for the bcc, fcc, hcp and Sm-type structures for K. *Figure taken from [20]*

1.2 fcc phase

Experiments have shown that the fcc structure of K has a lattice parameter of $a = 5.13$ Å at 11.7 GPa [8]. As for the bcc phase many *ab initio* studies have investigated the properties of the fcc structure of K and some of their findings are summarised in Table 2.

Table 2: Structural properties for fcc K at $T = 0$ K determined by *ab initio* calculations

a (Å)	B_0 (GPa)	Method [Reference]
7.16	3.23	Full-potential linear augmented plane-wave [27]
6.52	4.52	Pseudopotential plane-wave [27]
6.34	5.2	Full potential linearized augmented plane-wave [13]
6.36	4.5	LDA [14]
6.65	3.5	GGA PBE [14]
6.40	4.4	Pseudopotential method [15]
6.35	4.6	Augmented plane-wave with LDA [16]
6.58	**4.25**	**Experimental x-ray diffraction [10]**

Xie et al. [27] investigated the fcc structure of K by studying the evolution of the FS and lattice dynamics with pressure. They carried out the lattice dynamics calculation within the framework of DFT with the exchange-correlation described by the LDA. The FS calculations were performed within the DFT framework using the full-potential linearized augmented plane wave method, the exchange-correlation functional was described using the GGA and 32 768 k points were utilised. Figure 9 shows the evolution of the 2D FS of K with pressure.

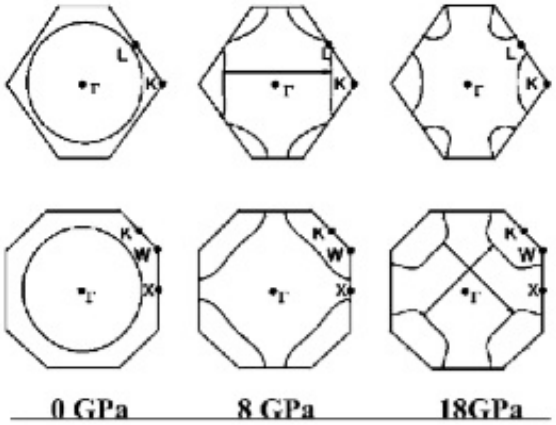

Figure 9: 2D FS of K for different pressures and on reciprocal lattice planes (001) (lower panel) and (110) (upper panel).*Figure taken from [27]*

These results confirm what was found in Xie et al. [12] (see Figure 3) until 11 GPa where the bcc-fcc transition occurs. However at 18 GPa, Figure 9 shows the disappearance of a Fermi surface nesting (FSN) in (110) and the appearance of a second parallel feature of Fermi surface nesting (FSN) in (100) along the ΓK direction with a nesting vector of 0.58, which coincides with the structural transition at 19 GPa (see Section 3). The FSN is accompanied by an increase of the d state contribution as well as a phonon softening along the ΓK direction and hence these electronic and phonon instabilities were deemed to be the possible source of a structural instability [12].

Further *ab initio* studies were carried out by Sanna et al. [28] in order to investigate the possible superconductivity of fcc K. Their study was based on the DFT for the superconducting state (SCDFT) [29]. They found fcc K to be a superconductor with a critical temperature of 2 K under which it loses all its electrical resistance. They attributed this superconductivity with the typical association of electronic changes with unstable phonon frequencies in alkali

metals, which in turn leads to strong electron-phonon couplings yielding superconductivity. Shi and Papaconstantopoulos [30] argued that the latter was not a sufficient explanation as the strong electron-phonon couplings were mainly due to the slow increase of the bulk modulus of K with pressure, causing the Hopfield parameter (which measures the electron-phonon coupling [31] - to be larger and hence the electron-phonon coupling constant as defined by McMillan [32] to be larger as well.

1.3 Host-guest structure

The third phase of K (K-III) is an incommensurate host-guest structure which is defined as "two interpenetrating components, a 'host' and a 'guest', which are incommensurate with each other along one or more axes [6]" It was first observed in 1990 in barium and has since then been observed in many other elements although it has never been observed at ambient pressure for any of them. Furthermore, because the host and guest are incommensurate, the host unit cell has a non-integer number of atoms and so in K there are 16 host atoms and 2x($\frac{c_H}{c_G}$) guest atoms [33], as shown in Figure 12.

McMahon et al. [6] carried out a study of K-III up to 25 GPa via x-ray powder diffraction and single dispersive methods. The transition of K-II to K-III was determined at 19 GPa and $T = 300$ K. They found that their diffraction pattern at 22.1 GPa showed strong peaks, which were indexed on a body-centred unit cell with $a = 9.767$ Å and $c = 4.732$ Å. However weaker peaks, which could not be accounted for by the latter, were also present and were explained by a host-guest composite structure with a 16 atom host structure and a C-face-centred tetragonal guest structure with $a = 9.767$ Å, $c_H = 4.732$ Å and $c_G = 2.952$ Å;

yielding a ratio $\gamma = \frac{c_H}{c_G} = 1.603$. Figure 10 shows the lattice parameters and coordinates of the atoms at different pressures determined experimentally by [6].

P (GPa)	a_{host}	c_{host}	c_{guest}	x_{host}	y_{host}
19.5	9.937(1)	4.879(1)	3.036(1)	0.7856(6)	0.0881(9)
20.6	9.865(2)	4.810(1)	2.993(2)	0.7941(7)	0.089(1)
21.3	9.819(1)	4.775(1)	2.978(2)	0.7924(6)	0.0914(6)
22.1	9.767(1)	4.732(1)	2.952(2)	0.7897(3)	0.0847(3)
23.1	9.715(1)	4.687(1)	2.935(2)	0.7990(4)	0.0861(6)
22.2[a]	9.770(2)	4.724(1)	2.954(2)	0.7960(4)	0.0845(5)
21.6[a]	9.809(2)	4.762(1)	2.972(3)	0.7947(4)	0.0901(5)
20.5[a]	9.878(1)	4.819(1)	2.996(2)	0.7917(4)	0.0879(4)
19.7[a]	9.9303(2)	4.868(2)	2.880(3)	0.7854(4)	0.0889(4)
18.8[a]	9.979(1)	4.920(2)	3.042(2)	0.7857(4)	0.0871(4)

Figure 10: Table of the lattice parameters and atom coordinates for K-III. *Figure taken from [6]*

The transition from fcc to K-III is accompanied by a drop in volume of 10 % and a decrease in coordination number from 12 to 9 [33]. Electrical resistance and optical resistivity of K were measured [34] and significant changes in these properties were experimentally observed at this phase transition. Indeed the resistance was found to increase by a factor of 50 in a pressure range up to 60 GPa and this was associated with core ionization [33]. On the contrary a decrease in the optical reflectivity was observed suggesting the presence of an optical gap over wide regions of the BZ [33]. Degtyareva [33] explained the changes in the optical properties by the change in the interaction of the BZ and the Fermi sphere as well as the filling of the BZ. Indeed, Degtyareva [33] determined that the filling of the BZ increased from 0.5 (for K-fcc) to 0.95 (for K-III) and that the total number of BZ planes in contact with the Fermi sphere

increased from 14 (for K-fcc) to 48 (for K-III). As noted by Degtyareva [33] the incommensurate nature of the crystal yields additional planes compared to a commensurate structure contributing in a gain in electron band structure energy to the detriment of the electrostatic term that favours more symmetrical configurations. It was also found that the shortest distance between two host atoms at 22.1 GPa is 2.832 Å(10), which is smaller than double the ionic radii thus implying an increase in the number of valence electrons [33]. Using the BRIZ program [35], which allows a visualisation of the BZ and Fermi sphere interaction, Degtyareva [33] determined the number of valence electrons to be 2.6 and attributed this non-integer number of electrons per atom to the overlap of s and d levels. Furthermore she noted that different number of valence electrons should be expected for host and guest atoms with a bigger participation from the d electrons for the guest atoms [33].

Given the incommensurate nature of the crystal the host-guest distances vary from one unit cell to another. McMahon et al. [6] determined the closest approach to be 2.948 Å, which takes place when the chain of guest atoms are in the centre of squares formed by the host structure and the largest host-guest distance is 3.176 Å, which occurs when the guest atoms are in the centre of square anti-prisms of the host framework. However, McMahon et al. [6] plotted γ as a function of pressure (see Figure 11) and noticed that it passed through the commensurate value of $\frac{8}{5}$ with no discontinuities and hence, allowing calculations to be carried out.

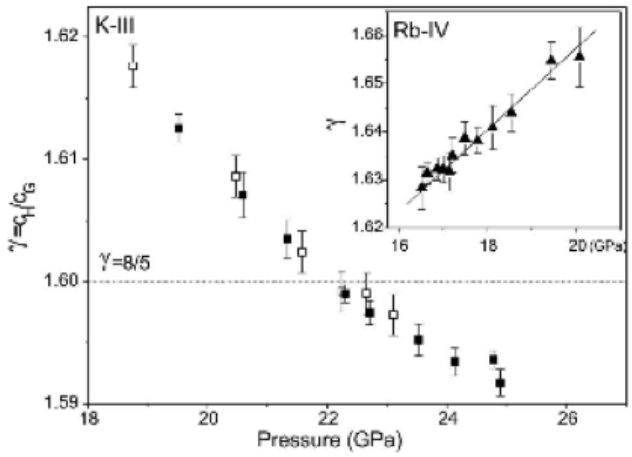

Figure 11: Ratio γ as a function of pressure for K-III with the same graph for Rb-IV in the inset. *Figure taken from [6]*

The most recent study of K-III was carried out by Lundegaard et al. [36], who performed x-ray powder and single crystal diffraction with a 99.9% pure sample of K and the diffraction data was collected from six different samples. The transition from K-II to K-III was observed at 18.8 GPa, consistent with the previous reported results. This study focused on the phase transitions of the guest structure of K-III from 18.8 GPa to 54 GPa (pressure of the transition K-III to K-IV). It was determined that from 18.8 GPa to 30 GPa, a first 'subphase' of K-III, K-IIIa, consisted of an I-centred host lattice (I4/mcm) with $a_H = 9.536$ Å and $c_H = 4.543$ Å and a C-centred guest lattice (C4/mcm) with $a_H = a_G$ and $c_G = 2.865$ Å. At 32.7 GPa, a second 'subphase', K-IIIb, was observed as the host reflections were unchanged but an obvious shift in the guest's reflections positions relative to the host was observed. The host structure remained an I-centred lattice with $a_H = 9.322$ Å and $c_H = 4.417$ Å and the guest reflections were indexed on an A-centred orthorhombic lattice (Ammm)

with $a_G = 6.570$ Å $b_G = 13.174$ Å and $c_G = 2.789$ Å. Upon further pressure increase to 40.2 GPa, Lundegaard et al. [36] observed a second reversible change in the positions of the guest reflections without changes to the host reflections. The guest structure was found to be a C-centred tetragonal lattice, thus making it isostructural with K-IIIa. These transitions of the guest structure at 30 GPa and 39.7 GPa, which were found to be reversible upon pressure decrease, results in K being the first element to undergo a re-entrant phase transition back to a lower pressure form as shown in the phase diagram in Figure 13. Also unique to K, are the C-centred guest structure of K-IIIa and the A-centred structure of K-IIIb, which have never been observed in any other alkali metal [36] (see Figure 12).

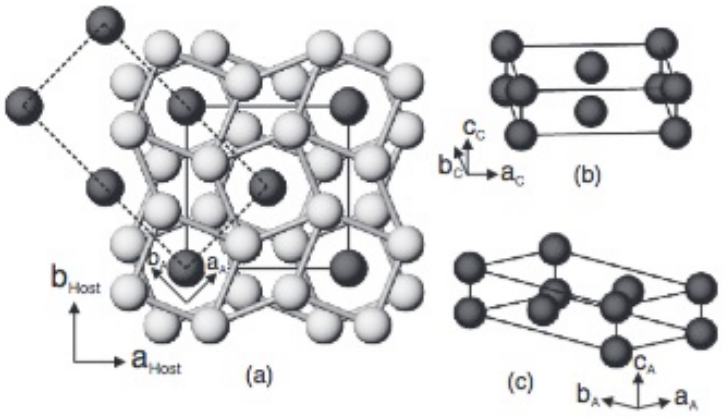

Figure 12: (a) Structure of K-IIIa in projection down the c-axis where the host atoms are in light gray and the guest atoms in dark gray. (b) shows the C-centred tetragonal guest structure of K-IIIa and (c) shows the A-centred orthorombic guest structure of K-IIIb. *Figure taken from [36]*

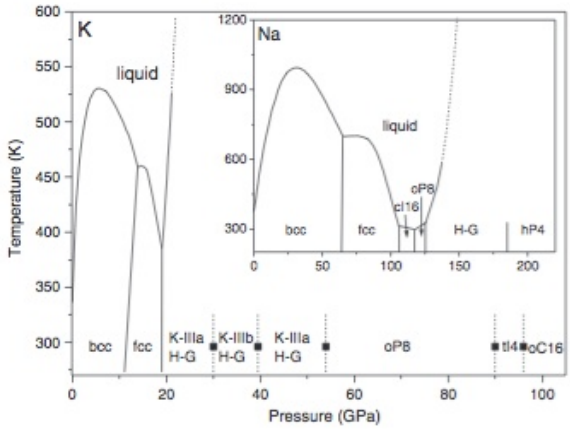

Figure 13: Phase diagram of K up to 100 GPa where the black squares denote the transition pressures at room temperature. The inset shows the phase diagram of Na. *Figure taken from [36]*

1.4 hP4 structure

Marques et al. [37] carried out x-ray powder diffraction experiments with a high-purity sample of K in a diamond anvil cell. They found the previously mentioned host-guest structure present in six samples but in two samples they observed a different phase between 25 and 35 GPa. From the diffraction pattern of this phase they concluded that it was hexagonal, spacegroup was $P6_3/mmc$, with 4 atoms per unit cell located on the $2a$ and $2c$ sites at (0,0,0) (K_1) and ($\frac{1}{3}$, $\frac{2}{3}$, $\frac{1}{4}$) (K_2), respectively. The lattice parameters at 25 GPa are $a = 4.2180(5)$ Å and $c = 5.7369(3)$ Å with a c/a ratio of $1.3601(2)$ [37].

Marques et al. [37] then carried out *ab initio* calculations in order to determine the enthalpy of K using DFT with a plane-wave pseudopotential approximation, the PBE exchange-correlation functional and the PAW description of the electron-ion-core interaction. Brillouin zone integrals were converged with plane-wave cutoff (390 eV) and k-point density (18^3 meshes) using tetrahedron

method with Blöchl correction and neglecting zero point vibrational contributions. Their results are shown in Figure 14.

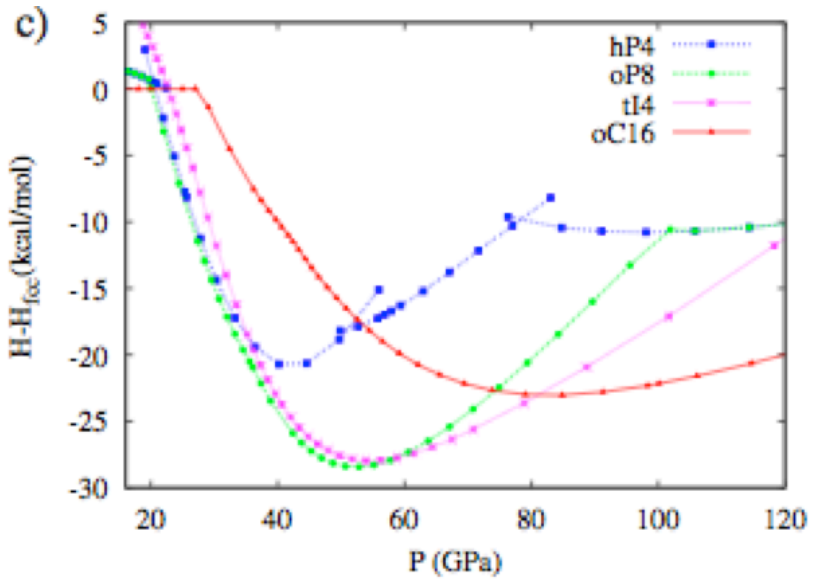

Figure 14: Calculated enthalpies for different structures of K as a function of pressure. *Figure taken from [37]*

Inspection of the calculated c/a ratio in the pressure range 20-50 GPa, where hP4 was observed, showed that it was very close to the experimental value of 1.36. Marques et al. [37] also noted that this same ratio was very similar to the c/a ratios of some di-alkali-metal monochalcogenides and their corresponding sulfates, which led them to note that the atoms in the hP4 structure are arranged as the cations of these structures. However, they also pointed out that the interstitial $2d$ site (1/3, 2/3, 3/4) of the Ni2-In-type structures are occupied by anions whereas they are unoccupied in the hP4 structure. They therefore applied the metallic matrices model (AMM) to the hP4 structure, as the AMM states that the crystal structure of inorganic compounds can be de-

scribed by a metallic matrix that acts as a host lattice for the non-metallic atoms and the electron density of the metal therefore determines the location of the non-metallic atoms. When applying the AMM to the hP4 structure, the latter was treated as an electride (an ionic compound in which an electron is an anion) and hence the valence electrons were located in interstitial positions: this increased interstitial localization is responsible for the stabilization of this phase [37].

1.5 oP8 structure

The phase oP8 was observed at 54 GPa until 90 GPa at 300 K with a coordination number of 8 and the shortest interatomic distances are $2.46 - 2.51$ Å which is smaller than double the ionic radii ($2r_i = 3.05$ Å) [33]. The number of valence electrons was found to be 2, the total number of BZ planes is 34 and the filling of the BZ by occupied electron states is 93.2 % [33]. Figure 15 shows the crystal structure of oP8 at 58 GPa along with the interatomic distances.

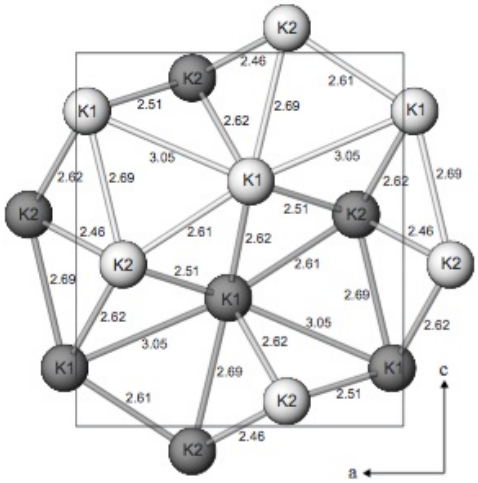

Figure 15: Structure of the oP8 phase of K viewed down the b axis. Interatomic distances are given in Å beside each bond which are shown between nearest and next-nearest neighbours. *Figure taken from [38]*

Lundegaard et al. [38] investigated the possibility of oP8 being a stable phase of K. Electronic structure calculations were achieved within the DFT framework with a plane-wave pseudopotential. They made use of the GGA for the exchange-correlation functional and the PAW all-electron description of the electron-ion-core interaction. To avoid core overlap the 3s, 3p and 4s states were treated as valence electrons. The method of Monkhorst and Pack was used to approximate the BZ integral and the energy converged with a 13 x 15 x 9 k mesh and a plane wave cutoff of 290 eV. Structural relaxations were carried out using a conjugate-gradient minimization of the total energy and for the final calculation, the tetrahedron method with Blöchl correction was used. The enthalpy was determined at zero temperature and by neglecting the zero point contributions. Figure 16 shows the results for the enthalpy of structures oP8, tI4 and oC16 for pressures ranging from 25 to 100 GPa. Assuming K-III to

have the lowest enthalpy where it was experimentally observed (that is up to to 54 GPa) they found that the oP8 phase was more stable than tI4 for pressures up to 58 GPa. Furthermore Lundegaard et al. [38] found that the electronic band structure of oP8-K at 58 GPa shows it to be a semi-metal with an indirect E-Y band overlap of 1.2 eV and a low density of states and a pseudogap near the Fermi level.

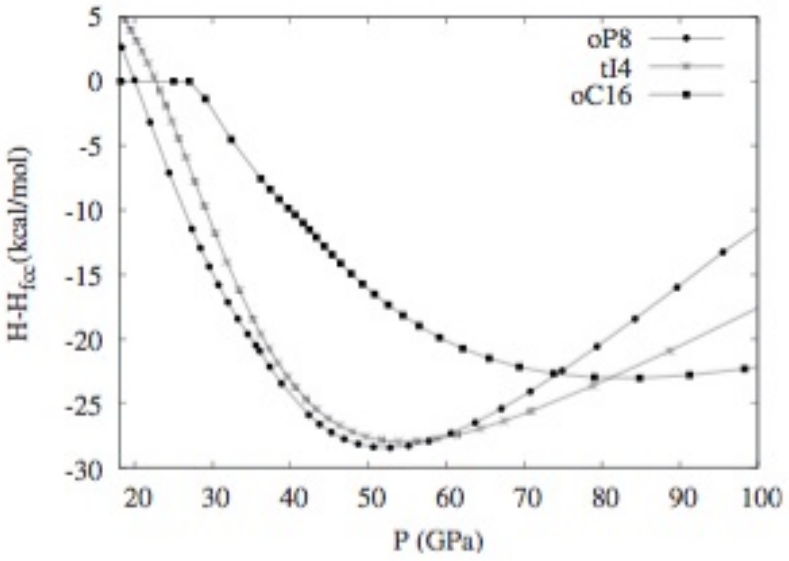

Figure 16: Enthalpies (relative to that of fcc K) as a function of pressure for the phases oP8, tI4 and oC16. *Figure taken from [38]*

They also carried out experiments in diamond-anvil cells to determine the existence of the oP8 phase in K. They found the oP8 phase to appear at 56 GPa up to 90 GPa where the appearance of new diffraction peaks suggested a new phase transition. The lattice parameters, volume and atomic coordinates are shown in Figure 17.

	P (GPa)	a (Å)	b (Å)	c (Å)	V_{atom} (Å^3)	x_1	z_1	x_2	z_2
*oP*8-K (calc)	58	5.705	3.266	6.377	14.85	0.033	0.156	0.143	0.568
*oP*8-K (obs)	58(1)	5.602(1)	3.311(1)	6.380(1)	14.792(6)	0.034(1)	0.156(1)	0.144(1)	0.567(1)
*oP*8-Na (obs)	119(2)	4.7650(5)	3.020(3)	5.251(2)	9.45(1)	0.015(1)	0.180(1)	0.164(1)	0.586(1)

Figure 17: Lattice parameters, volume and fractional coordinates of the oP8 structure of K. *Table taken from [38]*

Calculations of the optical properties of K were carried out within the framework of DFT along with PAW pseudopotentials and the LDA by Adebayo [39]. Results from the latter were found to be in fairly good agreement with the previous calculations and experimental data of optical conductivity [34]. Adebayo [39] found that the optical properties of the oP8 phase of K showed that the latter is an insulator in certain frequency ranges.

1.6 tI4 structure

The body-centered tetragonal structure tI4 has only been seen in alkali metals [33] found for Cs above 4.3 GPa and above 20 GPa for Rb. The uniqueness for K is the transition from the oP8 phase to tI4, not seen in the other alkalis. The latter has the following lattice parameters for K: $a = 2.322$ Å and $c = 8.669$ Å with atoms positioned at $4a$(0,0,0) [38]. This phase was found experimentally from 90 to 96 GPa with a volume change from the oP8 phase of about 1% [38]. This transition is accompanied by a decrease in coordination number from 8,10 to 4; an increase of the number of valence electrons to 2.5 and a decrease of the filling of the BZ with electron states to 79.2 % [33]. One of the explanations for the stability of the tI4 phase has been proposed as due to the $s - d$ transfer and the formation of electride-like compounds with high electron

density in the anion positions [33].

Ma et al. [40] looked for the lowest free energy structure using ab initio evolutionary simulations for a given pressure and temperature. Evolutionary algorithms were set in place to mimic evolution as described by Darwin using natural selection, heredity and mutations. Oganov and Glass [41] developped the method used in Ma et al. [40] which searches the entire free energy landscape to find the global minima and only requires the chemical composition as an input to predict the most stable structure as well as a set of metastables ones. Oganov and Glass [41] have implemented their algorithm in the USPEX code (Universal Structure Predictor: Evolutionary Xtallography). Ma et al. [40] used VASP (DFT within the GGA) for structure relaxations and the all-electron projector-augmented wave method was used. They treated the $3s$, $3p$ and $4s$ electrons as valence and used a plane-wave kinetic energy cutoff of 390 eV. All the calculations were performed at $T = 0K$ and at 40, 100, 150 and 300 GPa with systems of 4, 6, 8, 12 and 16 atoms in the simulation cell. They identified the following phases after the K-III structure: tI4, which transitions to oC16 at 80 GPa. They also observed the same sequence for both Rb and Cs but not for the lighter alkali metals Li and Na. They explain this similarity between larger alkali metals to their d electrons dominance due to the s-d charge transfer under pressure.

It is worth noting that the phase oP8 was not predicted by this algorithm, as opposed to the results of Lundegaard et al. [38] but given the relatively similar methods the reason as to why their results are so different have not yet been determined. However the two *ab initio* studies agree on the transition pressure of tI4 to oC16 as Ma et al. [40] determined it to be 80 GPa and Lundegaard et al. [38] found tI4 to be stable from 58 to 81 GPa but experimentally

it has been predicted stable between 90 and 96 GPa as mentioned previously; which raises the question of the possible sources of errors in both their *ab initio* studies and experiments. It was suggested by Lundegaard et al. [38] that firstly the calculations were performed at 0 K whereas the experiments were carried out at room temperature but although this may be a contributing factor the discrepancies are too large to solely be attributed to temperature differences. So Lundegaard et al. [38] added that the differences may arise from the ill description of the energy differences by the GGA functional when the type of bonding is extremely different between the two phases, which seems to be the case as the oP8 phase has a much lower metallicity indicating a much stronger electron correlation [42].

1.7 oC16 and dhcp

The seventh phase of K refered to as oC16 is a C-face centred orthorombic structure (space group Cmca). Diamond-anvil cells experiments [38] determined the transition pressure from the tI4 structure to be 96 GPa, the lattice parameters $a = 8.03$ Å $b = 4.753$ Å $c = 4.716$ Å and an atomic volume of 11.25 Å^3 . However *ab inito* calculations [38] showed the transition to occur at 81 GPa as seen in Figure 16 (for the possible explanations of this discrepancy refer to the discussion in Section 7). Ma et al. [40] also calculated the enthalpies of oC16, as shown in Figure 18, which indicates that at 250 GPa the oC16 structure becomes unstable with respect to the double hexagonal close packed (dhcp) structure.

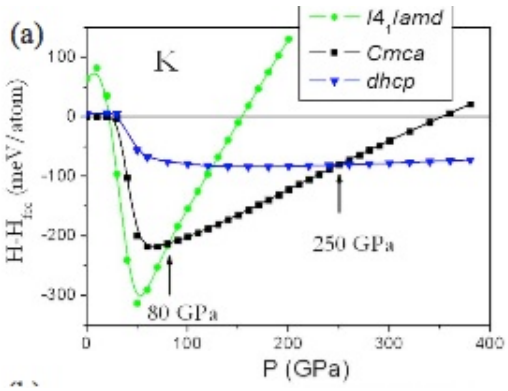

Figure 18: Enthalpy differences with respect to the fcc structure for K. *Figure taken from [40]*

1.8 Liquid Potassium

Zha and Boehler [43] studied the melting curve of K using a diamond anvil cell method up to 14.5 GPa. Their results are shown in Figure 19 where it can be seen that at low temperatures they are in good agreement with previous *in situ* experiments using the hydrostatic fluid cell method [44] and using modified single-stage piston-cylinder apparatus [45]. Figure 19 shows a practically constant melting temperature above 7 GPa and a change in slope at 11 GPa going from close to 0 degrees per kilobar to about 3 degrees per kilobar. Given that this change of slope coincides with the phase transition pressure Zha and Boehler [43] estimated the bcc-fcc-liquid triple point at 11 GPa and 568 K.

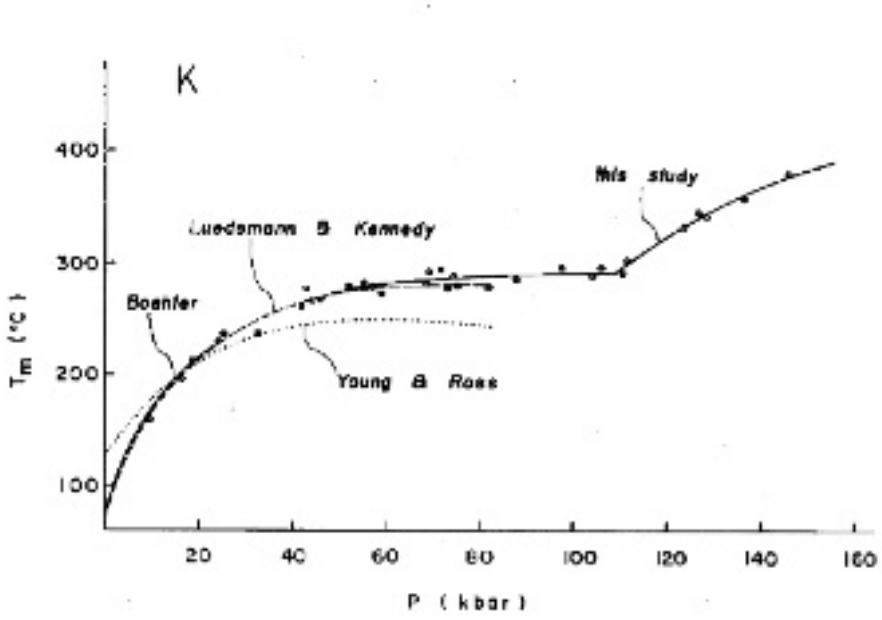

Figure 19: Temperature against pressure for K compared to previous results. *Figure taken from [43]*

A theoretical study [46] used an experimentally fitted two-parameters local pseudopotential (indicated in Figure 19 by Young and Ross) and predicted a melting maximum at around 6 GPa. Although it was not observed experimentally in [43], it was observed more recently in [9]. Indeed McBride et al. [9] conducted experiments using *in situ* x-ray diffraction and diamond anvil cell to determine the melting curve of K up to 22 GPa. Figure 20 shows their results where there is an obvious maximum in the bcc phase. Given the good agreement with the two previous experimental results ([45], [43]) they combined the latter with their own measurements and their bcc-fcc-liquid triple point at 13.6 GPa and 466 K to get a fit using the Kechin equation [47]. This approach yielded a maximum in the bcc phase at 530 K and 5.8 GPa. They also did not rule out the possible presence of a second maximum as it was previously

found in Cs [48], but it was not observed in this study. Moreover they noted the presence of a sharp minimum at 19 GPa and 390 K which coincides with the phase transition from the fcc structure to the K-III phase, during which the melting temperature rises very quickly at a rate of 65 K/GPa. They attributed the change of sign of the gradient to both structural and electronic transitions in the liquid phase. It was also observed by McBride et al. [49] that upon heating the guest chains melted before the sample as can be seen in Figure 21

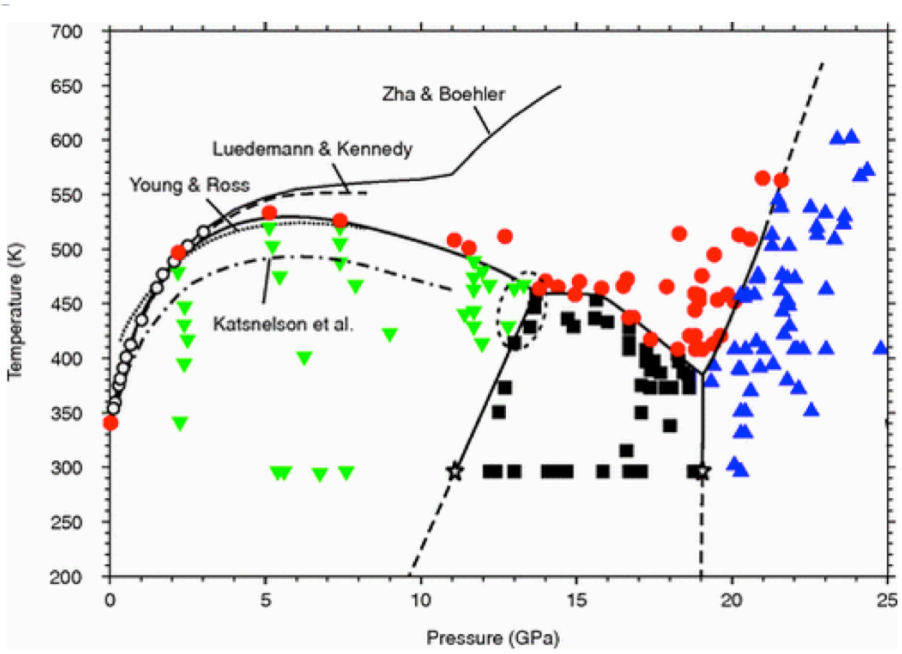

Figure 20: Temperature against pressure for K determined by McBride et al. [9]. Green triangles represent bcc, the black squares represent fcc, the blue triangles represent KIIIa and the red circles represent the liquid.The results are compared to previous studies. *Figure taken from [9]*

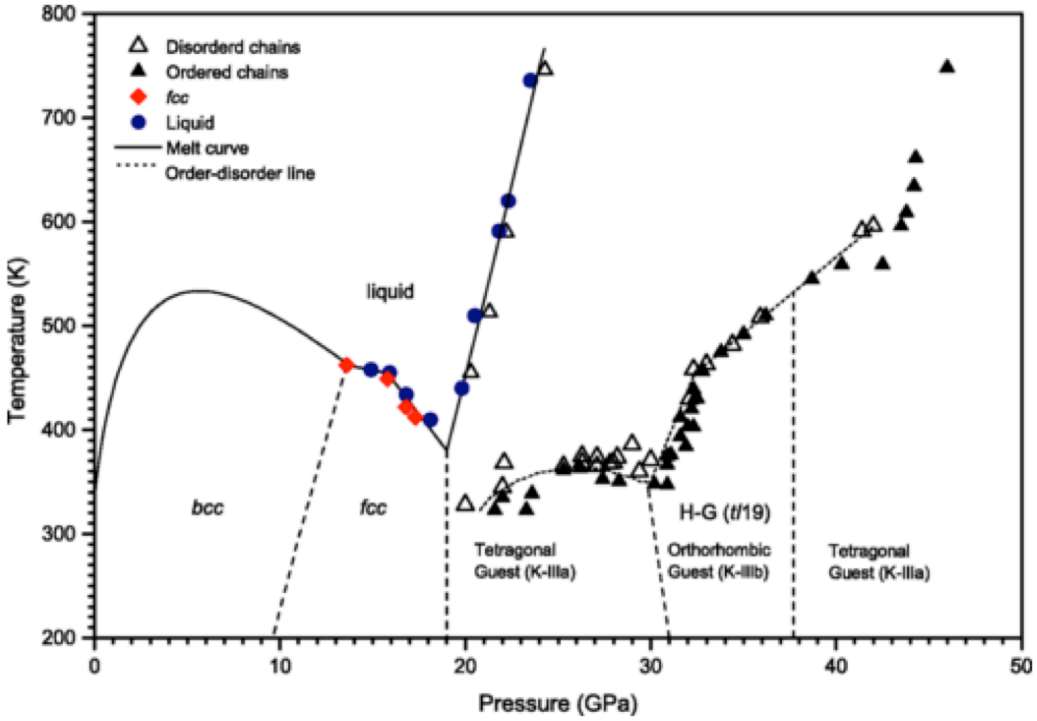

Figure 21: Phase diagram of potassium determined by McBride et al. [49]. The solid line represents the melting curve, the blue circles represent the liquid, the red diamonds represent the fcc phase, the black triangles represent the disordered guest chains of KIIIa and KIIIb, the white triangles represent the ordered guest chains. *Figure taken from [49]*

Katsnelson et al. [17] produced a phase diagram of K (see Figure 22) using different melting criteria and compared it to the experimental results of [43]. They used the empirical Lindeman criterion, which was found relatively inaccurate on wide pressure ranges; they also used the Varshni melting criterion [50] (which gives the relation between band gap energy and temperature), which appeared much more accurate and finally they used the equally accurate Debye model from which they extracted the thermodynamic quantities and the temperature was determined using the *ab initio* elastic moduli. Figure 22

shows that the results fit the experiment of Zha and Boehler [43] but are not in agreement with the expected melting maximum from both experiment [9] and theory [46].

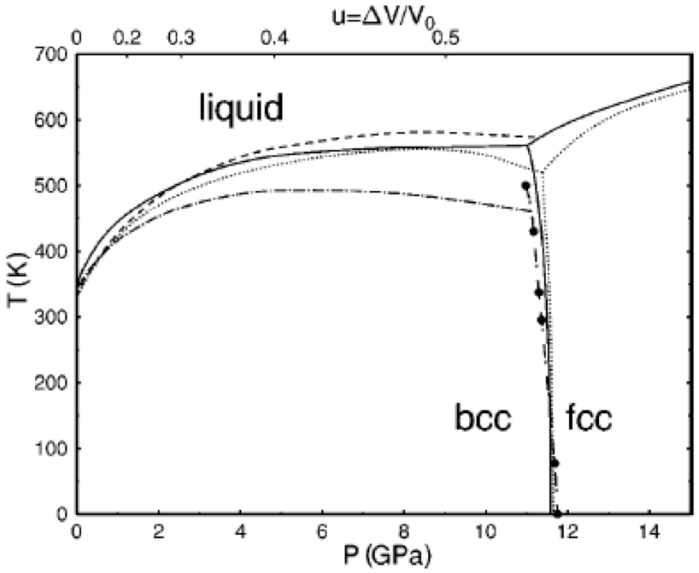

Figure 22: Phase diagram of K using the Lindeman criterion (dash-dotted line), the Varshni criterion (dashed line), the Debye model (dotted line) and the experimental results from [43]. *Figure taken from [17]*

Belashchenko and Smirnova [51] described liquid K using the molecular dynamics model of the embedded atom (EAM) [52] with data on static K compression for T=300 K and pressures ranging from 0 GPa to 52.9 GPa as well as data from shock compressions for pressures ranging for 0 GPa to 86 GPa. The potential energy in the EAM is the sum of the embedding potential of the *i*th atom and the pair potential previously described in [51]. Various states of liquid K were considered with pressure of about 0 GPa and density at temperatures up to 2200 K. Their model contained 2000 atoms, the interaction cutoff radius was 9.57 Å and the Verlet algorithm was used. Their results are

shown in Figure 23 for the temperature, density, pressure, potential energy, bulk modulus and diffusion constant. They did point out that the results yielded an overstating of the bcc phase for K given that the pressure found is of 0.12 GPa when it should be zero. Their results also showed that the inner energy was not in very good agreement with the experiments and attributed this to a calculated heat capacity lower than the experimental values, which are reported to be very close to the classical value of 3R until it falls off from 27.5 J/ (mol K) at 400 K to 22 J/(mol K) at 1800 K and the understating of the bulk modulus was determined to be the cause of the understating of the calculated heat capacity.

No.	T, K	d, g/cm^3	p, GPa	
			EAM	experiment
1*	300	0.8560	0.120	~0
2*	200	0.8560	0.088	~0
3	343	0.8278	0.005	~0
4	473	0.7986	0.002	~0
5	723	0.7401	0.002	~0
6	1000	0.6735	0.012	~0
7	1500	0.5455	−0.025	~0
8	2000	0.3834	0.016	~0
9	2200	0.2712	0.034	0.019

$-U$, kJ/mol		K_T, GPa		$D \times 10^5$, cm^2/s	
EAM	experiment	EAM	experiment [7]	EAM	experiment [8]
82.04	82.80	3.37 ± 0.08	–	–	–
84.66	–	–	–	–	–
79.12	79.09	2.95 ± 0.03	2.74	4.45	4.02
75.33	75.01	1.69 ± 0.04	2.29	8.11	11.3
68.32	67.44	0.69 ± 0.01	1.72	17.0	–
60.71	59.11	0.84 ± 0.09	1.18	29.3	–
45.08	42.13	0.35 ± 0.11	0.58	58.9	–
26.53	19.39	<0.1	0.20	116.2	–
16.32	7.69	<0.1	–	152.4	–

Figure 23: Properties of liquid K calculated by MD (with EAM potentials). Reference to experiments [7] refers to [53] and [8] refers to [54]. *Figure taken from [51]*

Furthermore they used the Grüneisen model with the data on shock compression up to 86 GPa to determine the temperatures on the Rankine-Hugoniot curve. They found that the Grüneisen model, which assumes the heat capacity and the Gruneisen parameter to be temperature independent, to be in good agreement with the experiments for pressures ranging from 10-15 GPa. Belashchenko and Smirnova [51] also estimated the melting temperature of K at high pressures using the reheating method [55] and their results are shown in Figure 24, which they found to be in good agreement with experiments up to 5 GPa but then the calculated curve lies about 100 K above the experimental curve due to the fact that the potential used cannot describe properly both the liquid and solid states.

p, GPa	0.0	2.35	4.60	8.60	17.5	30.0	41.2
T_m,K	319	466	581	681	794	994	1231

Figure 24: Pressure and melting temperatures of K using the reheating method. *Data taken from [51]*

1.9 Conclusion

This review clearly shows that there are many areas that require further investigation. First of all, it has yet to be determined which phase is stable at zero temperature and pressure. As it was pointed out in sections 2 and 3, different studies yielded different results and it would be useful to determine the accuracy of the method used by investigating wether the stable phase is bcc or fcc. Second of all there were more *ab initio* studies on high pressure solid phases than experimental results, perhaps due to the difficulty of carry-

ing out experiments at very high pressures. Similar difficulties occur at high temperatures resulting in a sparsity of studies made and the phase diagram of potassium has not yet been determined accurately. Third of all the enthalpy of the host-guest structure has not been determined but as it has been recently found that γ passes through a commensurate value of $\frac{8}{5}$, enthalpy calculations can be carried out. Fourth, the discrepancy between the experimental and calculated transition pressures also need to be addressed. Finally, no first-principles study of the anharmonicity or the melting have been carried out. For clarification, the sequence of the structures of K mentioned in this chapter is shown in Figure 25

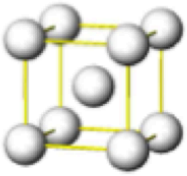

bcc structure stable until 11 GPa

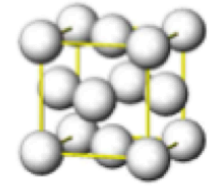

fcc structure stable until 19 GPa

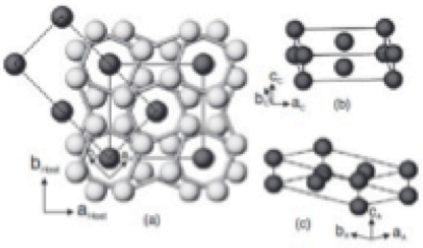

KIII structure stable until 42 GPa

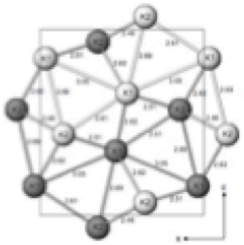

oP8 structure stable until 57 GPa

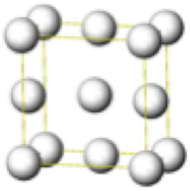

tI4 structure stable until 81 GPa

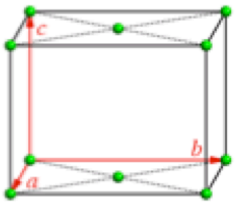

oC16 structure stable from 81 GPa

Figure 25: Summary of the sequence of the strutures of K along with the theoretical transition pressures.

This thesis will first give an overview of the computational methods used, then the results of the static calculations will be given in Part 3 followed by the solid phase diagram study using the quasi-harmonic approximation in Part 4 and the anharmonicity study in Part 5. Finally Part 6 will show the study of the melting

2 Computational Method

2.1 Electronic structure problem

2.1.1 Schrödinger's equation

Quantum mechanics is based on the description of the electrons and the nuclei in a system in terms of a wavefunction $\Psi(\mathbf{r},\mathbf{R})$, where **r** and **R** represent the electronic and ionic coordinates, respectively. The latter does not represent an observable physical quantity but its square represents the probability of finding an electron at any point r. The time-independent Schrödinger's equation describes the energy and dynamics of a system as follows [56]:

$$\widehat{H}\Psi(r) = E\Psi(r) \tag{1}$$

where E is the energy and $\widehat{H}$ is the Hamiltonian operator:

$$\widehat{H} = -\frac{1}{2}\sum_{i=1}^{M}\nabla_i^2 - \frac{1}{2}\sum_{A=1}^{M}\frac{\nabla_A^2}{M_A} - \sum_{i=1}^{N}\sum_{A=1}^{M}\frac{Z_A}{r_{iA}} + \frac{1}{2}\sum_{i=1}^{N}\sum_{i\neq j}^{N}\frac{1}{r_{ij}} + \frac{1}{2}\sum_{A=1}^{M}\sum_{A\neq B}^{M}\frac{Z_A Z_B}{R_{AB}} \tag{2}$$

where the subscript i and j refer to the electrons, N is the number of electrons in the system, the subscripts A and B refer to the nuclei, M is the number of nuclei in the system, M_A (M_B) is the mass of nucleus A (B), Z_A (Z_B) is the nuclear charge, r_i and r_j are the spatial coordinates of the electrons, R_A and R_B are the spatial coordinates of the nuclei and r_{ab} is the distance between the electrons a and b and R_{AB} is the distance between two nuclei A and B. The first and second terms of Equation 2 represent the kinetic energy of the electrons and the nuclei, respectively. The third terms denotes the attractive

interaction between the electrons and the nuclei. The fourth and fifth term give the repulsive interaction between any two electrons and any two nuclei, respectively. Theoretically, all the properties of a system can be derived from the many-body Schrödinger's equation. In practice, only a few cases have full analytical solutions. The difficulty in solving this equation is due to various factors, mainly the electrons and the nuclei obey different statistics and there are (3M+3N) coupled degrees of freedom. It is therefore necessary to introduce approximations to render the problem approachable.

2.1.2 Born-Oppenheimer approximation

Although the Schrödinger's equation can be solved exactly for one-electron systems such as the hydrogen atom, approximations are required in order to find solutions to the Schrödinger's equation for many electron systems. Given that the mass of the nuclei is much larger than that of the electrons, the Born-Oppenheimer approximation assumes that the atomic nuclei are stationary with respect to the electrons, which therefore move adiabatically in a potential of fixed nuclei [56]. This approximation yields the separation of the wavefunction as follows:

$$\Psi(\mathbf{x}, \mathbf{R}) = \phi(\mathbf{r}, \mathbf{R})\chi(\mathbf{R}) \tag{3}$$

Where $\phi(\mathbf{r}, \mathbf{R})$ is the electronic wavefunction and $\chi(\mathbf{R})$ is the nuclear wavefunction. One thus obtains an electronic eigenvalue equation with an electronic Hamiltonian:

$$[T_e + V_{ee} + V_{eN}(\mathbf{r}, \mathbf{R})]\phi(\mathbf{r}, \mathbf{R}) = \epsilon_n(\mathbf{R})\phi(\mathbf{r}, \mathbf{R}) \tag{4}$$

The latter yields eigenvalues $\epsilon_n(\mathbf{R})$ of the nth state which depend parametrically on **R**. Each solution, $\epsilon_n(\mathbf{R})$ gives rise to a Born-Oppenheimer surface on which a nuclear eigenvalue equation can be solved:

$$[T_N + V_{NN}(\mathbf{R}) + \epsilon_n(\mathbf{R})]\chi(\mathbf{R}) = E\chi(\mathbf{R}) \tag{5}$$

The Born-Oppenheimer approximation does not allow for non-adiabatic effects such as excitations of the electrons, however there will be no excitation if the difference in energy between the ground state and the first excited state is larger than kT, thus this approximation is valid if the surfaces have energy spacings larger than kT [57]. Furthermore, in many cases it is not necessary to solve the quantum nuclear equation and the classic nuclei approximation is thus valid.

2.1.3 Exchange and correlation

When describing electron interactions one must take into account two important properties. Firstly, in a many electron system, electrons repel each other due to their charges, which is expressed in the fourth term of Equation 2 but this repulsion also gives rise to a correlation between the motion of one electron and the motion of the other electrons in the system, for which there is no analytical expression [58]. Secondly because electrons are indistinguishable they obey the Pauli principle so the probability of finding two electrons must stay the same upon position exchange - that is:

$$\mid \Psi(r_1, r_2) \mid^2 = \mid \Psi(r_2, r_1) \mid^2 \tag{6}$$

This can be achieved by having two wavefunctions that are identical (symmetric) or have opposite sign (antisymmetric). Bosons, and more generally particles with integer spin must satisfy the first condition but fermions (or particles with half spin) must have antisymmetric wavefunctions. Electrons being fermions their wavefunctions satisfy:

$$\Psi(r_1, r_2) = -\Psi(r_2, r_1) \tag{7}$$

The reduction in energy due to this exchange symmetry is called the exchange energy, E_X.

2.1.4 Hartree-Fock

Hartree proposed a method in 1928 [59] to solve the Schrödinger's equation for multiple-electron systems which relies on the independent electron approximation. Therefore the Hamiltonian is represented by the sum of the Hamiltonians of each electron and the wavefunction is the product of the different electronic wavefunctions. This representation yields a one electron Schrödinger equation for the *i*-th electron:

$$-\frac{\nabla^2}{2}\psi_i(\mathbf{r}) + V(\mathbf{r})\psi_i(\mathbf{r}) = \epsilon_i\psi_i(\mathbf{r}) \tag{8}$$

Where $V(\mathbf{r})$ represents the potential, which includes the electron-nuclear interactions ($V_{eN}(\mathbf{r}) = -Ze^2\sum_{\mathbf{R}}\frac{1}{|\mathbf{r}-\mathbf{R}|}$) and the mean field arising from the other electrons ($V_H(\mathbf{r}) = -e\int \mathrm{d}\mathbf{r'}\rho(\mathbf{r'})\frac{1}{|\mathbf{r}-\mathbf{r'}|}$), known as the Hartree potential. The potential therefore depends on the wavefunctions of the other electrons, that is, it depends on the solution to the equation. The Hartree method must there-

fore be solved using a self-consistent field (SCF) method. The procedure is as follows [58] :

- Provide an initial guess for the electronic orbitals ψ_i
- Compute the Hartree potential, $V_H(\mathbf{r})$
- Solve the one-electron Schrödinger equation
- If the new orbitals are the same (within a threshold) as those in step 1 then the procedure ends. If they are different, the new orbitals are then used as the new input in step 1. The procedure is repeated until convergence.

Evidently, the rawness of the Hartree approximation produces fairly inaccurate results as it neglects fundamental physical principles such as the Pauli exclusion principle, which requires the wavefunction to be antisymmetric with respect to the change of any two electrons. The latter is clearly not respected in the Hartree approximation. This can be remedied by introducing a Slater determinant of single electron orbitals, which was done by Fock in 1930 [60]. This leads to the Hartree-Fock method. As per the Pauli exclusion principle, the wavefunction must be antisymmetric; condition that is satisfied when the wavefunction is built as a Slater determinant. The Hartree-Fock equation is derived as:

$$\widehat{F}\phi_i = \epsilon_i \phi_i \tag{9}$$

Where $\widehat{F}$ is defined as:

$$\widehat{F} = \widehat{h} + \sum_{j}^{n} (2\widehat{J_j} - \widehat{K_j}) \tag{10}$$

where $\widehat{J}_j$ is the Coulomb operator and $\widehat{K}_j$ is the exchange operator:

$$J_j(\mathbf{r}_1)\phi_i(\mathbf{r}_1) = \int d^3\mathbf{r}_2 \phi_j^*(\mathbf{r}_2)\phi_j(\mathbf{r}_2)\frac{1}{r_{12}}\phi_i(\mathbf{r}_1) \tag{11}$$

$$K_j(\mathbf{r}_1)\phi_i(\mathbf{r}_1) = \int d^3\mathbf{r}_2 \phi_j^*(\mathbf{r}_2)\phi_i(\mathbf{r}_2)\frac{1}{r_{12}}\phi_j(\mathbf{r}_1) \tag{12}$$

The total electron energy is therefore:

$$E = 2\sum_{i}^{n}(\epsilon_i + h_i) \tag{13}$$

Similarly to the Hartree method, the Hartree-Fock equation is non linear and must therefore also be solved by the SCF method.

2.2 Density Functional Theory

2.2.1 Hohenberg-Kohn theorems

Density functional theory (DFT) [21] computes the ground state properties of a system using the electron density rather than the wavefunction. It relies on the two Hohenberg-Kohn theorems [61]:

Theorem 1: *Assuming a non-degenerate ground state, the total energy of the ground state is a functional of the electron ground state density*.

This first theorem introduces a one-to-one mapping between the ground state wavefunction and density. Furthermore, the Schrödinger's equation can now be solved by finding a function of 3 spatial variables instead of 3N variables.

Theorem 2: *The true electron density is the one which minimizes the en-*

ergy of the functional.

This theorem provides a variational treatment of the electron density to determine the ground state and only the functional $E[n]$ is sufficient to determine the ground state density. Using these theorems, the total energy can be split as:

$$E[n(r)] = T[n(r)] + E_{ee}[n(r)] + E_{Ne}[n(r)] \tag{14}$$

where $n(r)$ is the electron density, T is the kinetic energy, E_{ee} is due to the electron-electron interaction and E_{Ne} is due to the nuclear-electron interaction. Equation 14 can be re-written as:

$$E[n(r)] = F[n(r)] + \int n(r)V_{ext}(r)dr \tag{15}$$

where the first term is called the Hohenberg and Kohn universal functional because it applies to any system and comprises the kinetic and electron-electron energy terms; the last term gives the interaction of the electron density with an external potentia $V_{ext}(r)$ and this term is system dependent [62].

The two Hohenberg-Kohn theorems, though groundbreaking, have a few limitations. First, they are restricted to non-degenerate ground states. Second, they do not provide any guidance on the treatment of excited states and third, they are only defined for *v*-representable densities [61]. However, this limitation does not usually affect practical applications.

2.2.2 Kohn-Sham equations

The method of Kohn-Sham [63] presumes that the ground state density of the interacting system is the same as that of a fictitious non-interacting system. This leads to the splitting of the kinetic energy into two terms as follows:

$$T[n(r)] = T_s[n(r)] + T_c[n(r)] \tag{16}$$

where T_s is the kinetic energy of the non-interacting system (that is the first term in Equation 2) and a correction T_c due to the electron-electron interactions. Although there is no exact expression of T_s as a functional of $n(r)$, it is possible to express it as a functional of single particle orbitals, which are themselves functionals of $n(r)$. Secondly, Kohn and Sham [63] split the $E_{ee}[n(r)]$ term in two:

$$E_{ee}[n(r)] = \frac{e^2}{2} \int \int \frac{n(r)n(r')}{\mid r - r' \mid} dr dr' + E_{NC}[n(r)] \tag{17}$$

where the first term is the classical Hartree energy and the second term gives the non-classical part of the electron-electron interactions. Therefore Kohn and Sham [63] inferred that the universal functional has the following form:

$$F[n(r)] = T_s[n(r)] + V[n(r)] + E_{XC}[n(r)] \tag{18}$$

where the second term is the classical Coulomb interaction and the third term is the exchange correlation energy, which gives the non-classical part of the electron-electron interaction and is given by:

$$E_{XC}[n(r)] = (T[n(r)] - T_s[n(r)]) + (E_{ee}[n(r)] - V[n(r)]) = T_C[n(r)] + E_{NC}[n(r)] \tag{19}$$

This leads to a total energy as follows:

$$E[n(r)] = T_s[n(r)] + (U_H[n(r)] + V[n(r)]) + E_{XC}[n(r)] \tag{20}$$

Solutions of the Kohn-Sham system can be viewed as a minimization problem but as mentioned previously, T_s is not an explicit functional of the electron density and therefore Equation 20 cannot be minimized directly with respect to $n(r)$. One can thus apply a scheme devised by Kohn and Sham [63]. First, one writes the minimization as:

$$\frac{\partial E[n(r)]}{\partial n(r)} = \frac{\partial T_s[n(r)]}{\partial n(r)} + \frac{\partial (U_H[n(r)]}{\partial n(r)} + \frac{\partial V[n(r)])}{\partial n(r)} + \frac{\partial E_{XC}[n(r)]}{\partial n(r)} = 0 \tag{21}$$

Where $\frac{\partial V[n(r)])}{\partial n(r)} = v(\mathbf{r})$ is the 'external' potential the electrons move in, $\frac{\partial (U_H[n(r)]}{\partial n(r)} = v_H(\mathbf{r})$ is the Hartree potential and $\frac{\partial E_{XC}[n(r)]}{\partial n(r)}$ is written as $v_{XC}(\mathbf{r})$. Second, one considers now a system of noninteracting particles moving in a potential $v_s(\mathbf{r})$, which therefore no longer have Hartree and exchange-correlation terms. The minimization is now:

$$\frac{\partial E_s[n(r)]}{\partial n(r)} = \frac{\partial T_s[n(r)]}{\partial n(r)} + \frac{\partial V_s[n(r)])}{\partial n(r)} = 0 = \frac{\partial T_s[n(r)]}{\partial n(r)} + v_s(\mathbf{r}) \tag{22}$$

Solving Equation 22 yields the density $n_s(\mathbf{r})$ and if one chooses the potential as $v_s(\mathbf{r}) = v(\mathbf{r}) + v_H(\mathbf{r}) + v_{XC}(\mathbf{r})$ then both minimizations must have the same solution: $n_s(\mathbf{r}) \equiv n(\mathbf{r})$ Finally this yields a set of single particle equations:

$$(-\frac{1}{2}\nabla^2 + v_s(\mathbf{r}))\chi_i = \varepsilon_i \chi_i \tag{23}$$

where $V_{\text{eff}}(r) = \int \frac{n(r)}{r_{12}} dr_2 + V_{XC}(r) - \sum_A^M \frac{Z_A}{r_{1A}}$; χ_i are the orthonormal molec-

ular orbitals. To solve the Kohn-Sham equations, one must first define the Hartree potential for which the electron density is required. Determining the electron density necessitates the single electron wavefunctions, which in turn are known when solving the Kohn-Sham equations. It is therefore a non-linear problem which must also be solved by the SCF method:

- Define initial trial density $n(r)$
- Solve Kohn-Sham equations to find the single electron wavefunction
- Calculate the electron density $n_1(r)$ using the single particle wavefunctions
- If $n_1(r) = n(r)$ then the cycle ends and $n_1(r)$ is the ground state density. If $n_1(r) \neq n(r)$ then the trial density is updated and the cycle starts again.

2.2.3 Mermin formulation finite temperature

Mermin [64] proved a generalization of the DFT at finite temperatures. To do so, a statistical average is produced to find the energy of the equilibrium state. Mermin [64] constructed a grand potential functional, which must be minimized to obtain the equilibrium density [65]:

$$\Omega[\widehat{\rho}] = \mathsf{Tr}\widehat{\rho}[(\widehat{H} - \mu\widehat{N}) + k_B T ln\widehat{\rho}] \tag{24}$$

whose minimum is the equilibrium grand potential:

$$\Omega[\widehat{\rho}_0] = -k_B T ln\mathsf{Tr}e^{-k_B T(\widehat{H}-\mu\widehat{N})} \tag{25}$$

with the density matrix:

$$\rho_0 = \frac{e^{-\beta(\widehat{H}-\mu\widehat{N})}}{\mathsf{Tr}e^{-\beta(\widehat{H}-\mu\widehat{N})}} \tag{26}$$

This generalization allows for the entropy and other thermodynamic properties to be defined as density functionals. In order to apply Mermin's formulation, the occupation numbers n_i must be expressed in accordance with the Fermi-Dirac distribution:

$$n_i = [e^{\beta(\epsilon-\mu)} + 1]^{-1} \tag{27}$$

2.3 Implementation of DFT

2.3.1 Plane Wave Basis Set

In the Kohn-Sham equations the wavefunctions are represented as a linear combination of basis functions. The repetition of the unit cell of a periodic crystal leads to the application of periodic boundary conditions, therefore the simulation cell will interact with images of itself in all directions. Hence the potential felt by an electron will be periodic and according to Bloch's theorem [66], the wavefunction of an electron within a periodic potential can be expressed as:

$$\psi_{j,\mathbf{k}}(\mathbf{r}) = u_j(\mathbf{r})e^{i\mathbf{k}\cdot\mathbf{r}} \tag{28}$$

Where j refers to the band index, **k** is a wavector confined to the first Brillouin Zone (BZ), $u_j(\mathbf{r})$ is a periodic function with the periodicity of the lattice. Therefore plane waves are a natural choice of basis functions to expand $u_j(\mathbf{r})$ with

wavectors **G**, which are the reciprocal lattice vectors of the crystal:

$$u_j(\mathbf{r}) = \sum_{\mathbf{G}} c_{j,\mathbf{G}} e^{i\mathbf{G}\cdot\mathbf{r}} \tag{29}$$

where $\mathbf{G} \cdot \mathbf{R} = 2\pi m$, with m an integer, **R** the lattice vectors and $c_{j,\mathbf{G}}$ the plane wave coefficients. Hence the electron wavefunctions can be expressed as:

$$\psi_{\mathbf{k}}(\mathbf{r}) = \sum_{\mathbf{G}} c_{\mathbf{k},\mathbf{G}} e^{i(\mathbf{k}+\mathbf{G})\cdot\mathbf{r}} \tag{30}$$

The number of plane waves required to expand a wavefunction is determined by the parameter E_{cut}, which is the maximum kinetic energy a plane wave can have:

$$\frac{(\mathbf{k}+\mathbf{G})^2}{2} \leq E_{cut} \tag{31}$$

Using planewaves as a basis set offers advantages as the planewaves are orthogonal and independent of atomic positions thus yielding no basis set superposition error (BSSE occurs as the interatomic distance decreases - the basis sets of two atoms can overlap, which impacts the energy of the atoms.) Planewaves do, however, present a few drawbacks; mainly the very quick variations of the inner wavefunctions, which require a very large number of planewaves.

2.3.2 Pseudopotentials

A solid can be regarded as a collection of valence electrons and ion cores. The ion cores are comprised of nuclei and tightly bound core electrons. The wavefunctions of the valence electrons are orthogonal to the core electrons

wavefunction. All-electron DFT methods treat both valence and core electrons equally. The closer electrons are to the nucleus, the higher their kinetic energies and therefore an extremely large number of planewaves would be required to model the rapid oscillations close to the nucleus. Including these high energy plane waves is computationally expensive, hence the solution to that problem is to take into consideration the fact that only valence electrons participate in chemical bonding, whereas the core electrons are too tightly bound to contribute significantly to bonding. The pseudopotential approach therefore assumes the ion cores to be frozen [67]. Core electrons are thus represented by a pseudopotential. Pseudo wavefunctions will not have nodes inside the core regions so they only require a small basis set.The norm conserving potential [68] introduces a core radius where the all-electron wavefunction is replaced by a soft, nodless pseudo wavefunction. The latter must have the same norm as the all-electron wavefunction within the core radius and outside both wavefunctions must be identical. The scattering properties of the full ionic potential should be the same as that of the pseudopotentials. The total charge of each pseudo wavefunction must equal the charge of the all electron wavefunction (norm conserving criteria). The norm conserving pseudopotential can be fairly hard (i.e it requires a lot of Fourier components). A larger core radius results in a softer pseudopotential, (therefore more efficient in terms of number of plane waves) and a smaller radius provides more transferability and reliability [69]. Vanderbilt [70] introduced the ultrasoft pseudopotential, which is no longer required to obey the norm conservation thus reducing the cutoff energy. Indeed, a high cutoff energy is necessary when tightly bound orbitals have a significant weight inside the core region and to reduce the basis set the norm conserving criteria must be violated by removing the charge of these

orbitals from the core achieved by introducing a generalized orthonormality condition.They also guarantee the appropriate scattering properties making them more transferable and accurate.

2.3.3 Projector Augmented Wave method

Pseudopotentials, albeit simple, do present drawbacks. Indeed, assuming the core to be frozen results in losing information on the charge density and the wave function near the nucleus.Augmented Waves Methods [71] introduced basis functions based on atom like wavefunctions thus rendering it possible to study bonding.The Projector Augmented Wave (PAW) method was first introduced by Blöchl [72] and is a combination of pseudopotential and augmented wave methods. The PAW method seeks a linear transformation which maps the true all-electron wavefunction $\psi(r)$ and exhibits strong oscillations near the nucleus, to an auxiliary smooth wavefunction.

$$\psi(r) = \widehat{T}\widetilde{\psi} \tag{32}$$

The transformation operator is determined using the fact that the real wavefunctions are already smooth far from the core and therefore should only modify the wavefunctions near the core. To determine the transformation operator $\widehat{T}$, non overlapping spheres centered on atoms are defined. In each sphere R, a pseudo partial wave ϕ_i is constructed as the solution of the Schrödinger equation for the isolated atom. The transformation operator is then defined as:

$$\widehat{T} = 1 + \sum_i (\mid \phi_i > - \mid \widetilde{\phi}_i >) < \widetilde{p}_i \mid \tag{33}$$

Where ϕ_i is the all electron partial wave and $\widetilde{p}_i$ is the projector function. $\widehat{T}$ therefore gives access to the true wavefunction via the auxiliary wavefunction as follows, where the equation is illustrated in Figure **??**.

$$\mid \psi_n >= \mid \widetilde{\psi_n} > + \sum_i (\mid \phi_i > - \mid \widetilde{\phi}_i >) < \widetilde{p}_i \mid \widetilde{\psi_n} > \tag{34}$$

The PAW method relies on the frozen core approximation and presents many advantages as it outputs the real density of the system and provides high accuracy.

2.3.4 Exchange-Correlation Functionals

Local Density Approximation An approximation to the exchange-correlation energy was introduced by Kohn and Sham [63] called the local density approximation (LDA), which is based on the exchange-correlation energy of a uniform electron gas. A uniform electron gas is defined in Burke [73] as a system in which 'the electrons sit in an infinite region of space, with a uniform positive external potential, chosen to preserve overall charge neutrality'. The exchange energy for a homogeneous electron gas is known exactly:

$$E_x^{LDA}[n] = -\frac{3q^2}{4}\left(\frac{3}{\pi}\right)\int \mathrm{d}^3 r n(r)^{4/3} \tag{35}$$

The correlation energy of a uniform electron gas, however, is not known. Ceperley and Alder [74] carried out quantum Monte-Carlo calculations to obtain the total energy of a uniform electron gas. Correlation energies are now parametrizations of this data, the most common one is that of Perdew and

Zunger [25] e_c^{LDA}. Hence the total LDA exchange correlation energy is:

$$E_{XC}^{LDA}[n] = \int \mathsf{d}^3\mathsf{r}\, e_{XC}^{hom}[n(r)] \tag{36}$$

Equation 36 illustrates the 'local' character of this approximation given that the exchange correlation energy at r depends only on the electron density at r. The LDA presents some further disadvantages beyond its local character such as the underestimation of the band gap for semiconductors and insulators, overestimation of the binding energies and incomplete cancellation of the self-interaction [75] (i.e. the artificial interaction of an electron with itself), to cite a few. Nevertheless, the LDA has been successful, partially due to its cancellation of errors as the correlation energy is underestimated and the exchange energy is overestimated. A variation of the LDA, called the local spin density approximation (LSDA) [76], was developed using the energy of a polarised uniform electron gas.

Generalised Gradient Approximation Although the LDA proved to be successful for many systems, any real system is inhomogeneous as its density varies spatially. The generalised gradient approximation (GGA) includes terms with the gradient of the density:

$$E_{XC}^{GGA}[n] = \int \mathsf{d}^3\mathsf{r} f(n(r), \bigtriangledown n(r)) \tag{37}$$

Various GGAs have been developed and they differ in the choice of f. For instance, Becke's exchange functional (B88) [77] is a parametrised one (it's also been called semi-empirical given that parameters are fitted to experimen-

tal data). The latter is a functional of the density and the density gradient. In 1991, Perdew and Wang derived the PW91 exchange correlation functional Perdew et al. [19], which is a correction to the LSDA . In 1996, Perdew, Burke and Ernzerhof derived the PBE exchange-correlation functional [78], which has replaced PW91.

It is worth noting that GGA is definitely an improvement to the LDA but even though the density gradient is included it is still thought of as local given that both the density and its gradient are evaluated at a single point. GGA should therefore be considered semi-local rather than non-local as the gradient and the density are still taken at a single point r. Both the GGA and LDA fail to describe adequately Van der Waals interactions [79].

Van der Waals functionals As aforementioned, both the LDA and the GGA do not accurately describe dispersion interactions, mainly due to their local character. New functionals were developed by [80, 81] specially to include non local effects and thus attempt to describe Van der Waals effects. The two functionals that will be described here have the same form:

$$E_{XC} = E_X^{GGA} + E_C^{LDA} + E_C^{NL} \tag{38}$$

Where E_X^{GGA} is the GGA exchange energy, E_C^{LDA} is the local correlation energy from the LDA and E_C^{NL} is the non-local correlation energy. J. Klimes [80] studied the implementation of various alternatives of the E_X^{GGA} term, mainly the exchange energy of GGA-PBE and of B88. Both have shown good performances on the calculations of bulk modulus, atomization energies and lattice constants.

2.3.5 K-point sampling

Observables, (such as the energy, charge density, density of states...) are integrals over all k-points within the first Brillouin Zone. In an infinite system, the states are grouped in bands and inside each band the states are continuous. As the simulation cell is finite, the states are discrete. In a periodic system, a primitive cell can be used but there woud still be an infinite number of states, however, an infinite number of k-points would need to be included. Therefore to evaluate computationally it is necessary to replace the integral with a discrete sampling of k space. The number of plane waves,in principle infinite, is limited by the energy cutoff. It is worth noting that the states are discrete as the simulation used is small so one can trade k-points for cell size. The most widely used approach is that of Monkhorst and Pack [82]. The latter only requires the total number of k points in each direction as input N_i and the formula spreads out the points as follows:

$$k_{n_1,n_2,n_3} = \sum_{i=1}^{3} \frac{2n_i - N_i - 1}{2N_i}\mathbf{G} \tag{39}$$

Where N_i is the number of k-points in each direction, $n_i = 1, ..., N_i$ and **G** are the reciprocal lattice vectors of the crystal.This yields a rectangular grid of points spaced evenly throughout the BZ. Increasing the dimensions of the grid makes the sampling finer and more accurate. The appropriate grid size can be determined by carrying out convergence tests.

Partial occupancies and metallic systems For metallic systems the functions being integrated are discontinuous at the Fermi level as the occupancies

jump from 1 to 0, which means a denser k-point grid is required to get well converged results. Indeed many k-points are needed to reproduce the fact that for the highest band there is a sharp discontinuity in k space between occupied and unoccupied states. To integrate this discontinuous function, one solution is to smear it out by replacing the step function by a smoother function. The latter can be achieved by introducing an electronic temperature. Regardless of the method chosen, the results should be comparable as in all cases the occupation numbers will become fractional and the energy functional is no longer the 0K one but the total free energy E-TS.

Fermi Smearing The first method consists in using the physical Fermi-Dirac function in lieu of the step function thus leading to the grand canonical extension of DFT by Mermin:

$$f(\frac{\epsilon-\mu}{\sigma}) = \frac{1}{e^{\frac{\epsilon-\mu}{\sigma}}+1} \tag{40}$$

Where σ is the smearing factor, which represents the electronic temperature of the system. The issue with this method is that to increase the convergence speed, the value of σ must be fairly large (0.1-0.5 eV), corresponding to thousands of degrees.

Linear tetrahedron method In this case the one electron energies are interpolated between k-points and the integral is calculated analytically within each tetrahedron [83]. Later Blöchl et al. [84] introduced a correction formula to the linear approximation by taking into account the curvature of the bands at the Fermi surface. This method is known to converge very fast and is widely

used to determine the energy of bulk materials, though it is less adequate for supercells as a minimum number of k-points is required. Moreover it is not applicable to calculate exact forces.

Gaussian Smearing Here, the step function is replaced by a Gaussian one:

$$f(\frac{\epsilon-\mu}{\sigma}) = \frac{1}{2}(1 - \text{erf}[\frac{\epsilon-\mu}{\sigma}]) \tag{41}$$

Where erf is the error function. The method of Methfessel and Paxton [85] is a generalization of the Gaussian smearing by expanding the step function as a set of orthogonal Hermite polynomials.

2.3.6 VASP: inputs

VASP [86] was used to perform the calculations in this thesis. VASP is a software package to carry out first principles electronic structure and quantum molecular dynamics calculations by computing an approximation of the Schrödinger equation with DFT. VASP requires four input files: POTCAR, POSCAR, KPOINTS and INCAR.

POTCAR This file contains the potentials of each atomic species as well as information about each element such as their mass, valence etc. The POTCAR file also contains a default energy cutoff, ENMAX. Both hard and soft potentials are provided for some elements.

POSCAR It specifies the geometry of the unit cell as well as the position of the atoms within that unit cell. After each run, VASP outputs a file CONTCAR,

which has the same format as POSCAR as it contains the ionic positions of the last step of relaxation and is therefore often used as a POSCAR input file if the relaxation has not converged.

KPOINTS This file gives the k-point sampling of the BZ.

INCAR It determines how and what to do by specifying a large number of parameters. A list and description of these parameters can be found in the VASP manual [87].

2.4 Quasi-Harmonic Approximation

At low temperatures, atomic vibrations are much smaller than interatomic distances thus the harmonic approximation assumes the ground state energy depends quadratically on these deviations from equilibrium [88]. Therefore, in the harmonic approximation, the vibrational contribution to the free energy does not depend on volume. The harmonic approximation, however, suffers from shortcomings such as infinite thermal conductivity and phonon lifetimes and the independence of vibrational spectra on temperature to cite a few. To remedy to these drawbacks one would have to calculate all phonon-phonon interactions [89]. The quasi-harmonic approximation (QHA) [88] avoids doing the latter to correct these failings by introducing volume dependent frequencies.

The potential energy of a crystal can be expressed as a function of atomic positions. If one takes a Taylor expansion around its equilibrium value then

the following is obtained [90]:

$$U_{\text{harm}}(V,R) = U_{\text{eq}} + \sum_i \frac{\partial U(V,0)}{\partial u_{i,\alpha}} u_{i,\alpha} + \frac{1}{2} \sum_{i,j,\alpha,\beta} \frac{\partial^2 U(V,0)}{\partial u_{i,\alpha} \partial u_{j,\beta}} u_{i,\alpha} u_{j,\beta} + O[u^3] \quad (42)$$

Where $u_{i,\alpha}$ is the displacement of the ith atom in the α direction The second term on the right hand side is null since it is evaluated at the equilibrium position, where the potential energy will be minimum. The QHA is obtained by only retaining the terms up to second order. The potential energy function U_{harm} then determines the Helmholtz free energy:

$$F(V,T) = E_{\text{perf}} + F_{\text{harm}}(V,T) \quad (43)$$

Where E_{perf} is the energy of the static lattice and $F_{\text{harm}}(V,T)$ is the quasi-harmonic contribution to the free energy, which can be expressed as:

$$F_{\text{harm}} = \frac{k_B T}{\Omega} \int_{BZ} d\mathbf{q} \sum_s \ln(2\sinh \hbar\omega_{\mathbf{q}s}/2k_B T) \quad (44)$$

Where Ω is the volume of the Brillouin Zone (BZ), $\omega_{\mathbf{q}s}$ is the frequency of the s-th vibrational mode at wave vector $\mathbf{q}$. The difficulty of QHA thus lies within the determination of the phonon density of states, which is a continuous function of the specific volume [88]. To obtain the phonon frequencies, there are two *ab initio* approaches to phonon calculations: the linear response method and the direct method. The former introduces a lattice perturbation yielding the inverse dielectric matrix , which is then used to get the dynamical matrix [91]. The direct approach has two variants: first, the frozen-phonon method [92] and second, the method relies on the forces induced on all atoms following

the displacement of atoms in a supercell with periodic boundary conditions. Only the latter will be described here. The phonon frequencies are the square root of the eigenvalues of the dynamical matrix:

$$D_{i,\alpha,j,\beta}(\mathbf{k}) = \sum_t \frac{\Phi_{i,\alpha,jt,\beta}}{\sqrt{M_i M_j}} \text{exp}^{i\mathbf{k}\cdot\mathbf{x_t}} \tag{45}$$

Where M_j and M_i are the masses of the atoms j and i in the primitive cell, jt is the equivalent atom of j in cell t and x_t is the displacement of cell t with respect to the primitive unit cell and $\Phi_{i,\alpha,jt,\beta}$ is the force-constant matrix. The dynamical matrix is the Fourier transform of the force constant matrix at wavevector **k**. The small displacement method aims to compute $\Phi_{i,\alpha,jt,\beta}$ by displacing one atom i in cartesian direction α, whilst keeping all other atoms fixed at equilibrium. The force field is then calculated via the Hellman-Feynamn theorem [93] and the restoring forces on all other atoms yield elements of the force constant matrix:

$$\Phi_{i,\alpha,j,\beta} = \frac{\partial^2 U}{\partial u_{i,\alpha} \partial u_{j,\beta}} \simeq -\frac{F_{j,\beta}}{u_{i,\alpha}} \tag{46}$$

The smaller the displacement, the better the harmonic approximation, however, if the displacements are too small then the numerical error becomes non-negligible. Translational invariance means that there are at most $3N$ calculations needed, where N is the number of atoms in the primitive cell. Symmetry relations, however, can reduce this number drastically. Also, in principle, the elements of the force constant matrix are not null for large separations so care must be taken when setting a cutoff distance beyond which these elements are negligible. Furthermore, the force constant matrix represents that in the infinite lattice but it is calculated in a supercell thus generating information only

at wavevectors that are reciprocal vectors of the supercell. Hence, a further assumption must be introduced [94]; assuming that the Wigner-Seitz (WS) cell is centred on the cell of the displaced atom (R) then it is assumed that the infinite force constant matrix is zero if R lies within a different WS, it is equal to the supercell force constant matrix if R lies within the same WS and is equal to the supercell force constant matrix divided by an integer P if R lies on the boundary of the same WS, where P is the number of WS cells with R on its boundary. Under this assumption the force constant matrix will converged to the infinite one as the dimensions of the supercell are increased [90]. Also, given that the crystal is not truly harmonic the expression for the force constant is only an approximation and in such is not necessarily invariant under symmetry relations of the crystal. It must, therefore, be symmetrised with respect with the point group operations of the crystal, which can also remove lowest-order anharmonicities [90]. There are other sources of errors when calculating the forces: errors due to the finite basis sets and k-point grid are inherent to all *ab initio* calculations, however, the Hellmann-Feynman theorem shows that errors in the wavefunctions will only yield second order errors in the energy but first order errors will be induced in the forces [90]. Errors can also arise from the relaxation of structures or anharmonicity.

2.5 Molecular Dynamics

Ab Initio Molecular Dynamics (AIMD) relies on a key principle that is ergodicity, which assumes that in the limit of infinite trajectory, thermal ensemble

averages are equivalent to time averages [95]:

$$< A >_{\text{time}} = < A >_{\text{ensemble}} \tag{47}$$

Two further assumptions must also be made; firstly, the nuclei are treated as classical particles and thus their positions and momenta follow Newton's equations of motion [66]:

$$\dot{x} = \frac{\partial H}{\partial p_x} = \frac{p_x}{m} = v_x \tag{48}$$

$$\dot{p_x} = -\frac{\partial H}{\partial x} = -\frac{\partial V(x)}{\partial x} = F = ma_x \tag{49}$$

Secondly, the forces on the nuclei are due to the electrons in their ground state (the latter refers to the Born-Oppenheimer approximation aforementioned). The AIMD scheme, therefore, computes the forces using the Hellmann-Feynman theorem at each time step and then integrates Newton's equations of motion using the Verlet algorithm [96] to generate the trajectory of the ions. The Verlet algorithm combines a backward and forward Taylor expansion of the positions $r(t)$:

$$r(t + \Delta t) = r(t) + v(t)\Delta t + \frac{1}{2}a(t)\Delta t^2 + \frac{1}{6}\dddot{r}(t)\Delta t^3 + \mathcal{O}(\Delta t^4) \tag{50}$$

$$r(t + \Delta t) = r(t) - v(t)\Delta t + \frac{1}{2}a(t)\Delta t^2 - \frac{1}{6}\dddot{r}(t)\Delta t^3 + \mathcal{O}(\Delta t^4) \tag{51}$$

Where $v(t)$ is the velocity, $a(t)$ is the acceleration and $\dddot{r}(t)$ is the third time derivative of $r(t)$ Adding these two Taylor expansions then gives:

$$r(t + \Delta t) = 2r(t) - r(t - \Delta t) + a(t)\Delta t^2 + \mathcal{O}(\Delta t^4) \tag{52}$$

This form of the Verlet algorithm provides a reasonable approximation for the trajectories, if the time step is small enough.

The electrons are relaxed at each time step in order for them to remain in the self-consistent ground state. The calculations in this work were performed in the canonical ensemble where the number of particles (N), the volume (V) and the temperature (T) are fixed and is thus referred to as the NVT-ensemble. The temperature was controlled by using an Andersen thermostat [97], which introduces random collisions of the particles with an imaginary heat bath at the set temperature. This is done by periodically, randomly reassigning the atomic velocities from a Maxwell-Boltzmann distribution at the same temperature and therefore this generates the canonical ensemble. When calculating thermal averages for a harmonic system (or similar to harmonic), the degrees of freedom do not exchange energy thus rendering the calculations very long in order to scan the whole phase space. The statistical sampling introduced by the Andersen thermostat resolves this problem.

2.6 Thermodynamic Integration

The Helmholtz free energy of a system is expressed as [98]:

$$F = -k_B T \ln \left\{ \frac{1}{N! \lambda^{3N}} \int \mathbf{dR_1}...\mathbf{dRn} \exp[-\frac{1}{k_B T} U(\mathbf{R_1}...\mathbf{Rn}; \mathbf{T}) \right\} \quad (53)$$

Where $\lambda = \frac{h}{(2\pi M k_B T)^{1/2}}$ is the thermal wavelength, N is the number of atoms in the system, M is the nuclear mass, $U(\mathbf{R_1}...\mathbf{Rn}; \mathbf{T})$ is the free energy of the electrons, h is the Planck constant, k_B is the Boltzmann constant and T is the temperature. This equation cannot be calculated directly as knowledge

of $U(\mathbf{R_1}...\mathbf{Rn};\mathbf{T})$ for every position of the atoms would be required. A method commonly used to calculate the Helmholtz free energy is thermodynamic integration [99]. Generally speaking, this scheme yields the difference of free energies $F_1 - F_0$. The anharmonic contributions to the free energies were calculated using thermodynamic integration. This method is founded on the idea that $F_1 - F_0$ is the work done when reversibly, continuously and isothermally switching the corresponding energy functions from U_0 to state U_1.To achieve the latter, a switching parameter λ is introduced thus defining a new potential energy function, $U_\lambda = h(\lambda)U_1 + f(\lambda)U_2$ where $h(\lambda)$ and $f(\lambda)$ are arbitrary switching functions that must fulfil the following conditions:

$$\begin{cases} h(0) = 1, h(1) = 0 \\ f(0) = 0, f(1) = 1 \end{cases} \tag{54}$$

A simple choice for the switching functions is $h(\lambda) = 1 - \lambda$ and $f(\lambda) = \lambda$. According to statistical mechanics, the work done in an infinitesimal change $d\lambda$ is [94]:

$$dF = < \frac{dU_\lambda}{d\lambda} >_\lambda d\lambda = < U_1 - U_0 >_\lambda d\lambda \tag{55}$$

Thus yielding the following formula:

$$\Delta F = F_1 - F_0 = \int_0^1 < U_1 - U_0 >_\lambda d\lambda \tag{56}$$

Where ΔF represents the work done and $< . >_\lambda$ is the thermal average in the ensemble generated by U_λ. U_1 is chosen as the *ab initio* energy function whose free energy we aim to calculate and U_0 is chosen as the total energy function of a "reference system", U_{ref}, whose free energy can be calculated. When phonons are stable, the reference system can be chosen to be the total

energy of the *ab initio* system calculated in the QHA. It is worth noting that the required computational effort is considerably reduced if the fluctuations of the energy differences between the reference and the *ab initio* systems are small given that it reduces the amount of sampling. Subsequently, M values of λ are chosen from the interval [0,1] and at each value an AIMD simulation is performed in the NVT-ensemble governed by the energy function U_λ to get the average $< U_1 - U_0 >_\lambda$. These averages were thus plugged into Eq. 56, which was then integrated numerically using the trapezium rule yielding ΔF. Errors associated with this method are mainly due to integration errors if the number of λ is too small and statistical errors.

In practice, two steps were introduced in order to render the procedure computationally efficient. Essentially, the method above was applied to the *ab initio* system with non-converged parameters, U_{low} (i.e. k-points grid, plane wave cutoff, number of valence electrons, smearing parameters). The second step calculated the difference between U_{low} and the now *ab initio* system with converged parameters, U. Given that the fluctuations of the energy differences between U_{low} and U were small enough, the following perturbative approach to TI was applied:

$$F \simeq E_{\text{low}} + < \Delta U >_0 + \frac{1}{2k_B T} < (\delta \Delta U)^2 >_0 \tag{57}$$

Where $\delta \Delta U = U_1 - U_0 - < U_1 - U_0 >_0$. This perturbative approach can be applied by sampling the phase space with the reference system and then extracting statistically independent configurations to perform an *ab initio* static calculation on each of them.

2.7 Coexistence

There are mainly two experimental approaches to measure the melting temperature of materials: static compression and shock experiments [100]. There have been large discrepancies between the two, indicating the difficulty of carrying out such experiments. Furthermore, neither approach can accurately determine the melting properties of materials at very high pressures. First-principles calculations can provide reliable results of melting properties. There are two possible techniques: the free energy approach and the coexistence method [98]. Both methods can either be used as a direct method or using an empirical model to mimic the liquid and the solid. Direct coexistence and coexistence using a potential are both detailed below.

2.7.1 Direct coexistence

The direct coexistence [101] method consists in simulating both liquid and solid in a cell. Once the liquid and the solid are in equilibrium, the average value of the pressure and temperature yield a point on the melting curve. To prepare the simulation, the perfect crystal is first thermalized at a temperature slightly below the expected melting temperature. Afterwards, half the atoms are free to evolve at a very high temperature until this half melts. The liquid is then rethermalized back to the initial guessed temperature. Finally, the system is allowed to evolve freely in the NVE ensemble. The system can either completely melt or solifidy, if E is not within the right range. Therefore, 'trial and error' steps are necessary to identify a coexistence range. This method is, however, extremely computationally expensive as it requires a very large number of atoms (i.e. a few hundred or thousand atoms are needed). An

alternative to reduce the computational price is to use an empirical potential.

2.7.2 Coexistence method with a reference model

Initially, an empirical reference model is fitted to the *ab initio* simulations, which are carried out under conditions close to the melting. Then, this reference model is used in simulations on very large systems to determine points on the melting curve. In practice, both the embedded atom model (EAM) [102] and the Stillinger-Weber model [103] were tested as reference models. The EAM can be expressed as:

$$U_{\text{ref}}(r_1, ...r_N) = \frac{1}{2}\varepsilon \sum_{i \neq j} \left(\frac{a}{r_{ij}}\right)^n - C\varepsilon \sum_i \left[\sum_{j \neq i} \left(\frac{a}{r_{ij}}\right)^m\right]^{\frac{1}{2}} \tag{58}$$

Where the first term on the right hand-side is a repulsive term and the second one is the embedding term. The reference model is chosen to mimic the *ab initio* system by adjusting the parameters a (characteristic length) , ε (energy scale), m (embedding exponent), n (repulsive component) and C (dimensionless coefficient) [104]. The Stillinger-Weber model can be expressed as:

$$V = \epsilon A[\sum_{<ij>} v_{ij}^{(2)} r_{ij} + \frac{\lambda}{A} \sum_{<ijk>} v_{ijk}^{(3)}(r_{ij}, r_{ik})] \tag{59}$$

Once the fit has been performed, a supercell is thermalized slightly below the expected melting temperature. Half the atoms are then fixed and the other half is melted by heating it to a very high temperature. To monitor the state of the cell, the density number is calculated. With half the atoms still fixed, the molten half is rethermalized to a temperature close to the expected melting

temperature. Finally, the fixed atoms are released and thermal velocities are assigned. The system is then allowed to evolve freely for a long time until both the solid and the liquid come into equilibrium thus yielding a point on the melting curve.

2.7.3 Correction to the coexistence

The coexistence method described above generates errors which can be due for instance to insufficient k-point sampling or incomplete basis sets. The use of a reference model introduces a new source of error due mainly to the differences between full *ab initio* and reference model calculations and this will necessarily incur errors in the melting temperature, which can be evaluated [105]. G^{ls} is the difference between the Gibbs free energy of the liquid and the Gibbs free energy of the solid at a given pressure and temperature. Therefore:

$$G^{ls}_{AI}(P,T) = G^{ls}_{\text{ref}}(P,T) + \xi \Delta G^{ls}(P,T) \tag{60}$$

Where Δ refers to a shift caused by changing U_{ref} to U_{AI}, $G^{ls}(P,T)$ represents the difference between the Gibbs free energies of the liquid and the solid and ξ is a parameter introduced to expand the T^{ref}_m as a power series [105]:

$$T^{\text{AI}}_m = T^{\text{ref}}_m + \xi T^{'}_m + \xi^2 T^{''}_m + ... \tag{61}$$

The *ab initio* melting temperature T^{AI}_m is the solution of $G^{ls}_{AI}(P,T) = 0$, which can be solved using the expansion in Equation 61. To first order, the melting

temperature shift is [106]:

$$\Delta T_m \simeq \frac{\Delta G^{ls}(T_m^{\text{ref}})}{S_{\text{ref}}^{ls}} \tag{62}$$

Where S_{ref}^{ls} is the entropy of fusion. The latter can be obtained by performing AIMD simulations of the solid and the liquid separately in the NVT ensemble using the same T as that of the coexistence simulations. These simulations generate the enthalpy of fusion H_{ref}, which can be inserted into: H_{ref}^{ls}=$T_m^{\text{ref}} S_{\text{ref}}^{ls}$ to get the reference entropy of fusion [104]. For calculations performed in the isothermal-isobaric ensemble, the shifts of the Gibbs free energies of the liquid and the solid can readily be evaluated using:

$$\Delta G \simeq < \Delta U >_{\text{ref}} - \frac{1}{2}\beta < \delta\Delta U^2 >_{\text{ref}} \tag{63}$$

Where $\delta\Delta U^2 \equiv \Delta U - < \Delta U >_{\text{ref}}$ and averages are taken in the reference ensemble. It is convenient to perform calculations at constant volume and temperature and for that reason, one can compute the shift of the Helmholtz free energy energy instead using Equation 63. To revert to the Gibbs free energy, one must use the following relation [105]:

$$\Delta G = \Delta F - \frac{1}{2} V \kappa_T (\Delta P)^2 \tag{64}$$

Where κ_T is the isothermal compressibility and ΔP is the pressure change upon replacing U_{ref} by U_{AI} at constant volume and temperature.

2.8 Z method

The Z method attempts to recreate how melting is measured in experiments. The method starts with a solid and the temperature is gradually increased. When the temperature is high enough the solid melts and it is readily observable as latent heat causes a temperature drop. There are drawbacks to this method which is why the theory of the Z method is not fully understood. Indeed, melting occurs usually from surfaces and defects in experiments whereas in a computational study the solid will remain in a metastable state after the temperature goes above the melting temperature. The Z method was introduced for the first time in [107] on Molybdenum where the initial configuration is a solid whose final state lies on the isochore corresponding to the fixed volume. The isochore is composed of 4 parts [107] : first, a solid which transforms into a superheated solid, a transition from the superheated solid state to the melting curve and finally, a liquid part. In theory, there is a maximum energy E_{LS} which can be given to a solid before it melts in the microcanonical ensemble (NVE - with N being the number of particles, V the volume and E the energy of the system). This energy corresponds to the limit of superheating temperature T_{LS}. If the energy is increased above E_m the solid then spontaneously melts. The latter leads to an increase in potential energy thus the temperature decreases [108]. After melting has occured the final temperature is the melting temperature T_m. At a fixed volume the various (E,T) points present a Z shape as shown in Figure 26. In practice, a molecular dynamics simulation is performed on a solid at different initial kinetic energies. The system is then allowed to evolve freely under the classical equations of motion until the temperature drops to T_m at the chosen pressure [109]. The Z method requires

long simulations and directly yields points (P, T_m) on the melting curve.

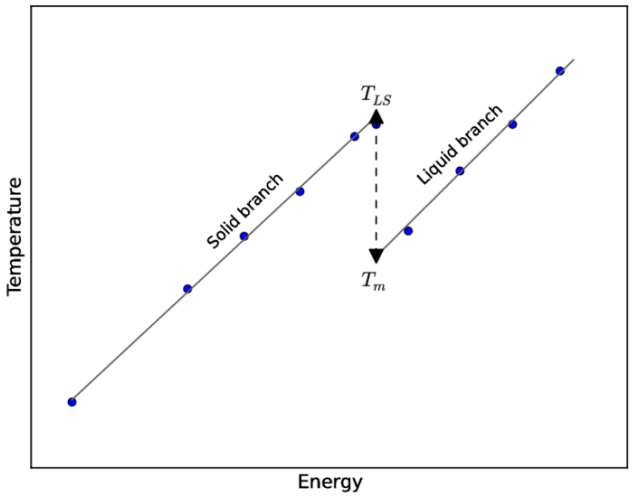

Figure 26: Schematic representation of the Z method. Figure taken from [108]

It is worth noting that a study [110] showed that the elapsed time τ_ω before melting is not correlated to initial conditions and therefore will differ in each run.The same study also concluded that the mean waiting time depends on the difference between the mean solid temperature T_{sol} and T_{LS}. Indeed melting occurs more rapidly as this difference gets larger. Furthermore, Alfè D. and Gillan [110] also showed that the mean waiting time can approximately be represented by $< \tau_\omega >= A/(T_{liq} - T_m)^2$ where T_m does not depend on T_{liq} nor N but A is inversely proportional to N. It is worth noting that the main assumption behind the Z method is that it only works if the simulation can be done for an infinite amount of time. Finally, caution is to be exercised as the Z method assumes that the final state of melting will be solely composed of liquid when in fact it could also be composed of a mix of solid and liquid [110].

3 Static Calculations

3.1 Method

In order to establish which phases are stable at zero temperature and finite pressures, one must first determine each phase's enthalpy F_0. The phase with the lowest enthalpy is thus the most stable one. Therefore, energy versus volume curves were produced and then fitted to a third order Birch-Murnaghan equation of state (Eq. 65), which then yielded the equilibrium volume V_0, bulk modulus B_0, minimum energy E_0 and first derivative of the bulk modulus B_0'.

$$E(V) = E_0 + \frac{9V_0B_0}{16}\left\{\left[\left(\frac{V_0}{V}\right)^{\frac{2}{3}} - 1\right]^3 B_0' + \left[\left(\frac{V_0}{V}\right)^{\frac{2}{3}} - 1\right]^2 \left[6 - 4\left(\frac{V_0}{V}\right)^{\frac{2}{3}}\right]^3\right\} \quad (65)$$

The pressure was then found using:

$$P(V) = \frac{3B_0}{2}\left[\left(\frac{V_0}{V}\right)^{\frac{7}{3}} - \left(\frac{V_0}{V}\right)^{\frac{5}{3}}\right]\left[1 + \frac{3}{4}(K_0' - 4)\left(\left(\frac{V_0}{V}\right)^{\frac{2}{3}} - 1\right)\right] \quad (66)$$

The enthalpy is defined as:

$$H = E(V) + PV \quad (67)$$

The enthalpies of various phases are then plotted as a function of pressure yielding the most stable one.

3.2 Structural properties of bcc and fcc

Given the large number of previous work done on bcc and fcc, calculations on these two phases were used as an initial test of the method's robustness.

Calculations on both bcc and fcc were performed using both the LDA and the GGA PBE. Two different number of valence electrons were also tested within the GGA (7 and 9 valence electrons). Fermi smearing was used throughout with a smearing parameter σ = 0.05 eV. Convergence was achieved using a 20x20x20 Monkhorst-Pack k-point grid and a plane wave cutoff of 400 eV. A plane wave cutoff of 800 eV and a k-point grid of 25x25x25 were tested to check convergence and energies were converged within 0.18 meV and 2.22 meV for bcc and fcc, respectively, as shown in Appendix A.1. The latter yielded a bulk modulus converged within 0.03 GPa, a lattice parameter converged within 0.002 Å, the minimum energy converged within 0.3 meV and the first derivative of the bulk modulus converged within 0.1 GPa as shown in Appendix A.1.The results obtained for the lattice parameter a, B_0, E_0 and $B_0^{'}$ for bcc and fcc are shown in Table 3 and 4, respectively.

Table 3: Calculated structural properties for bcc K at T = 0 K compared to previous theoretical and experimental data

a (Å)	B_0 (GPa)	B_0'	Reference
5.29	3.68	3.66	Full-potential linear augmented plane-wave [12]
5.22	4.30	2.79	Pseudopotential plane-wave [12]
5.30	6.08	1.87	Projector augmented wave method [12]
5.03	5.4	-	Full potential linearized augmented plane-wave [13]
5.04	4.8	-	LDA [14]
5.27	3.6	-	GGA PBE [14]
5.10	4.3	-	Pseudopotential method [15]
5.05	4.7	-	Augmented plane-wave with LDA [16]
5.33	2.96	4.06	Experimental [10]
5.22	3.4	-	Experimental [13]
5.29	3.6	5.6	This work - GGA
5.04	4.5	5.6	This work - LDA

Table 4: Calculated structural properties for fcc K at T = 0 K compared to previous theoretical and experimental data

a (Å)	B_0 (GPa)	B_0'	Reference
7.16	3.23	3.38	Full-potential linear augmented plane-wave [27]
6.52	4.52	2.8	Pseudopotential plane-wave [27]
6.34	5.2	-	Full potential linearized augmented plane-wave [13]
6.36	4.5	-	LDA [14]
6.65	3.5	-	GGA PBE [14]
6.40	4.4	-	Pseudopotential method [15]
6.35	4.6	-	Augmented plane-wave with LDA [16]
6.58	4.25	3.63	Experimental [10]
6.67	3.5	5.5	This work - GGA
6.36	4.5	5.5	This work - LDA

The results for both GGA and LDA were found to be in excellent agreement with previous calculations, thus providing an initial validation of the method used. It is worth noting, however, that the LDA significantly underestimates the equilibrium lattice parameter compared to experimental results whereas GGA slightly overestimates it. As for the bulk modulus, it was found that GGA calculations yielded a value closer to the one determined experimentally as was previously found by [14].

3.3 Transition pressure bcc-fcc

The transition pressure at which bcc transforms into fcc was obtained by plotting the enthalpy of both structures with respect to pressure, which is shown in Figure 27, which exhibits a transition pressure of 11.3 GPa. There has been some debate as to whether bcc or fcc was more stable at zero pressure and temperature. Figure 27 exhibits bcc as the most stable one albeit very small energy differences.

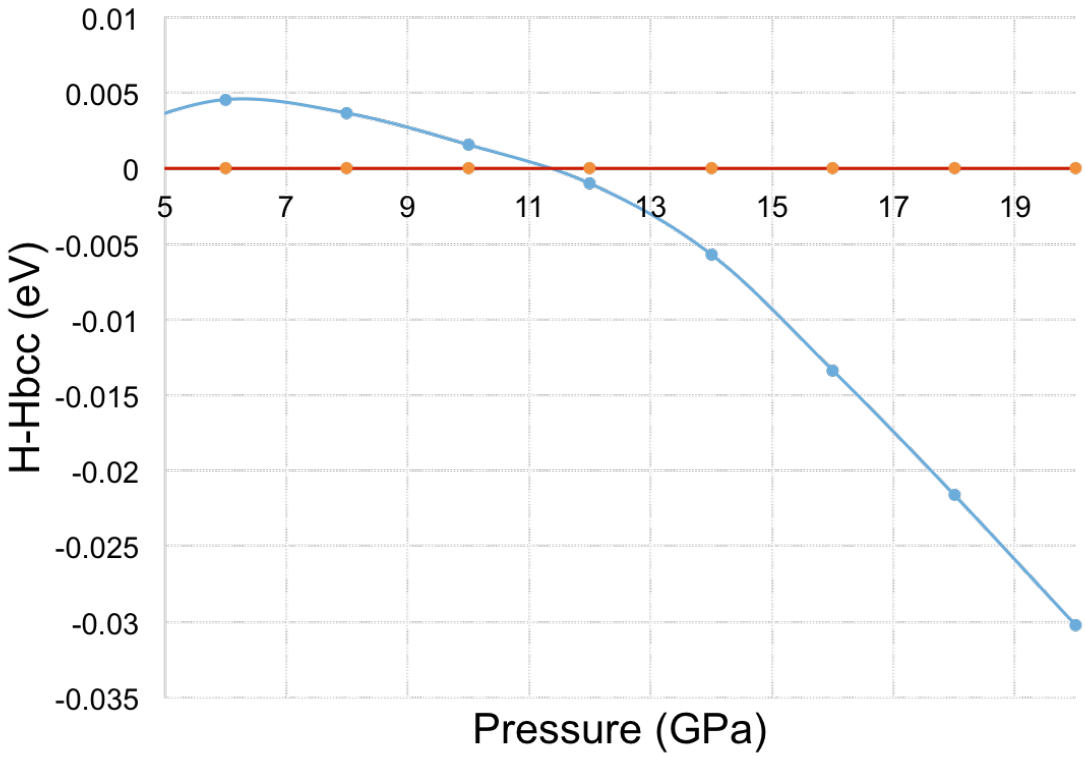

Figure 27: Enthalpy of fcc with respect to the enthalpy of bcc plotted against pressure where the blue line represents the enthalpy of fcc and the orange line is the enthalpy of bcc. It can be seen that the transition from fcc to bcc occurs at 11 GPa.

The transition pressures obtained with the GGA PBE and the LDA are shown in Table 5 below, along with previous experimental and theoretical results.

Table 5: Calculated transition pressures for fcc K at T = 0 K compared to previous theoretical and experimental data. (PV and SV stand for 7 and 9 valence electrons, respectively)

Parameters	Transition pressure (GPa)
PV GGA	11.4
SV GGA	11.3
PV LDA	10.7
SV LDA	10.9
Experimental [8]	11
Experimental [111]	11.4
Previous calculations [17]	11.6
Previous calculations [20]	10.74

As shown in Table 5, the difference between 7 and 9 valence electrons is very small, however, the difference between the use of GGA and LDA is more noticeable and GGA yields results closer to the experimental ones.Therefore, it was deemed reasonable to use the GGA for the subsequent calculations.

3.4 Bain Path

Experiments found bcc to be the most stable structure at 0 GPa and most theoretical studies [20] also found bcc to be the most stable at 0 GPa and 0 K. Nevertheless, some theoretical studies [12] found fcc to be more stable. This difference was attributed to the temperature difference between experiments and calculations. To reinforce results the bcc-fcc transition was investigated as a Bain path. The latter describes the phase change as martensitic change where the initial cell is a body centered tetragonal (bct) whose c/a ratio changes continuously. The calculations for the bct unit cell containing 2 atoms were performed using a 19x19x19 Monkhorst-Pack set of Brillouin-zone sampling wavevectors within the GGA which resulted in energy converged to 5 meV. The results can be seen in Figure 28, which shows the calculated energy as a function of the c/a ratio at 3 different volumes 61, 70 and 112 Å^3 corresponding approximately to pressures of 0, 10 and 16 GPa, ($\pm$ 1 GPa) respectively. There are two minima, one at $c/a = 1$ and $c/a = \sqrt{2}$ corresponding to the bcc and fcc structures, respectively. At 0 GPa, Figure 28 shows that bcc is in fact more stable, validating our first approach although uncertainties could allow fcc to be more stable. Previous calculations of this Bain path [12] it was found that at 0 GPa, the fcc structure was more energetically favourable, which could be due to the fact that the work of [12] was performed at constant pressure whereas this work was done at constant volume. Be that as it may, both works exhibit two minima at zero pressure and temperature and with increasing pressure the local minimum at $c/a = 1$ disappears and the minimum at $c/a = \sqrt{2}$ dominates, meaning the bcc structure is no longer stable.

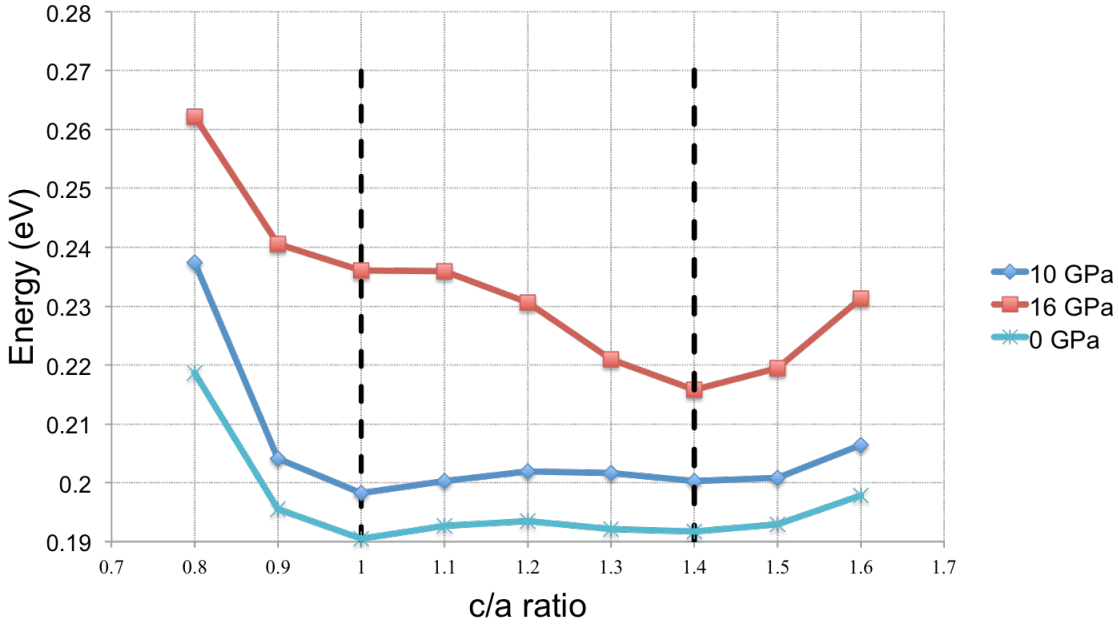

Figure 28: Energy as a function of the c/a ratio of bct illustrating Bain path from which it can be seen that the bcc phase is more stable at 0 GPa but as the pressure increases fcc becomes more stable.The curves are offset for a better view.

3.5 Incommensurate host-guest structure

3.5.1 Introduction

As mentioned previously, the third phase of potassium, referred to as KIIIa hereafter, is an incommensurate host-guest structure with a body-centered host cell with $a_H = 9.767$ Å and $c_H = 4.732$ Å at 22.1 GPa and the guest structure was identified as a C-face centered tetragonal structure with $a_H = a_G$ and $c_G = 9.767$ Å as determined experimentally [36]. The structure is shown in Figure 29.

A transition to a second composite host guest structure (KIIIb) was also

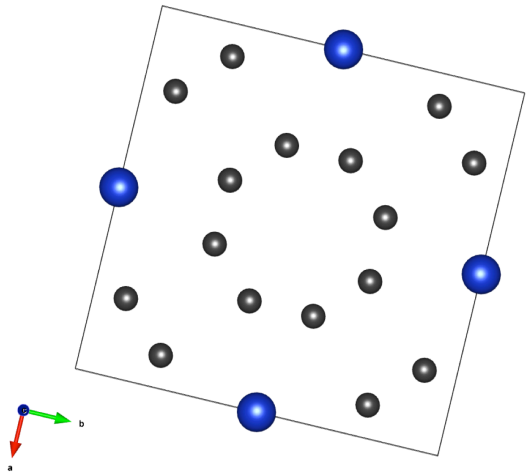

Figure 29: KIIIa structure, where the host atoms are shown in grey and the guest atoms are shown in blue.

observed at 30 GPa using x-ray powder and single-crystal diffraction [36]. This second phase consists of the same host as KIIIa but a guest structure, which was indexed on an A-centered orthorombic lattice with $a_G = 6.57$ Å , $b_G = 13.174$ Å and $c_G = 2.789$ ÅṪhe same experimental study also observed a reentrant phase transition at 39.7 GPa back to the guest structure of KIIIa. There are no theoretical work on KIIIa and KIIIb therefore there is no calculation of their enthalpies due to their incommensurate nature.

3.5.2 Enthalpies of KIIIa and KIIIb

Lundegaard *et al.* [36] showed that the c_H/c_G goes through the commensurate value of $8/5$ thus allowing enthalpy calculations. The approximate periodic structure was therefore constructed by merging a 1x1x5 supercell of the guest lattice and a 1x1x8 supercell of the host lattice, which resulted in a primitive cell of 48 atoms. The enthalpies of both host guest structures were thus calcu-

lated using a plane wave cutoff of 400 eV, a 2x2x2 k-point grid, which yielded energies converged to better than 5 meV as shown in Appendix A.2. Fermi smearing was used with a smearing parameter of 0.05 eV and calculations were carried out using the GGA. The results exhibit a first transition at 29 GPa as shown in Figure 30, followed by a second transition at 48 GPa as shown in Figure 31. Hence, the reentrant transition $KIIIa \rightarrow KIIIb \rightarrow KIIIa$ is readily observed theoretically, which concurs with the experimental data.

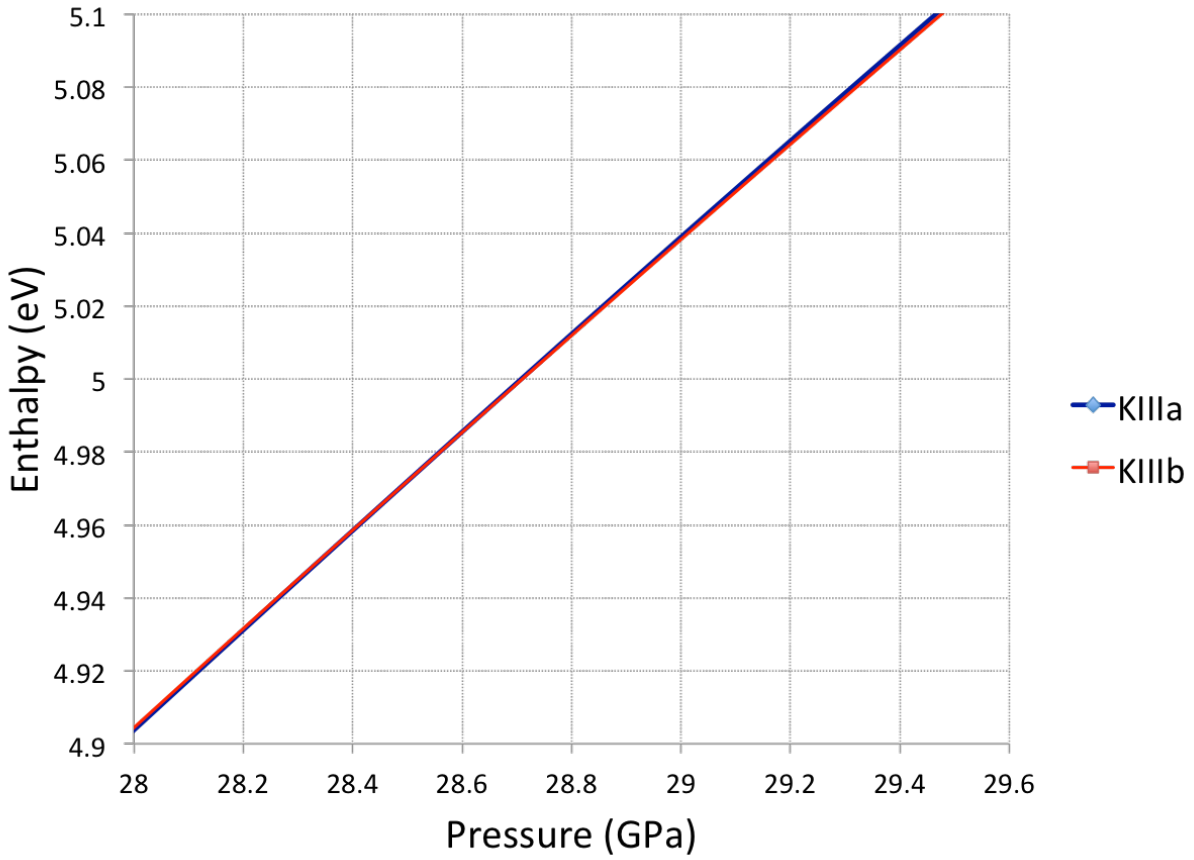

Figure 30: Enthalpy as a function of pressure for KIIIa and KIIIb exhibiting the first transition at 29 GPa

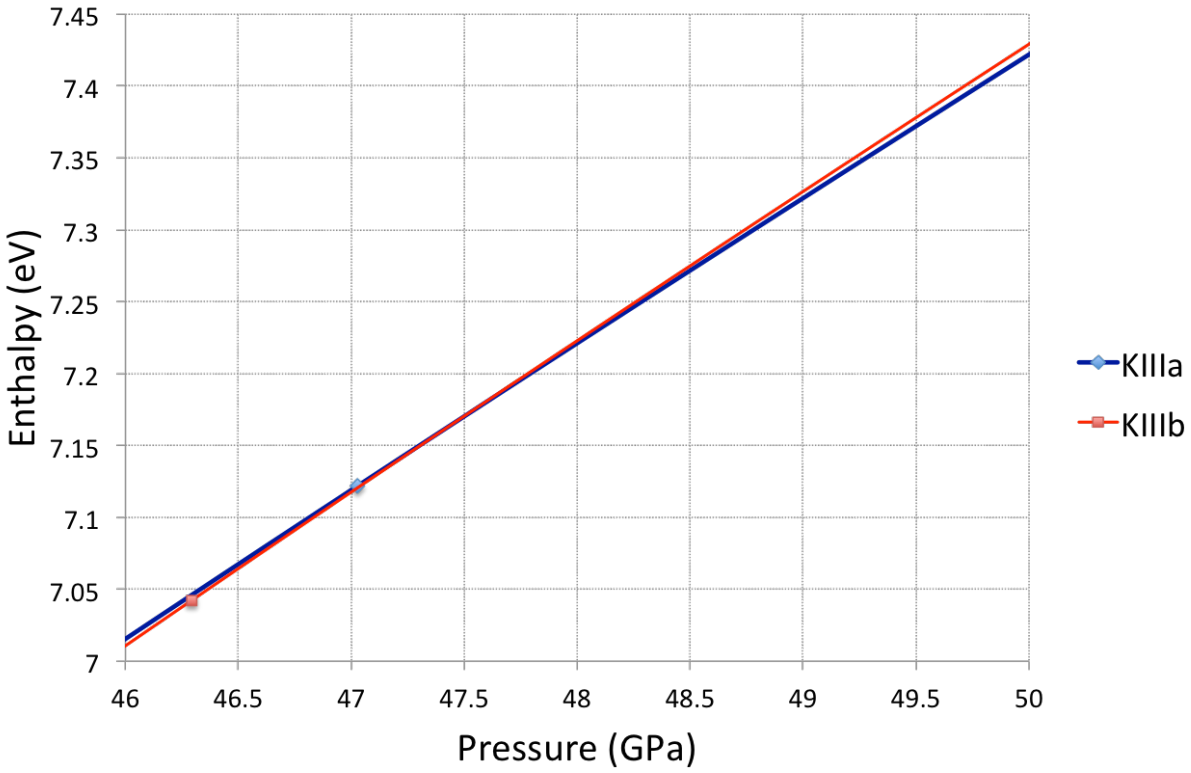

Figure 31: Enthalpy as a function of pressure for KIIIa and KIIIb exhibiting the second transition at 48 GPa

3.5.3 Comparison with ferromagnetic phases and hP4

There has been some debate as to whether KIIIa was truly the post-fcc most stable phase. In the same pressure range, some samples [37] experimentally identified a metastable phase hP4, as was previously found in Na [112]. Furthermore, at pressures between 18.5 and 22 GPa a ferromagnetic ground state was also suggested justified by the possible lowering of the electronic energy by magnetic ordering [113]. Therefore, to verify which phase is indeed most stable after fcc, the enthalpy of hP4 was calculated. Spin-polarised cal-

culations of the simple cubic (scFM) and cI16 were also performed to compare them to the enthalpy of KIIIa. Calculations were performed with a plane wave cutoff of 400 eV using the GGA and Fermi smearing with $\sigma = 0.05$ eV. The k-point grid used was 20x20x12 for hP4 and 15x15x15 for the spin polarised calculations on sc and cI16. Energies were converged within 1 meV as shown in Appendix A.2. Results are shown in Figure 32. As can be seen, the enthalpy curves cross at shallow angles, thus illustrating why some studies found these phases stable. Nevertheless,this study shows KIIIa still remains the most stable structure at these pressures.

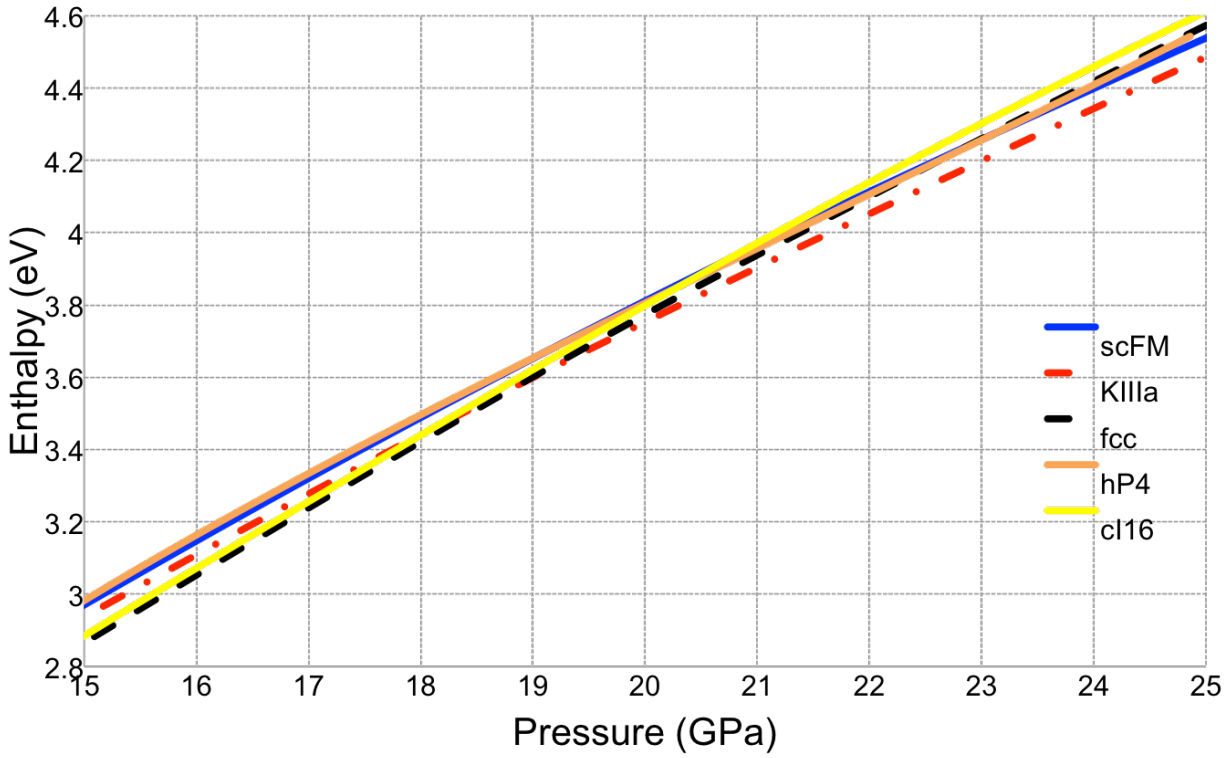

Figure 32: Enthalpies of fcc (black dashed), scFM (solid blue), KIIIa (dashed red), hP4 (orange solid) and cI16 (yellow solid) showing KIIIa to be the most stable

3.6 Phase transitions above 40 GPa

The post-KIII phases, as determined experimentally, are oP8, tI4 and oC16 and transitions were observed at 54 GPa, 90 GPa and 96 GPa, respectively. *Ab initio* calculations were also carried out to determine these transition pressures and two studies [38, 40] found very similar results, that is, a transition from oP8 to tI4 at 66 GPa followed by a transformation from tI4 to oC16 at 81 GPa. Evidently, there are discrepancies between theoretical and experimental results, which will be discussed later.

3.6.1 Calculation details

Calculations on these phases were done using the GGA PBE, a planewave cutoff of 400 eV and Fermi smearing with a smearing parameter of 0.05 eV. The k-point grids used were 16x10x8, 16x16x10 and 12x12x12 for oP8, tI4 and oC16, respectively.These parameters showed energies converged within 2, 0.5 and 0.2 meV for oP8, tI4 and oC16, respectively, as shown in Appendix A.3. The enthalpy of oP8 was compared to those of KIIIa and KIIIb as seen in Figure 33. The corresponding energy-volume curves are shown in Figure 34. This shows that KIIIa transforms into KIIIb at 29 GPa but before the reentrant transition from KIIIb to KIIIa can occur at 48 GPa, oP8 becomes more stable at 41.7 GPa. Hence, the order of the phases previously reported [38, 40] is now changed.

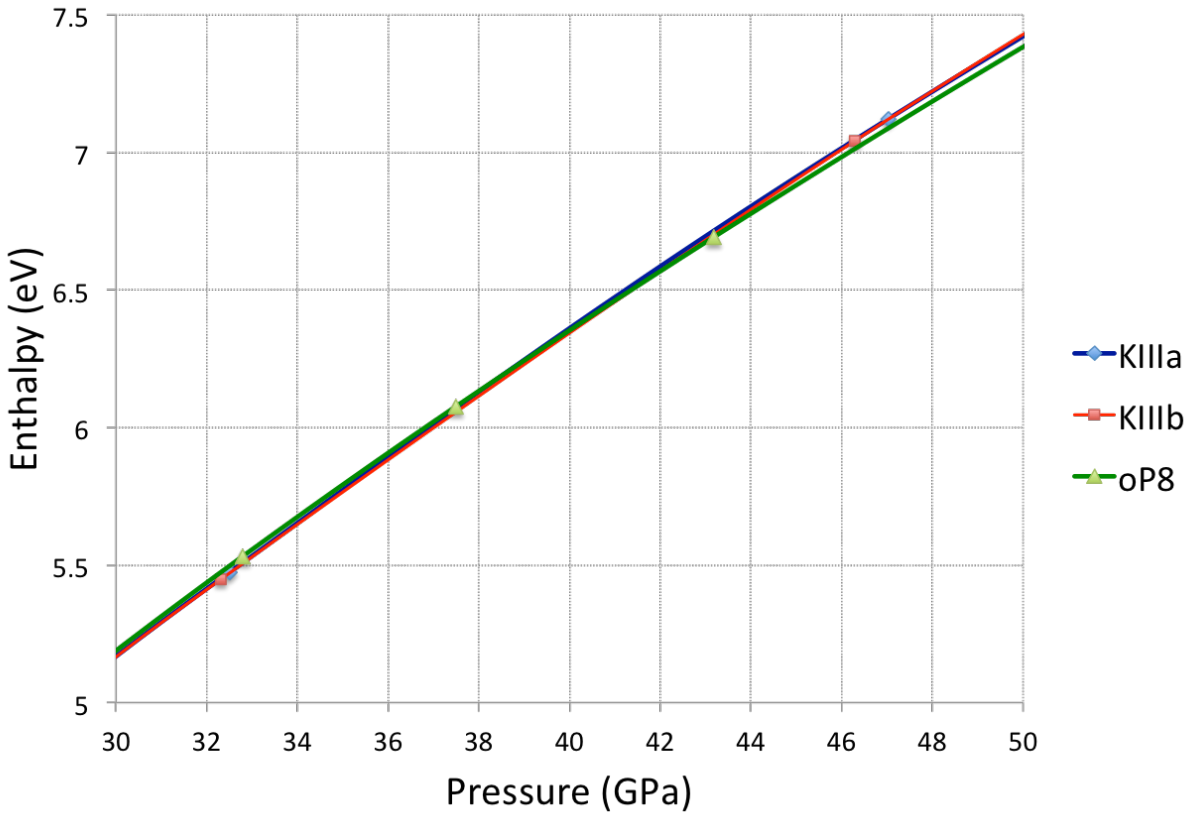

Figure 33: Enthalpies of KIIIa, KIIIb and oP8 as a function of pressure showing oP8 becomes more stable at 41.7 GPa, before the reentrant transition from KIIIb to KIIIa at 48 GPa.

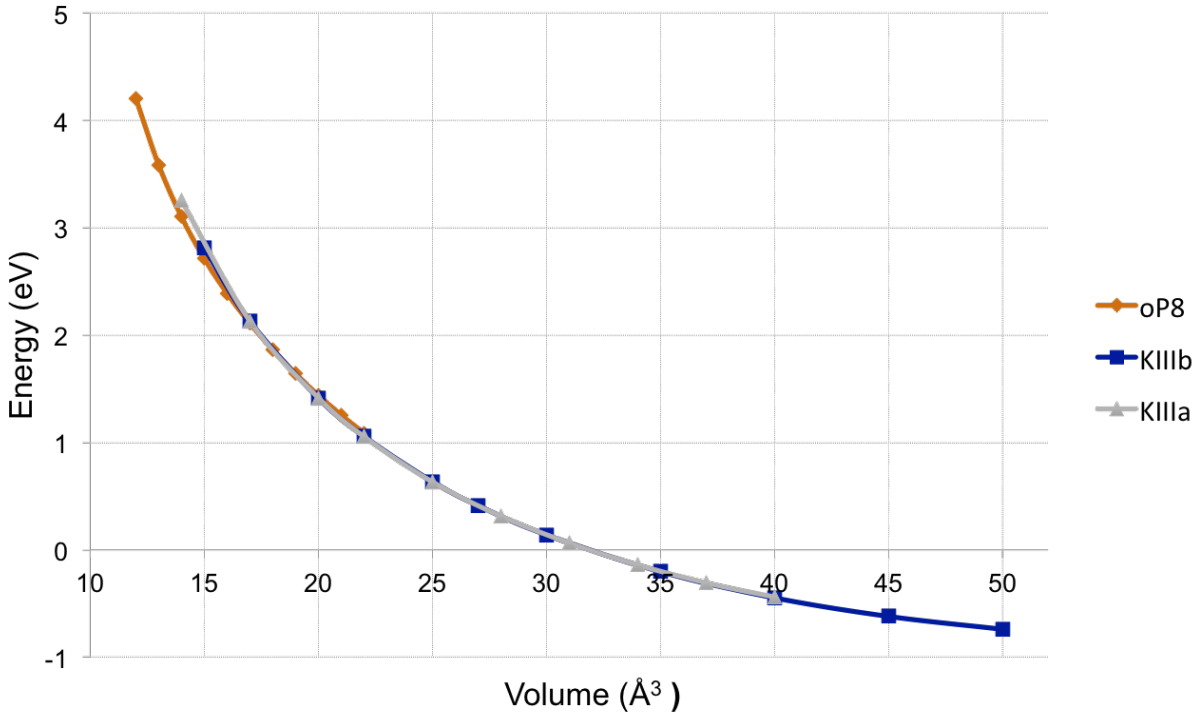

Figure 34: Energy-volume curves of KIIIa, KIIIb and oP8

The enthalpies of tI4, oC16 and oP8 were also determined and the results show that oP8 has a lower enthalpy than tI4 until 57 GPa as shown in Figure 35. The energy volume curves of oP8 and tI4 are also shown in Figure 36.

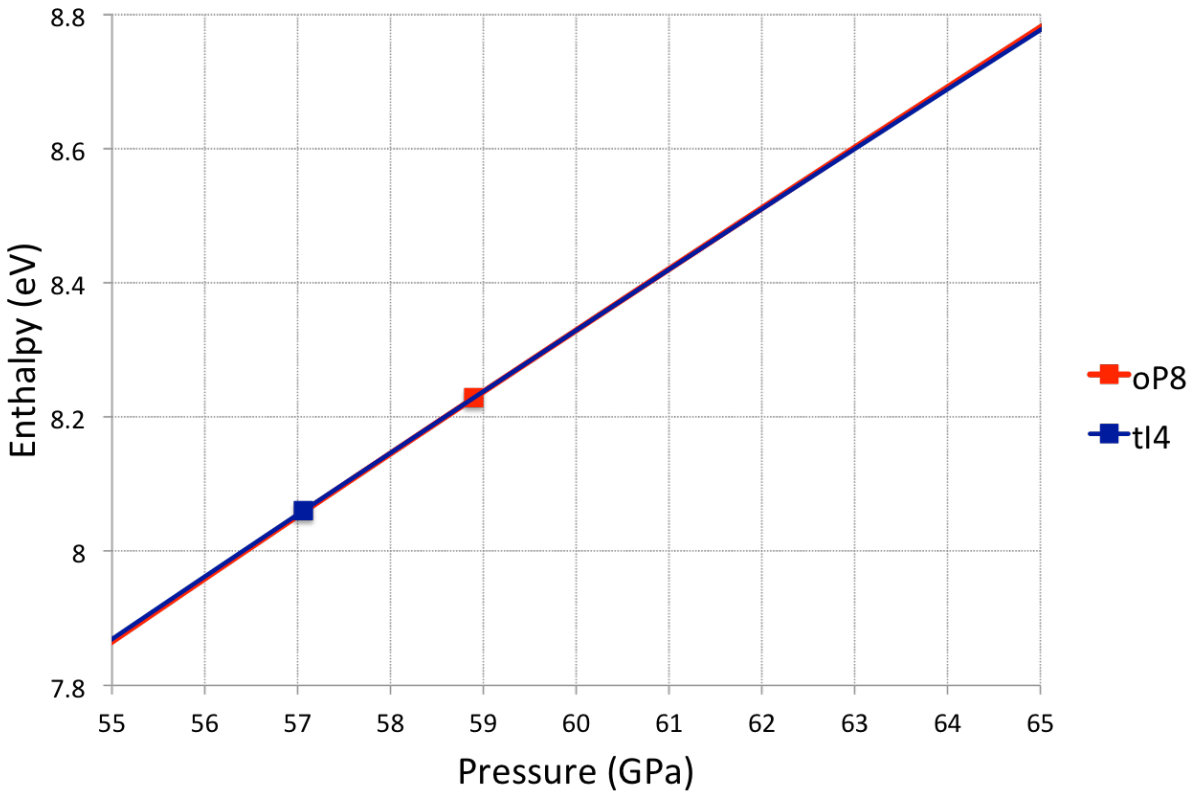

Figure 35: Enthalpies of oP8 and tI4 as a function of pressure showing the transition at 57 GPa.

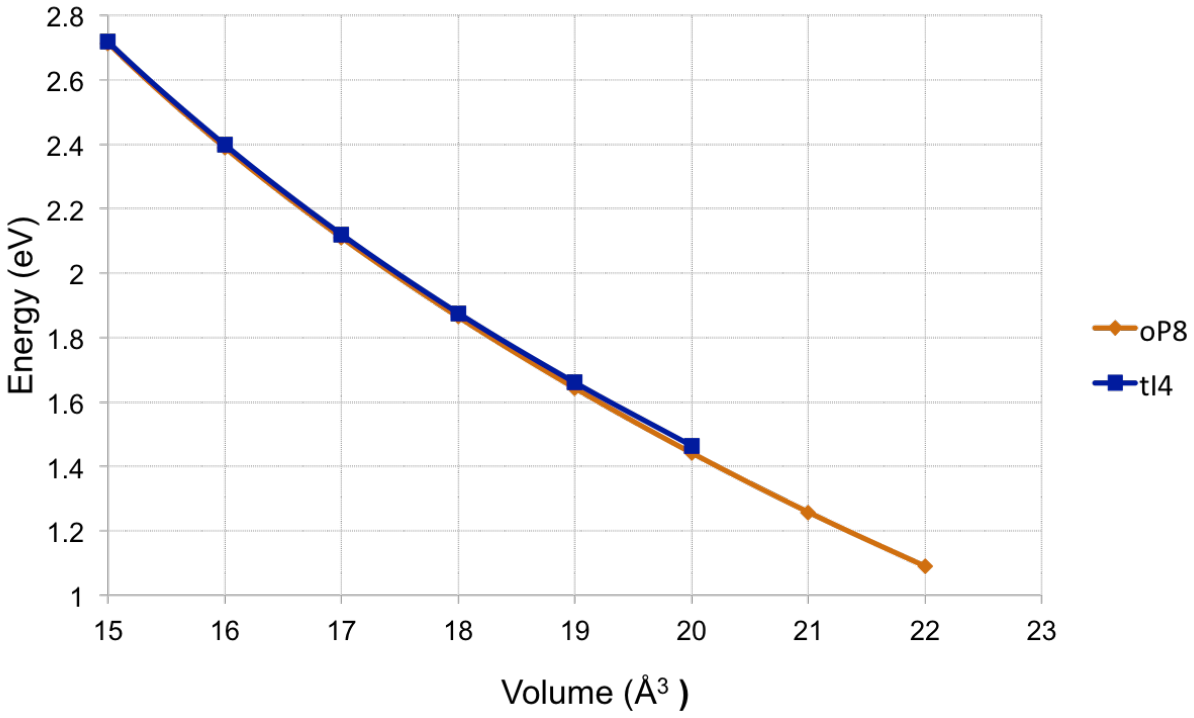

Figure 36: Energy-volume curves of oP8 and tI4

At 81 GPa, our calculations clearly show that the enthalpy of tI4 becomes unfavourable with respect to the oC16 structure as seen in Figure 37. These results are in excellent agreement with previous studies hence fairly distant from experimental results.

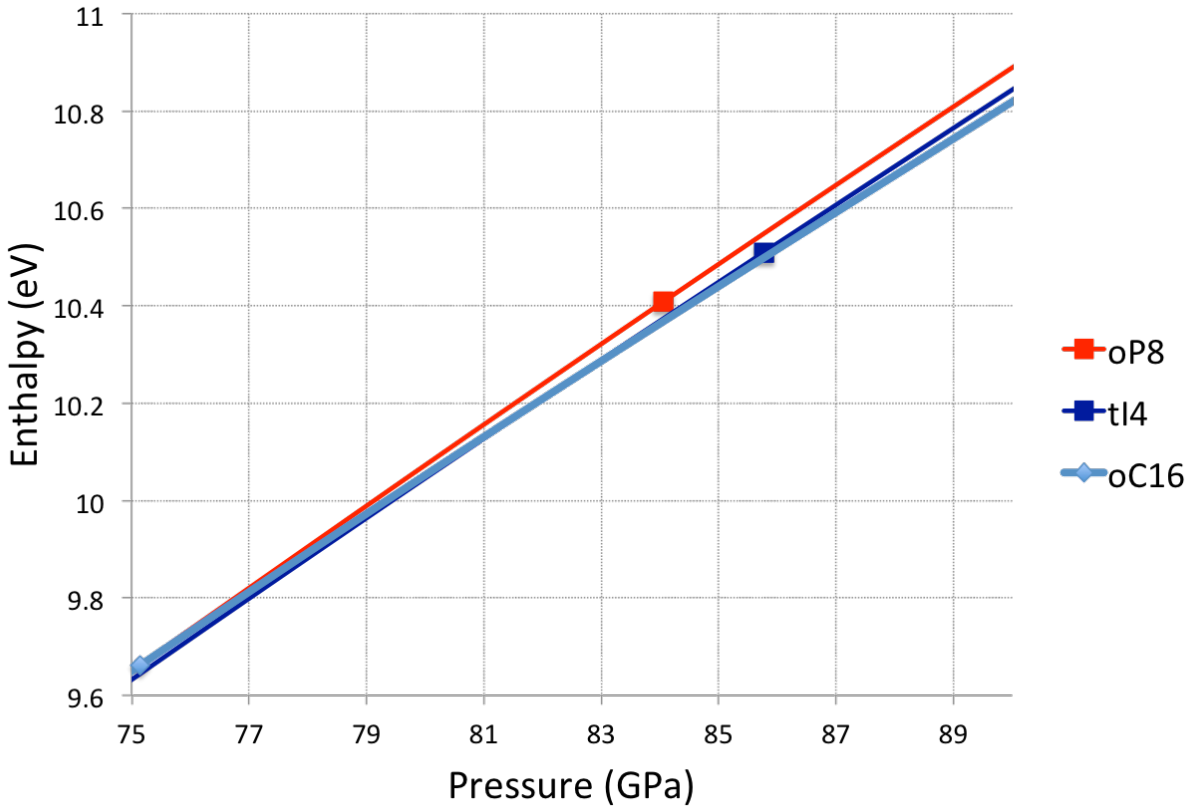

Figure 37: Enthalpies of tI4 and oC16 as a function of pressure showing the transition at 81 GPa.

3.6.2 Disagreement with experiments

The differences between experiments and these theoretical calculations yield a rearranging of the phase order. Indeed, the ordering of the transitions differ from that found experimentally. Instead of the following found via previous calculations and experiments:

$$fcc \rightarrow KIIIa \rightarrow KIIIb \rightarrow KIIIa \rightarrow oP8 \rightarrow tI4 \rightarrow oC16 \tag{68}$$

Enthalpy calculations in this study yielded the following order:

$$fcc \rightarrow KIIIa \rightarrow oP8 \rightarrow tI4 \rightarrow oC16 \tag{69}$$

It is worth noting that the transition from KIIIb back to KIIIa found here at 48 GPa was experimentally found at 39.7 GPa [36] hence if these results had found a value closer to the experimental one then the order would be unchanged. It was suggested that the discrepancies between experiments and theory might be due to the fact that the GGA poorly describes the energy differences when the type of bonding is quite different as seems to be the case between oP8 and tI4. To address the latter, other functionals were used to recalculate the enthalpies of all phases (excluding bcc and fcc) and the resulting transition pressures are shown in Table 6. Although the functionals do have an impact on the transition pressures, none adequately represents the experimental results.

Table 6: Transition pressure between the phases oP8, tI4 and oC16 with respect to different exchange correlation (XC) functionals

	Transition Pressure (GPa)	
XC Functional	oP8-tI4	tI4-oC16
optPBE-vdw [81]	68	78
optB88-vdw [81]	66	76
PBEsol	43	71
LDA	25	74
PBE	57	81

3.7 Conclusion

This chapter show the results of calculations at 0 GPa, more specifically, bcc transforms into the fcc structure at 11 GPa, then KIIIa becomes more stable at 19 GPa. The reentrant transition KIIIa - KIIIb - KIIIa is readily observed as was in experiments, however, oP8 becomes energetically more favourable than KIIIb before the reentrant transition can occur thus the order of the phase transition observed is: bcc - fcc - KIIIa - KIIIb - oP8. At 57 GPa, tI4 becomes more stable until 81 GPa, at which point it transforms into oC16. The transitions oP8 - tI4 - oC16 are in excellent agreement with previous calculations but differ from experimental findings. The next chapter will study the same transitions at finite temperatures using the quasi-harmonic approximation.

4 Quasi-Harmonic Calculations

4.1 Calculations details

Calculations were carried out within the framework described in Part I.4. The force constant matrix was determined using the small displacement method thus yielding the dynamical matrix and hence the phonon frequencies, which are the square root of the eigenvalues of the dynamical matrix.

Tests were carried out on bcc and fcc with respect to cell size (8 - 64 atoms), number of k-points (up to 8x8x8) and displacement size (0.00423 - 0.043 Å) at a volume per atom of 68 $Å^3$ and 0 K.

Table 7: Supercell sizes and k-point grid tested for the calculation of the harmonic contribution to the free energy of oP8, tI4 and oC16

Phase	Supercell size	Gamma centered k-point grid
oP8	1x1x1	12x8x6
	2x1x1	6x8x6
tI4	2x2x1	8x8x10
	4x4x2	4x4x5
oC16	1x1x1	12x12x12
	2x2x2	6x6x6

4.2 Phonon frequencies of bcc and fcc

Convergence of the phonon frequencies to within less than 6 GHz was achieved using a 4x4x4 supercell with a 4x4x4 MP k mesh in the BZ along with a displacement of 0.04 Å and a plane-wave cutoff of 500 eV. Figure 38 shows the calculated phonon frequencies plotted with the experimental inelastic neutron scattering from [114].

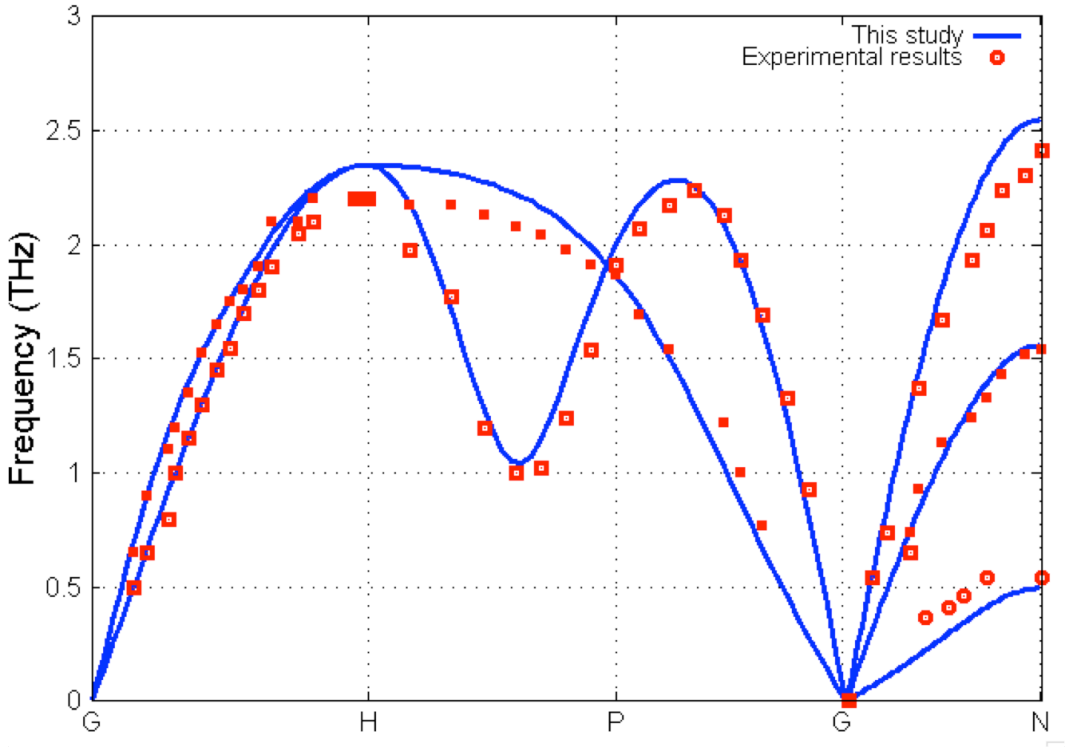

Figure 38: Calculated phonon frequencies for bcc K (line) along with experimental results [114] (squares) and previous calculations [12] (circles)

It is evident from Figure 38 that the agreement with previous calculations [12] is excellent and it agrees with the experimental results within 6 % or less. Given the good agreement with previous work, both experimental and theoret-

ical, calculations were also carried out at a higher pressure of 15 GPa for the bcc phase with confidence and the results can be seen in Figure 39. Using Fermi smearing with a smearing parameter of 0.2 yields an excellent agreement with previous calculations [12], which are shown in Figure 5. Indeed upon pressure increase TA phonon instabilities occur as they become imaginary around 15 GPa, which illustrates a structural instability.

However, smaller smearing parameters lead to different phonon frequencies along the ΓN path as can be seen in Figure 39. When σ is decreased, there is still a softening of the phonons but they are no longer imaginary.

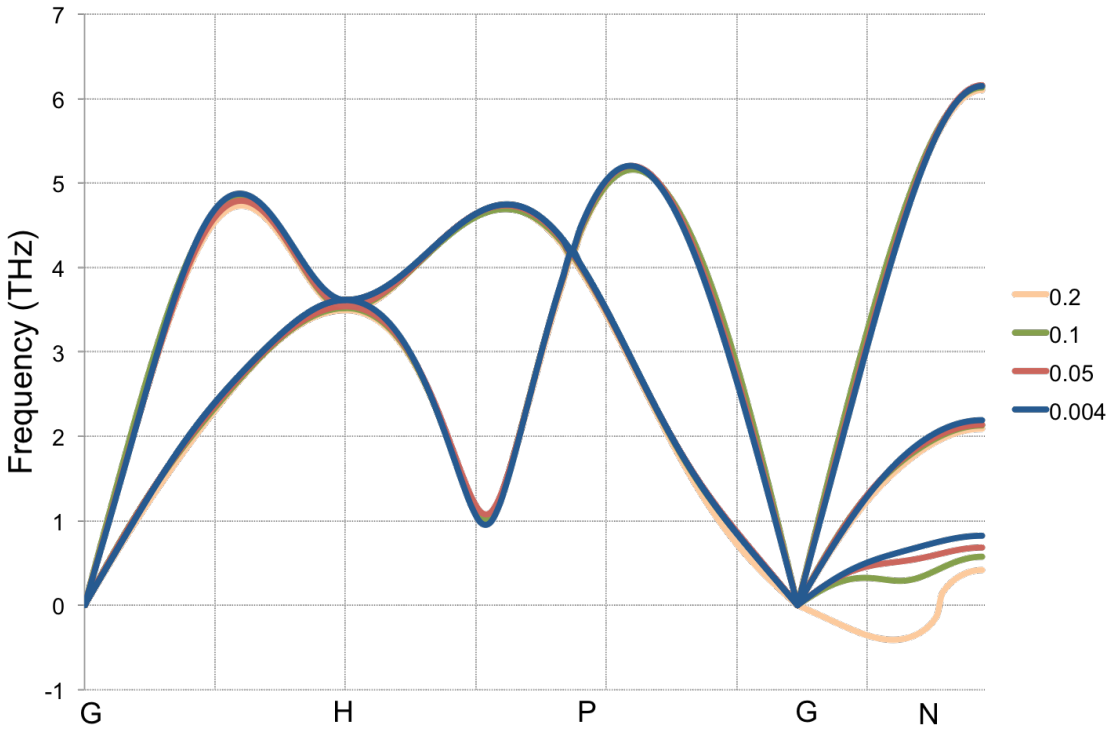

Figure 39: Calculated phonon frequencies for bcc K at 15 GPa for different smearing parameters σ=0.004, 0.05, 0.1 and 0.2.

Calculations were carried out on fcc at different pressures. The results are

in fairly good agreement with previous calculations [27] when $\sigma = 0.2$ as, similarly to the bcc phase, phonon softening occurs upon pressure increase and become imaginary, which can be an indicator of structural change as shown in Figure 40.

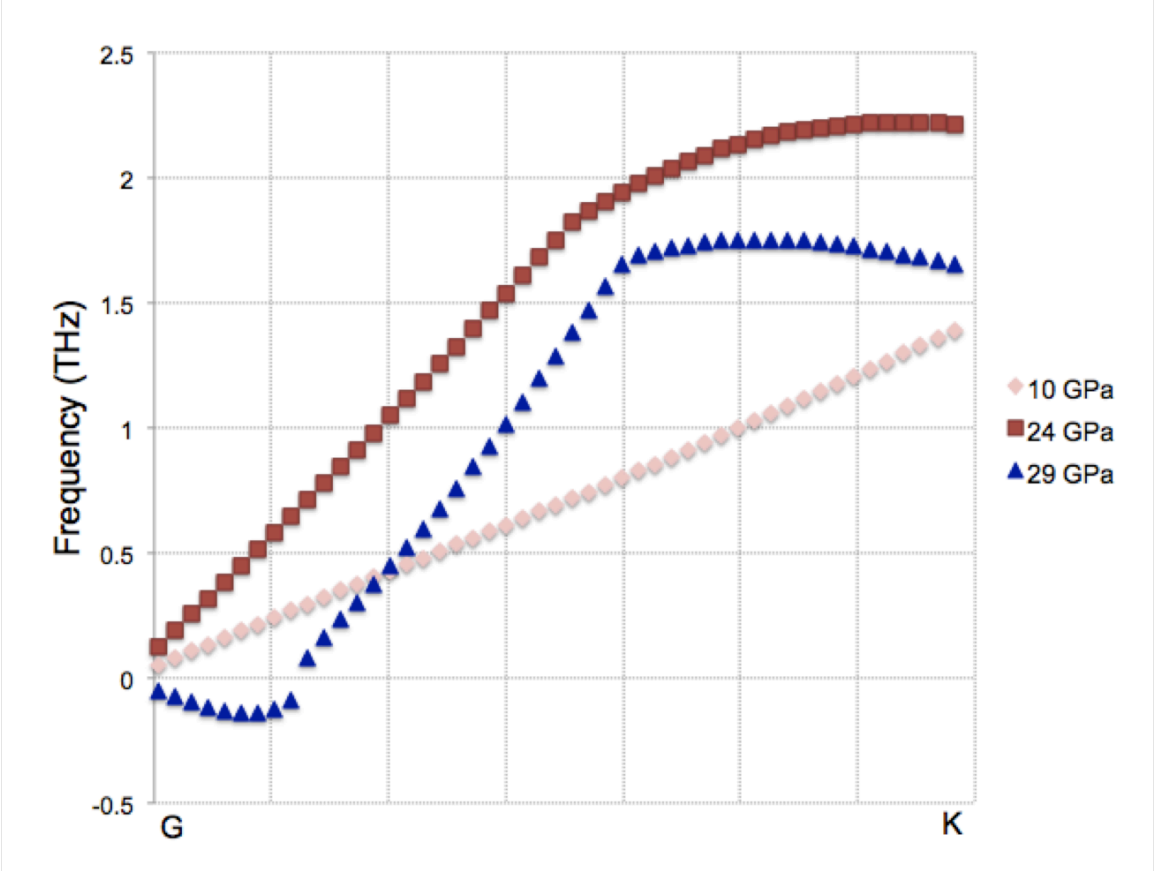

Figure 40: Phonon dispersion curves of fcc for different pressures (10, 24 and 29 GPa). Obtained with a 4x4x4 SC within the GGA PBE and with a displacement of 0.04 Å

Convergence tests with respect to σ were carried out for fcc and results are shown in Figure 41, which proves that the softening previously reported by [27] was indeed an artefact caused by using a large σ.

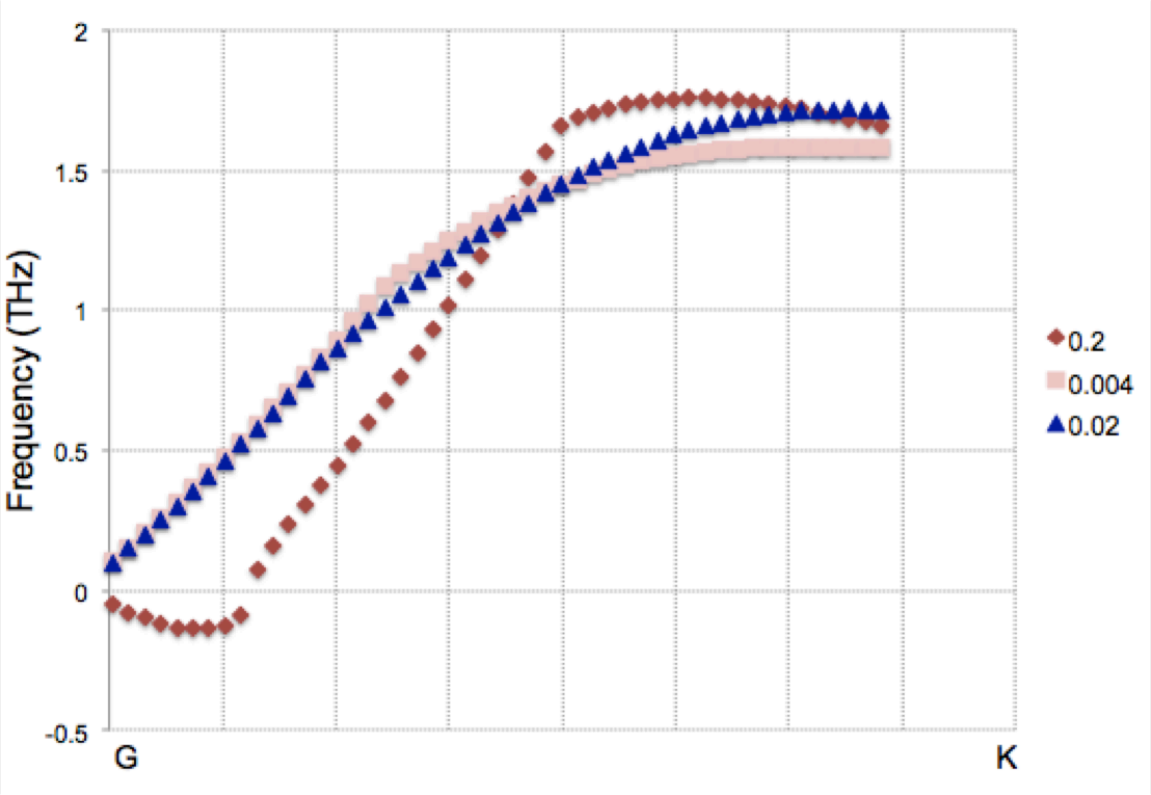

Figure 41: Phonon dispersion curves of fcc for different smearing parameters (σ =0.2, 0.02 and 0.004 eV). Obtained with a 4x4x4 SC within the GGA and with a displacement of 0.04 Å at 29 GPa

Using these frequencies, the harmonic contribution to the free energy of both bcc and fcc were obtained and results are shown in Figure 42 along with previous experimental and theoretical work. It can be seen from the nearly straight lines obtained that the phonon contribution to the free energy difference between neighbouring phases is negligible at such pressures and temperatures.Indeed the transition pressure at 0 K is essentially the same at 400 K. These results also agree well with those of Fabbris et al. [115], who found the transition from bcc to fcc to be 13 GPa $\pm$ 1 GPa at 10 K and 11 GPa at

300 K. Here we find 11.4 GPa at 0 K and 11.3 at 300 K.

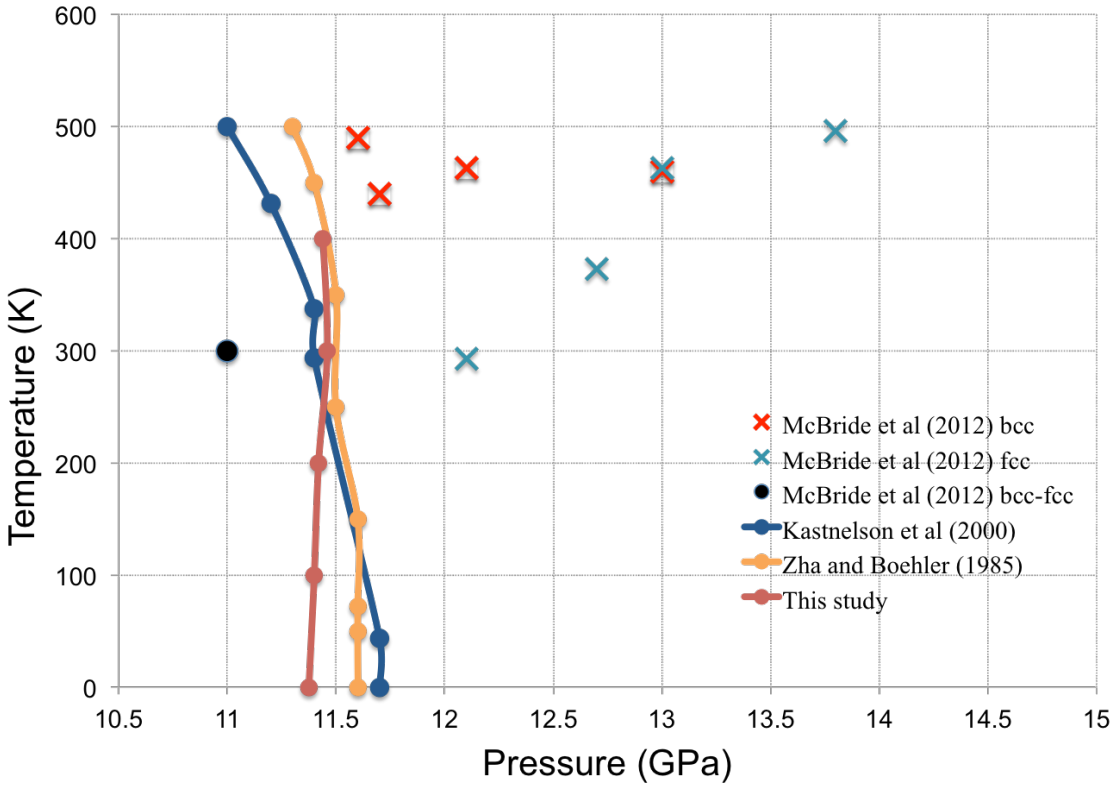

Figure 42: Solid phase boundaries calculated in this study (orange) with 4x4x4 supercells, 4x4x4 Γ centered k-point grid and a plane wave cutoff of 500 eV. These results are compared to previous experimental and theoretical studies.

4.3 Phonon DOS of higher pressure phases

The harmonic contribution to the free energy of the higher pressure phases were also calculated using the GGA to the exchange correlation functional with 9 valence electrons and a plane wave cutoff of 400 eV. Convergence tests were carried out on the supercell sizes and k-points grid as shown in Table 8. Comparisons with previous calculations and experimental results were

unfeasible in this case as these transitions were not previously established at finite temperatures though our results found the phonon contribution to the free energy difference to be negligible.

Table 8: Supercell sizes and k-point grid tested for the calculation of the harmonic contribution to the free energy of KIIIa, KIIIb, oP8, tI4 and oC16

Phase	supercell size	Gamma centered k-point grid
KIIIa	1x1x1	4x4x4
KIIIb	1x1x1	2x2x2
oP8	2x1x1	6x8x6
tI4	4x4x2	4x4x5
oC16	2x2x2	6x6x6

The phonon frequencies of the KIII, oP8, tI4 and oC16 structures were determined using the quasi-harmonic approximation with central differences instead of forward differences in order to reduce numerical noise. The results are shown in Figure 43 from which we can see there are no imaginary phonons thus eliminating the possibility of mechanical instability.

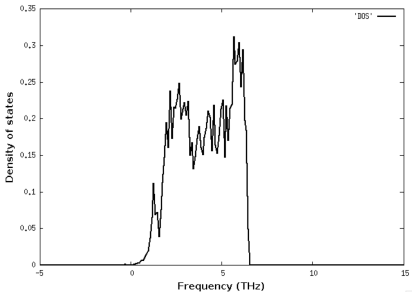

(a) Phonon DOS of KIIIa

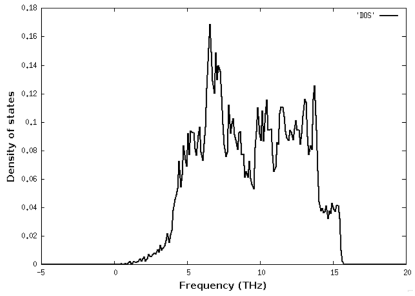

(b) Phonon DOS of oC16

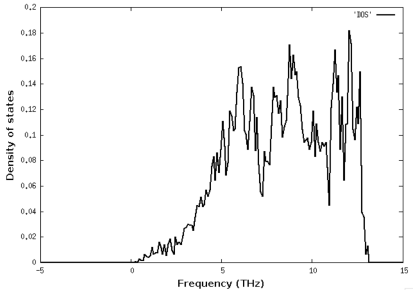

(c) Phonon DOS of tI4

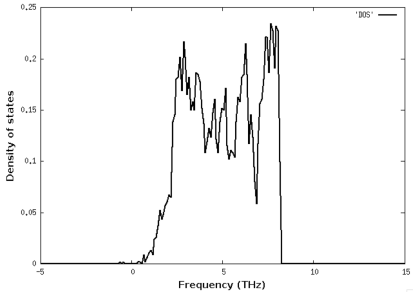

(d) Phonon DOS of KIIIb

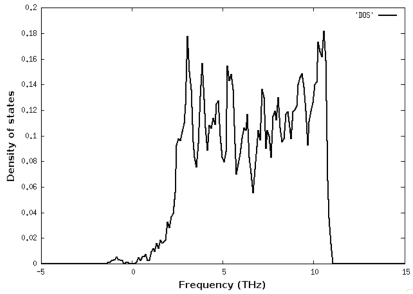

(e) Phonon DOS of oP8

Figure 43: Phonon DOS of KIIIa, KIIIb, oP8, tI4 and oC16 showing there are no negative frequencies.

Using these phonon calculations yielded the Gibbs free energies of all phases at temperatures ranging from 0 to 400 K thus allowing the determination of the solid phase diagram at finite temperatures as shown in Figure 44 for KIIIa and KIIIb and Figure 45 for oP8, tI4 and oC16. The discrepancy

with experimental results remains as the differences in transition pressures is causing the phases to switch order. Moreover, the phase diagram shows that the transition lines are essentially vertical, indicating that phonons contribute very little if at all to the free energy differences between neighbouring phases.

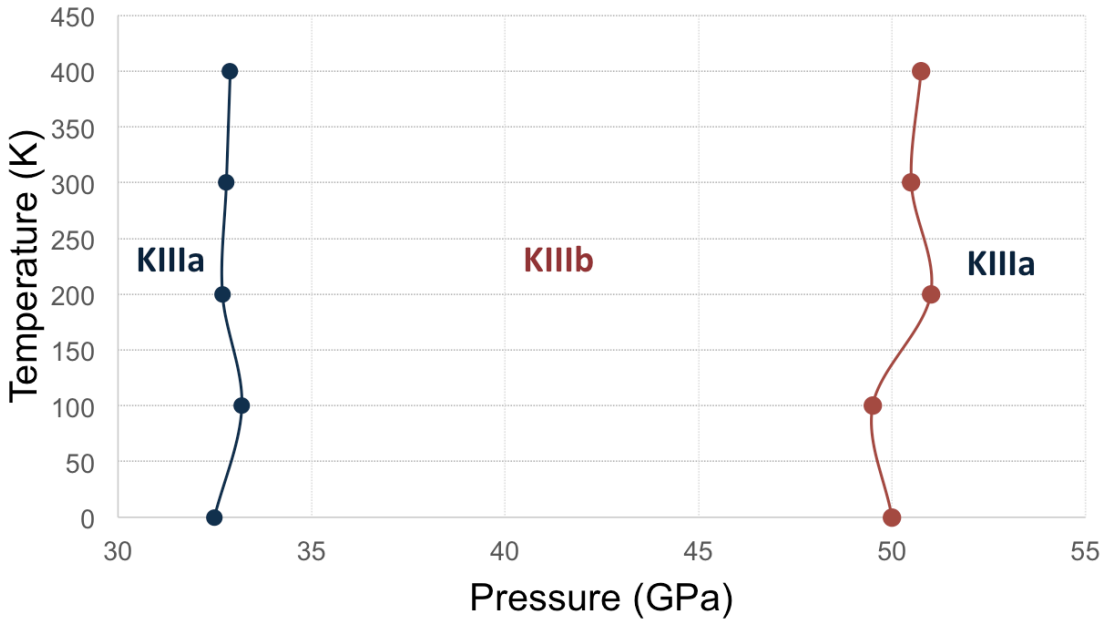

Figure 44: Phase diagram of solid potassium for pressures and temperatures ranging from 30 to 55 GPa and 0 to 450 K. The solid phases shown are KIIIa and KIIIb.

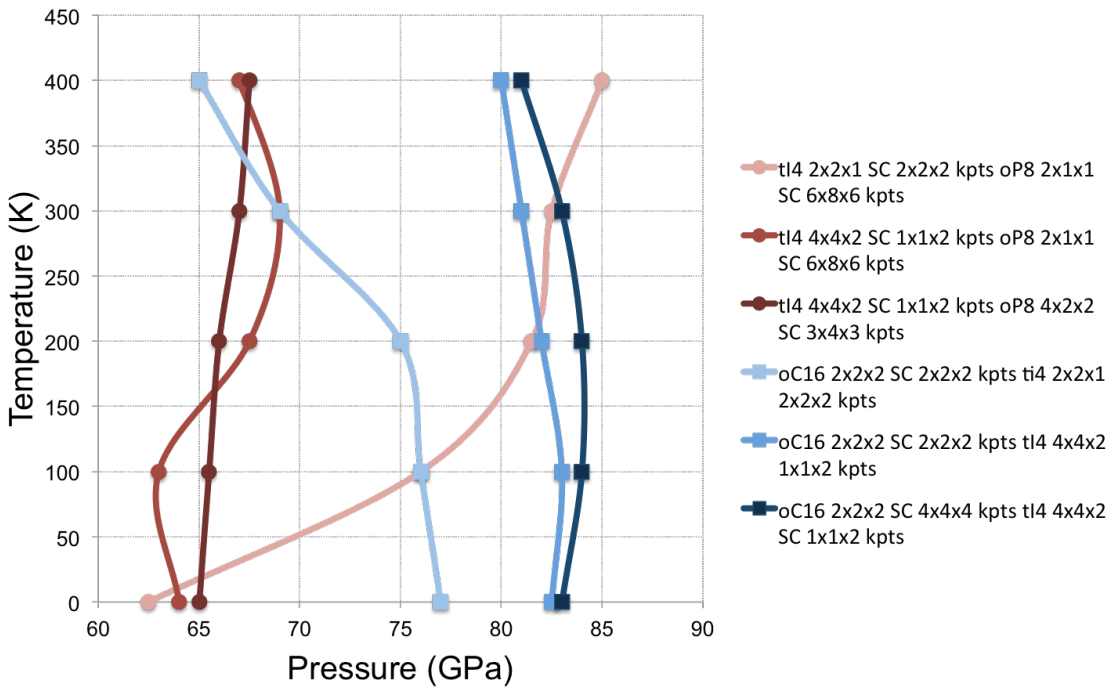

Figure 45: Phase diagram of solid potassium for pressures and temperatures ranging from 60 to 85 GPa and 0 to 450 K, respectively. The solid phases shown are the orthorombic oP8, tetragonal tI4 and orthorombic oC16

The full converged solid phase diagram is shown in Figure 46 below:

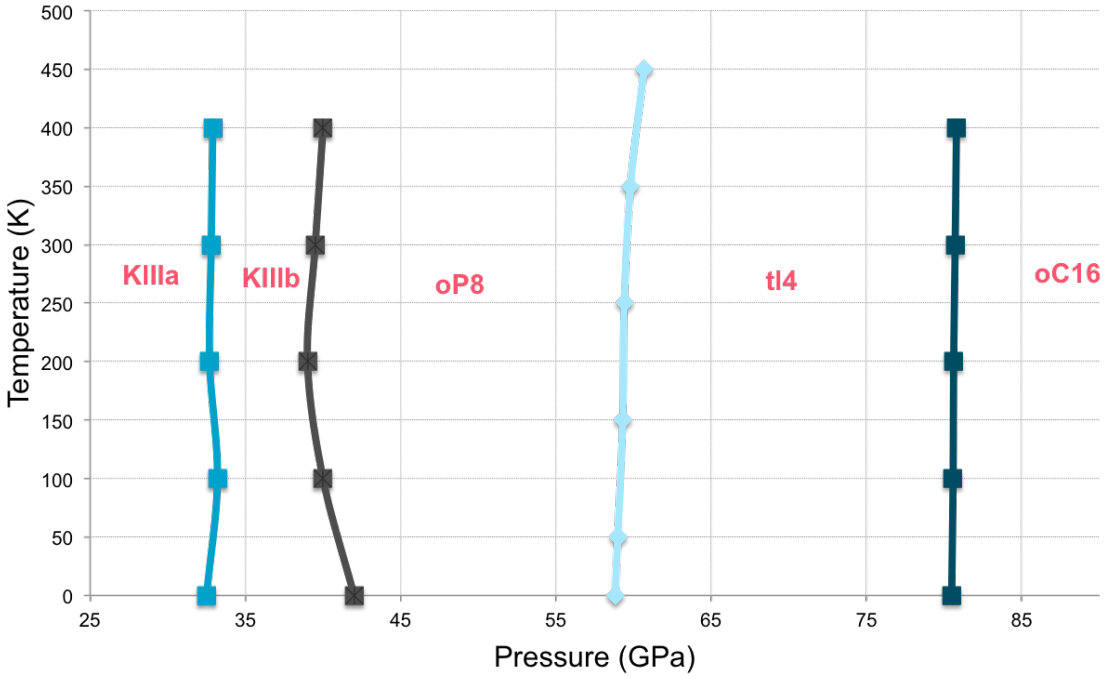

Figure 46: Phase diagram of solid potassium for pressures and temperatures ranging from 25 to 85 GPa and 0 to 450 K, respectively. The solid phases shown are KIIIa, KIIIb, oP8, tI4 and oC16

4.4 Conclusion

This chapter used the quasi-harmonic approximation to study the phase transitions at finite temperature. Previous work had been carried out on bcc and fcc, however, no work was previously done on the other solid phases of potassium. The phonon density of states were obtained for each phase and their Gibbs free energies were computed in order to observe the phase transitions at finite temperature. It is evident from the results above that the harmonic contribution to the free energies differences between neighbouring phases is negligible. The use of the quasi-harmonic approximation neglects anhar-

monicity. Anharmonicity can stabilise some structures and therefore the next chapter will determine the anharmonic contribution to the free energy of each phase using thermodynamic integration.

5 Anharmonicity

5.1 Calculations details

The anharmonic contribution to the free energy for each phase was calculated using thermodynamic integration as described in Part 2.6. To recall, the free energy can be expressed as:

$$F = E_0 + F_{harm} + F_{anharm}(\text{low}) + [F_{anharm}(\text{high}) - F_{anharm}(\text{low})] \quad (70)$$

$F_{anharm}(\text{low})$ was calculated using thermodynamic integration that is:

$$F_{anharm}(\text{low}) = \int_0^1 d\lambda < U_{low} - (U_{harm} + E_{low}) >_\lambda \quad (71)$$

Where U_{low} corresponds to the energy of the system with low convergence parameters (which will be specified later for each phase), U_{harm} is the energy of the harmonic system, E_{low} is the static energy with low convergence parameters and $< ... >_\lambda$ represents the thermal average in the ensemble generated by $U_\lambda = \lambda U_{\text{low}} + (1-\lambda)U_{\text{harm}}$.

The difference $[F_{anharm}(\text{high}) - F_{anharm}(\text{low})]$ was then calculated using the perturbative approach to thermodynamic integration, which can be expressed as:

$$[F_{anharm}(\text{high}) - F_{anharm}(\text{low})] = < U - U_{low} >_{low} - \frac{1}{2k_BT} < [U - U_{low} - < U - U_{low} >_{low}]^2 >_{\text{low}} \quad (72)$$

In practice, the right hand side of Equation 71 was calculated using ther-

modynamic integration with the constant switching of parameter λ. Each calculation yielded the difference $U_{harm} - U_{low}$ for different λ and specific volume and temperature. Once the calculation had equilibrated, the average of these differences was obtained before adding E_{low}. After this was done for each λ at one volume V, the integral was calculated using the trapezium rule:

$$\int_{x_0}^{x_n} f(x)dx = \frac{1}{2}h[(y_0 + y_n) + 2(y_1 + y_2 + ... + y_{n-1})] \tag{73}$$

Where $h = \frac{(x_n - x_0)}{n}$ and n is the number of intervals.

To calculate the right hand side of Equation 72, firstly, a MD run with low convergence parameters was carried out after which configurations were extracted every 200 steps. On each of these configurations, static calculations were carried out with both high and low convergence parameters.

Finally, the errors of the calculations were calculated using the blocking method [116],[99]. As MD calculations produce quantities which fluctuate over time, the quantity of interest is the average m over time steps. Therefore in order to calculate the errors of these correlated quantities one must obtain the variance of the mean $\sigma^2(m)$:

$$\sigma^2(m) = < m^2 > - < m >^2 \tag{74}$$

The blocking method involves splitting the dataset into N blocks after the system was equilibrated. If all blocks were uncorrelated, the variance of the mean of the system could be calculated directly using the classic equations of statistics, however, blocks in an MD simulation are correlated. The average of this new dataset x_i must be equal to x thus both the average and $\sigma^2(m)$ are invariant under the blocking transformation. The average of each block is

then computed and the standard deviation of the mean of each block can be written as:

$$\sigma_b = \sqrt{\frac{1}{N-1}\sum_{i=1}^{N}(< X_i^2 > - < X >_N^2)} \tag{75}$$

Where X_i is the average of block i, $< X >_N$ is the average over all blocks and N is the number of blocks. As the length of the blocks increases, the standard deviation of each block will increase until a limiting value is reached. The latter can be read of a plot as shown in Figure 47 where the error estimate converges as the block size increases.

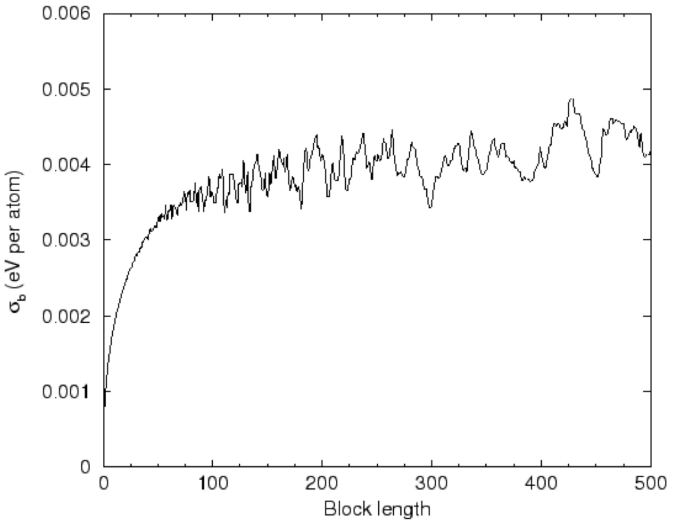

Figure 47: Standard deviation of each block as a function of block length.

An additional information can be obtained from this method which is the uncertainty in σ as it is dependent on the number of block averages.

5.2 Convergence with respect to λ

In order to determine how many λ were necessary for the constant switching thermodynamic integration, calculations were carried out on bcc. The MD calculations were carried out using the Andersen thermostat, the planewave cutoff was set to 400 eV, MP smearing was used with a smearing parameter of 0.2 and only 7 valence electrons were used. A supercell of 64 atoms was used with V=30 Å^3 per atom.The same parameters were used to determine E_{low} which was found to be 0.207 eV per atom. In order to test the convergence, nine different values of λ were used to obtain DF $=< U_{low} - U_{harm} - E_{low} >$ and Figure 48 shows these results for 100 K (at which the anharmonic contribution is expected to be small).

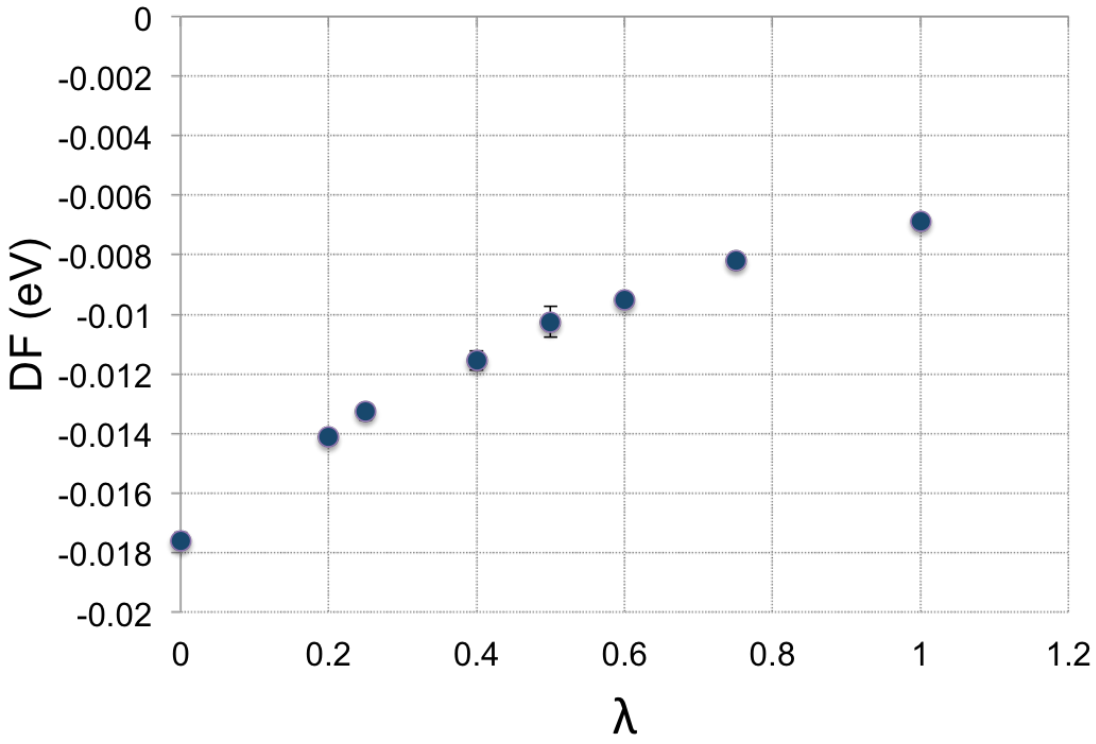

Figure 48: DF=$< U_{\text{low}} - U_{\text{harm}} - E_{\text{low}} >$ as a function of λ for bcc at 100 K. Most error bars are not visible as they are smaller than the markers.

Convergence tests showed that 3 λ points, equally spaced, were enough to ensure energy differences converged to better than 3 meV as can be seen in Table 9. In this case the 3 λ points chosen for future calculations were $\lambda = 0, 0.5, 1$.

Table 9: Convergence test with respect to the number of λ. The free energy differences are in eV. The errors (σ) were calculated using the blocking method

Number of lambdas	$< U_{low} - U_{harm} >$	σ
3	-0.011251714	-0.011251714
5	-0.010992993	9.44462E-05
6	-0.011131060	9.09092E-05

5.3 Calculation results for bcc

Thermodynamic integration calculations were performed to obtain $F_{\text{anharm}}(\text{low})$ for bcc for V=30-60 Å^3 per atom and temperatures spanning from 100 to 400 K (above which melting occurs according to experiments). This first part was determined using a 64-atom supercell with low convergence parameters: the planewave cutoff was 116 eV, Methfessel-Paxton smearing was used with $\sigma = 0.2eV$, only 7 valence electrons were included and finally, only the Gamma point was used. Figure 49 shows DF obtained for the different volumes and temperatures.

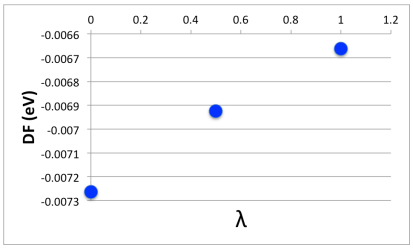

(a) V=50 Å^3 - 100 K

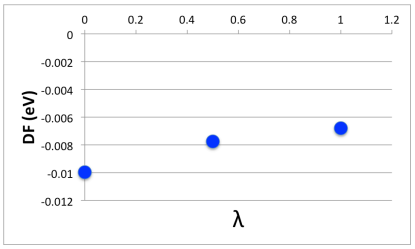

(b) V=50 Å^3 - 200 K

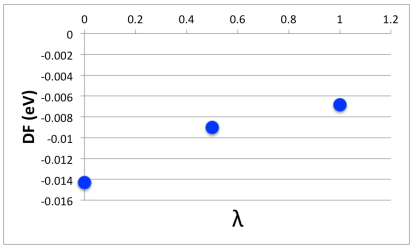

(c) V=50 Å^3 - 300 K

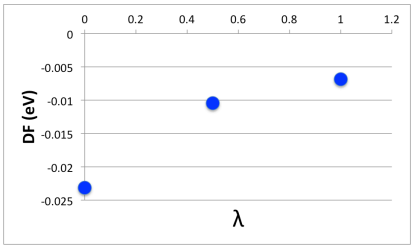

(d) V=50 Å^3 - 400 K

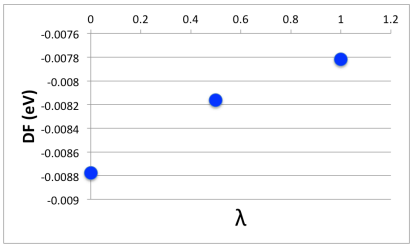

(e) V=60 Å^3 - 100 K

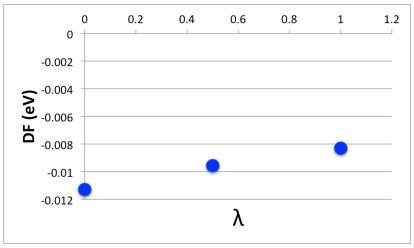

(f) V=60 Å^3 - 200 K

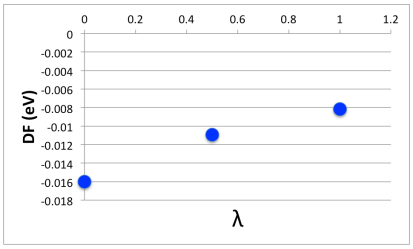

(g) V=60 Å^3 - 300 K

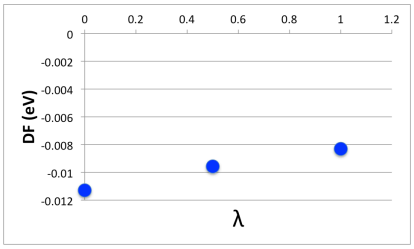

(h) V=60 Å^3 - 400 K

Figure 49: DF with respect to λ for bcc for volumes 50-60 Å^3 per atom and temperatures ranging from 100K to 400K

To obtain the difference $F_{anharm}(\text{high}) - F_{anharm}(\text{low})$, the perturbative ap-

proach was employed:

$$F \simeq E_{\text{low}} + < \Delta U >_{\text{low}} + \frac{1}{2k_B T} < (\delta \Delta U)^2 >_{\text{low}} \tag{76}$$

Where $\delta \Delta U = U_1 - U_{\text{low}} - < U_1 - U_{\text{low}} >_{\text{low}}$. In practice, a MD run was performed with low convergence parameters at different temperatures. For each temperature, 25 statistically independent configurations were extracted. One static run with low convergence parameters was performed on each of these configurations and one static run with high convergence parameters. These high convergence parameters for bcc are a planewave cutoff of 400 eV, 9 valence electrons, Fermi smearing with $\sigma = 0.05$ and a Gamma centered k-point grid of 4x4x4 was used. Once the difference $F_{anharm}(\text{high}) - F_{anharm}(\text{low})$ was obtained, F_{anharm} was determined as follows:

$$F_{\text{anharm}} = \int_0^1 DF + < \Delta U >_{\text{low}} + \frac{1}{2k_B T} < (\delta \Delta U)^2 >_{\text{low}} + E_{\text{low}} - E_0 \tag{77}$$

$$F_{\text{anharm}} = DF_1 + < \Delta U >_{\text{low}} + \text{Term}_2 + E_{\text{low}} - E_0 \tag{78}$$

The results of the perturbative approach for bcc along with the resulting F_{anharm} are shown in Table 10.

Table 10: Anharmonic contributions to the free energy of bcc for various volumes and temperatures where $DF_1 = \int_0^1 DF$, Term$_2$ $= \frac{1}{2k_BT} < (\delta\Delta U)^2 >_{\text{low}}$ and $DF_2 =< \Delta U >_{\text{low}} +$Term$_2$.Unless specified otherwise, units are in eV

Volume (Å^3 /atom)	Temperature (K)	DF$_1$ (eV)	$< \Delta U >_{\text{low}}$	Term$_2$	DF$_2$	E$_{\text{low}}$	E$_0$	**F$_{\text{anharm}}$**
30	100	-0.018	-0.118	-1.2E-4	-0.118	0.207	0.077	1.12E-3
40	100	-0.012	-0.1455	-4.76E-5	-0.1456	-0.453	-0.602	-7E-3
	200	-0.006	-0.1455	4.76E-5	-0.146	-0.453	-0.602	-2.54E-3
50	100		-0.14	-4.76E-5	-0.15	-0.7671	-0.89	
	200	-0.0083	-0.1226	6.67E-7	-0.123	-0.7671	-0.89	-7.89E-3
	300	-0.0098	-0.1209	3.26E-5	-0.121	-0.7671	-0.89	-7.6E-3
	400	-0.0127	-0.1198	4.43E-5	-0.12	-0.7671	-0.89	-9.52E-3
60	100	-0.0082	-0.108	-1.73E-6	-0.108	-0.8988	-1.0076	-7E-3
	200	-0.0097	-0.1068	6.46E-6	-0.107	-0.8988	-1.0076	-7.68E-3
	300	-0.0115	-0.1059	9.76E-6	-0.106	-0.8988	-1.0076	-8.65E-3
	400	-0.0097	-0.105	2.15E-5	-0.105	-0.8988	-1.0076	-5.92E-3
70	100	-0.0087	-0.098	-2.49E-6	-0.944	-1.045	-6.12E-3	
80	100	-0.0075	-0.09	-3E-4	-0.09	-0.95	-1.04	-6E-3

Results show that for all pressures and temperatures the anharmonic contribution to the free energy is only of a few meV and hence was not included in the free energy calculations.

5.4 Calculation results for fcc

The same method was applied to fcc with the same low and high convergence parameters as bcc. A 4x4x4 supercell was also built yielding a cell with 64 atoms. Figure 50 shows DF for fcc with volumes spanning from 40 Å^3 to 80 Å^3 per atom and temperatures ranging from 100 to 400 K.

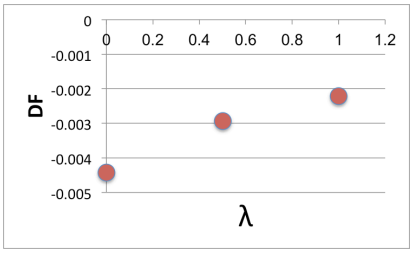

(a) V=40 Å- 200 K

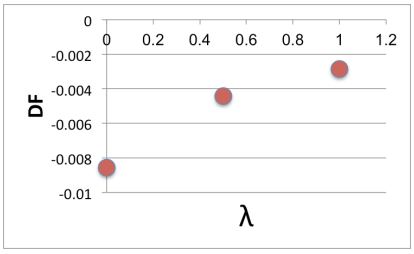

(b) V=40 Å- 300 K

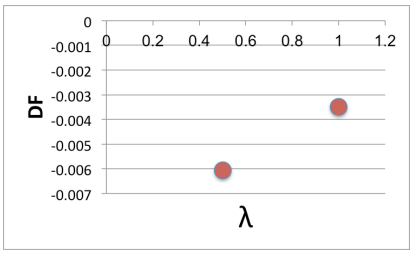

(c) V=40 Å- 400 K

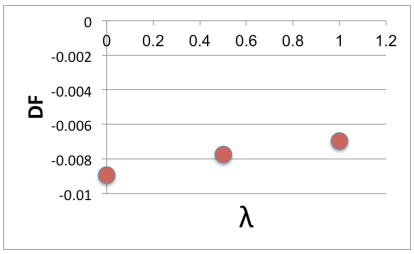

(d) V=50 Å- 200 K

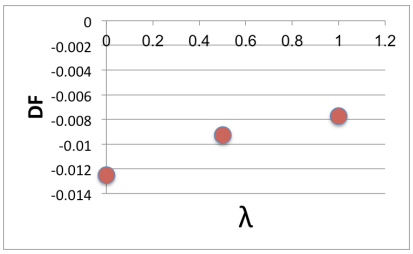

(e) V=50 Å- 300 K

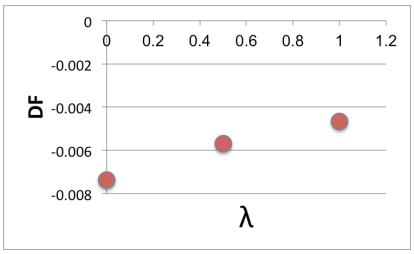

(f) V=70 Å- 200 K

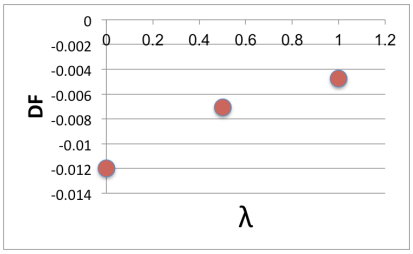

(g) V=70 Å- 300 K

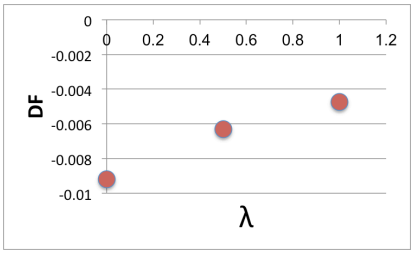

(h) V=80 Å- 200 K

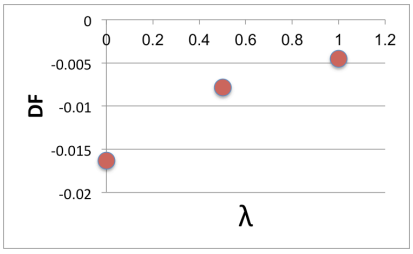

(i) V=80 Å- 300 K

Figure 50: DF with respect to λ for fcc for volumes 40-80 $Å^3$ per atom and temperatures ranging from 100K to 400K

Table 11 shows the results for the pertubative approach and the resulting F_{anharm} for fcc. Similarly to bcc, the anharmonic contributions to the free energy are negligible.

Table 11: Anharmonic contributions to the free energy of fcc for various volumes and temperatures where $DF_1 = \int_0^1 DF$, Term$_2$ $= \frac{1}{2k_BT} < (\delta\Delta U)^2 >_{\text{low}}$ and $DF_2 =< \Delta U >_{\text{low}} +$Term$_2$.Unless specified otherwise, units are in eV

Volume (Å^3 /atom)	Temperature (K)	DF$_1$ (eV)	$< \Delta U >_{\text{low}}$	Term$_2$	DF$_2$	E$_{\text{low}}$	E$_0$	**F$_{\text{anharm}}$**
30	100	0.0022			-0.117	0.187	0.07	2.2E-3
40	100	-0.0019	-0.1202	-1.72E-6	-0.1202	-0.481	-0.6015	-1.6E-3
	200	-0.0031	-0.12	10E-5	-0.11	-0.48	-0.6	-2.43E-3
	300	-0.0051	-0.118	0.0037	-0.1142	-0.48	-0.6	0.7E-3
	400	-0.0024	-0.1139	0.0017	-0.1122	-0.48	-0.6	5.4E-3
50	100	-0.0062	-0.113	-4.98E-6	-0.113	-0.774	-0.889	-4.7E-3
	200	-0.0078	-0.1116	1.15E-5	-0.111	-0.774	-0.8891	- 4.2E-3
	300	-0.0097	-0.1104	1.63E-5	-0.1104	-0.774	-0.8891	-4.9E-3
	400	-0.011	-0.1092	1.91E-5	-0.1091	-0.774	-0.8891	5.5E-3
60	100	-0.0064	-0.106	-1.23E-6	-0.106	-0.899	-1.01	-4.2E-3
70	100	-0.0047	-0.095	-3.6E-6	-0.095	-0.9499	-1.04	-4.12E-3
	200	-0.0059	-0.094	6.2E-6	-0.0942	-0.9499	-1.04	4.6E-3
	300	-0.0077	-0.096	0.02	-0.077	-0.9499	-1.04	10E-3
	400	-0.0033	-0.092	4E-5	-0.092	-0.9499	-1.04	6.2E-3
80	100	-0.005	-0.089	-1.98E-5	-0.089	-0.9525	-1.04	-3.6E-3
	200	-0.0066	-0.088	3.6E-5		-0.9525	-1.04	- 3.5E-3
	300	-0.0091	- 0.086	4.8E-5		-0.9525	-1.04	-4.5E-3
	400	-0.0034	- 0.084	1.3E-4		-0.9525	-1.04	3.8E-3

5.5 Calculation results for oP8

Anharmonic contribution to the free energy was also calculated for oP8. The 'low convergence' parameters runs were carried out using 7 valence electrons

and the Methfessel-Paxton smearing method with a default value of $\sigma = 0.2$ eV. Furthermore, as for bcc, only the Gamma point was used during the calculations along with a plane wave cutoff of 116 eV. As for the 'high convergence' parameters run, all calculations were carried out using a planewave cutoff of 400 eV with Fermi smearing ($\sigma = 0.05$ eV) and 9 valence electrons. The Gamma-centered k-points used for oP8 was 3x4x3

Results of the calculations of $DF =< U_{\text{low}} - U_{\text{harm}} - E_{\text{low}} >$ with low convergence parameters for oP8 are shown below in Figure 51.

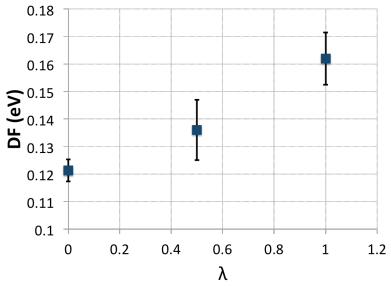

(a) 15 Å^3 - 100 K

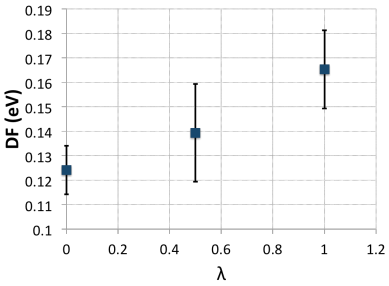

(b) 15 Å^3 - 200 K

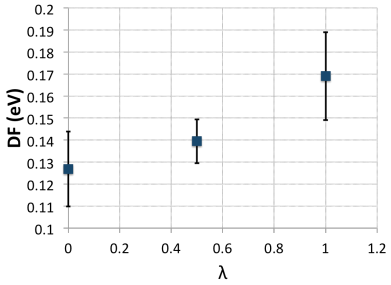

(c) 15 Å^3 - 300 K

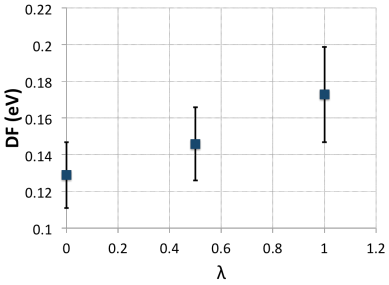

(d) 15 Å^3 - 400 K

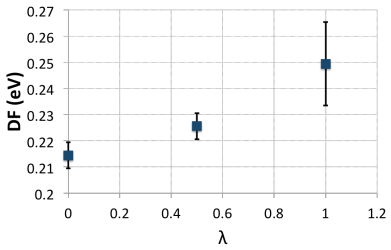

(e) 16 Å^3 - 100 K

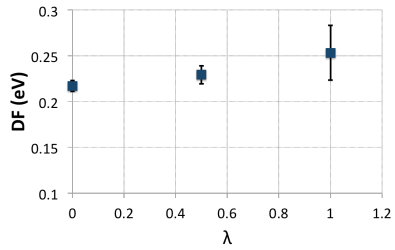

(f) 16 Å^3 - 200 K

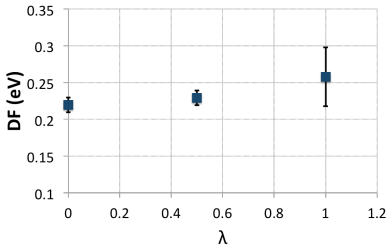

(g) 16 Å^3 - 300 K

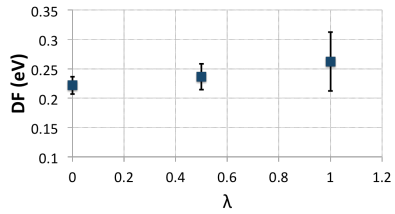

(h) 16 Å^3 - 400 K

Figure 51: DF with respect to λ for oP8 from 100 K to 400 K

Table 12 shows the complete results for thermodynamic integration for oP8 from which it can be seen once more the anharmonic contribution to the free energy is negligible as it only accounts for a few meV. Given the negligible results of the anharmonic contributions for bcc, fcc and oP8, it can be assumed that the contributions will be negligible for all phases.

Table 12: Anharmonic contributions to the free energy of oP8 for various volumes and temperatures where $DF_1 = \int_0^1 DF$, Term$_2$ $= \frac{1}{2k_BT} < (\delta\Delta U)^2 >_{\text{low}}$ and $DF_2 =< \Delta U >_{\text{low}} +$Term$_2$.Unless specified otherwise, units are in eV.

Volume (Å^3 /atom)	Temperature (K)	DF$_1$ (eV)	$< \Delta U >_{\text{low}}$	Term$_2$	DF$_2$	E$_{\text{low}}$	E$_0$	**F$_{\text{anharm}}$**
15	100	0.13886	-0.338	-4.8E-5		2.92	2.71	6.96E-3
	200	0.142	-0.3384	-9.4E-5		2.92	2.71	8.45E-3
	300	0.144	-0.34	-1.3E-4		2.92	2.71	8.27E-3
	400	0.148	-0.342	-1.8E-4		2.92	2.71	11E-3
16	100	0.229	-0.268	-4.62E-5		-4.079	4.113	-4.17E-3
	200	0.232	-0.27	-8.93E-5		-4.079	4.113	-2.61E-3

This chapter determined the anharmonic contribution to the free energy of each phase using thermodynamic integration. The reference system chosen was the harmonic potential and the results show that the anharmonic contributions are in the order of meV, therefore it is not necessary to include this contribution moving forward. The next chapter will look at melting. This will be done using 3 methods: the direct coexistence method, the coexistence method with a potential and the Z method. Previous work done on melting was carried out until 700 K and 25 GPa.

6 Melting

6.1 Coexistence with a potential

6.1.1 Introduction

As mentioned in part 2.7.2, the coexistence method was used with a potential. Initially, the EAM was used as a reference model for bcc in order to test the method. The fits can be done on the solid, the liquid or both. The fit is done using the least squares method. The fitted energies, the actual energies and the difference between the two were plotted. Both a visual inspection of the energies and the value of χ^2 were necessary to evaluate the goodness of the fits. Once the fit completed, a supercell was built, and after thermalization, the aim was to obtain a cell half liquid and half solid to determine the melting temperature. The results for bcc are shown in Section 6.1.2 and the inconclusive results for the other phases are shown in Section 6.1.3.

6.1.2 Results for bcc

The reference model EAM was fitted to both the liquid and the solid for bcc. First, a fit was performed on the liquid at 400K as shown in Figure 52 and second, on the solid as shown in Figure 53.

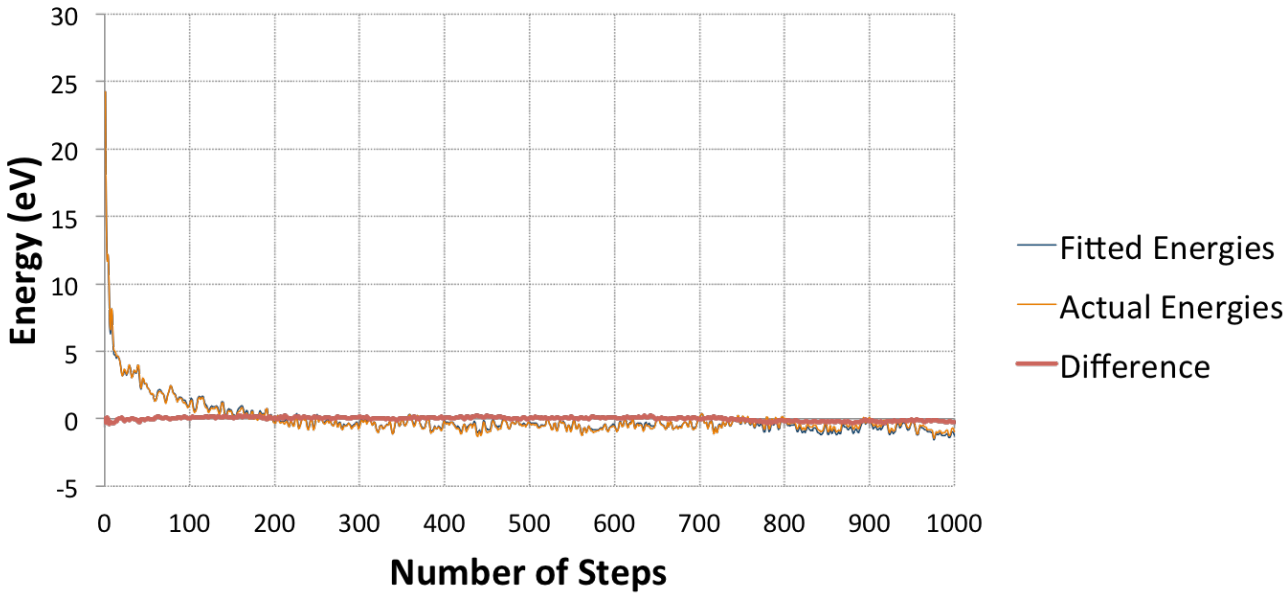

Figure 52: Fit of EAM with liquid K

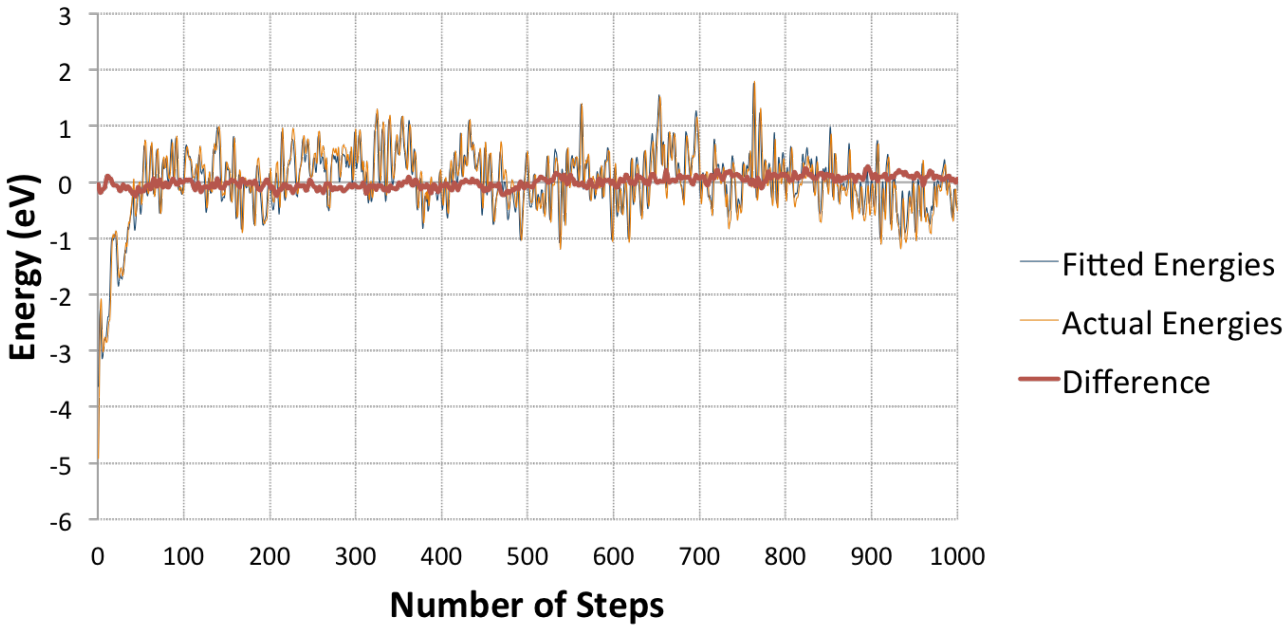

Figure 53: Fit of EAM with solid bcc K

Finally, the solid and the liquid were fitted together as shown in Figure 54 which shows that the fit is particularly good as it described the *ab initio* potential even in the equilibration part of the simulation, which is sampling a phase space not relevant to the chosen thermodynamic conditions. The parameters of each fit are shown in Table 20.

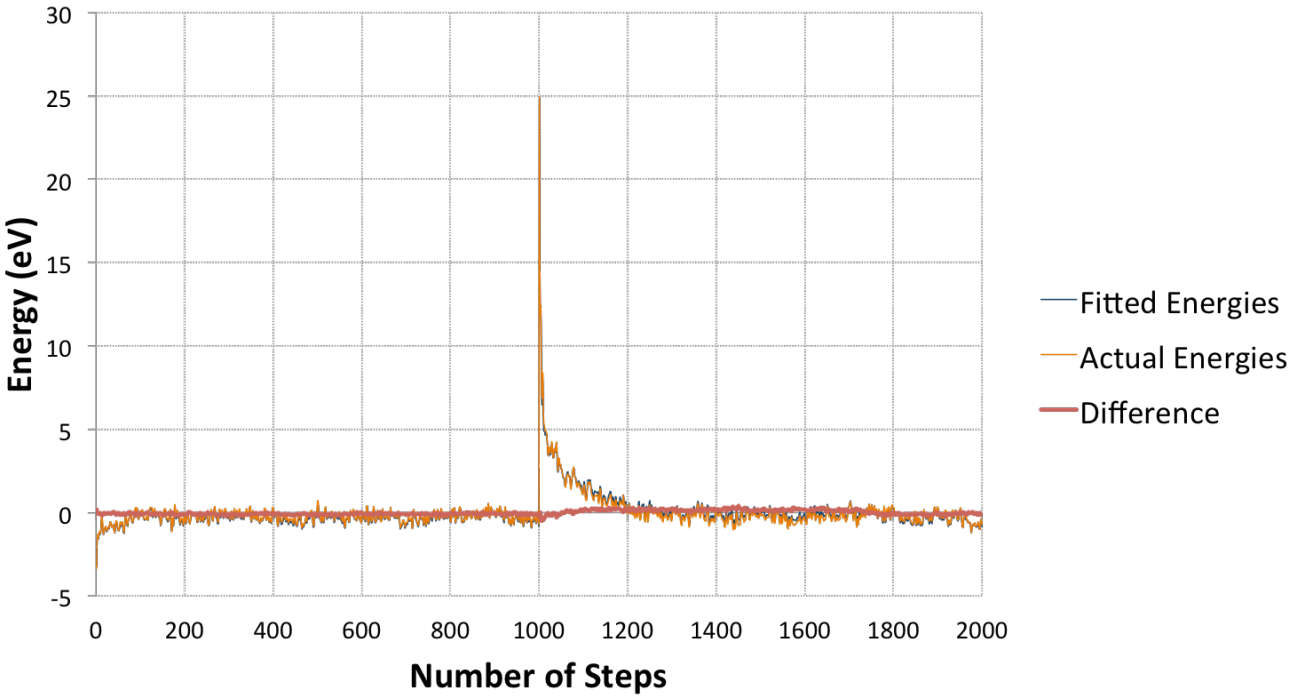

Figure 54: Fit of EAM with both solid and liquid

Table 13: Parameters of the fit for bcc with the EAM

State	ε(eV)	a(Å)	n	m	C	χ^2
Liquid	0.74	3.803	3.688943	2.34	2.72	0.277E-3
Solid	1.10	3.35	3.62	2.16	1.66	0.25E-4
Solid and Liquid	1.03	3.39	3.64	2.21	1.85	0.27E-3

After the fit, a supercell of 2000 atoms was constructed from the solid static

relaxed configuration of bcc. The first step was to thermalize the supercell at 300 K so that the whole supercell remains solid as is shown in Figure 55.

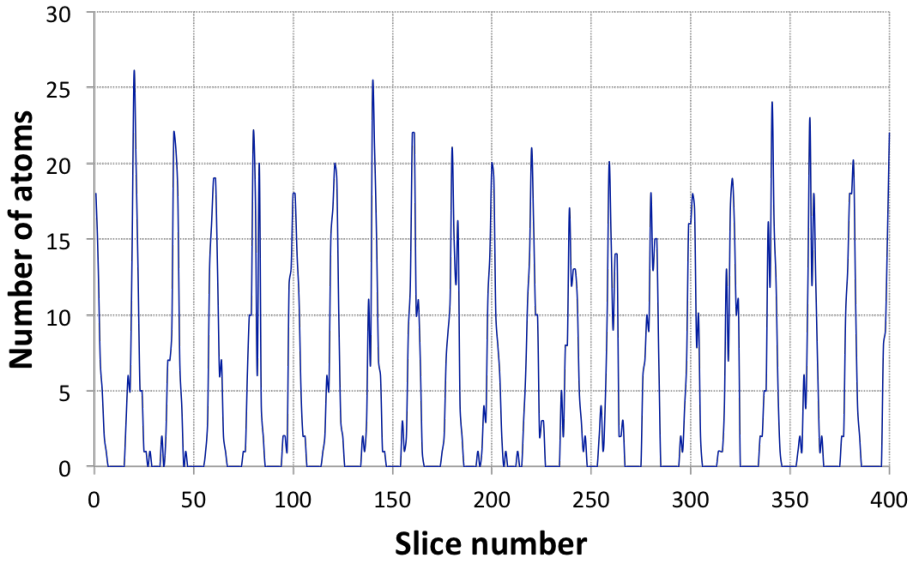

Figure 55: Number density of solid bcc K at T=300 K.

The second step consisted in freezing half the atoms and set the temperature at 3000K in order to melt half the cell. As shown in Figure 56, the cell then becomes half solid and half liquid.

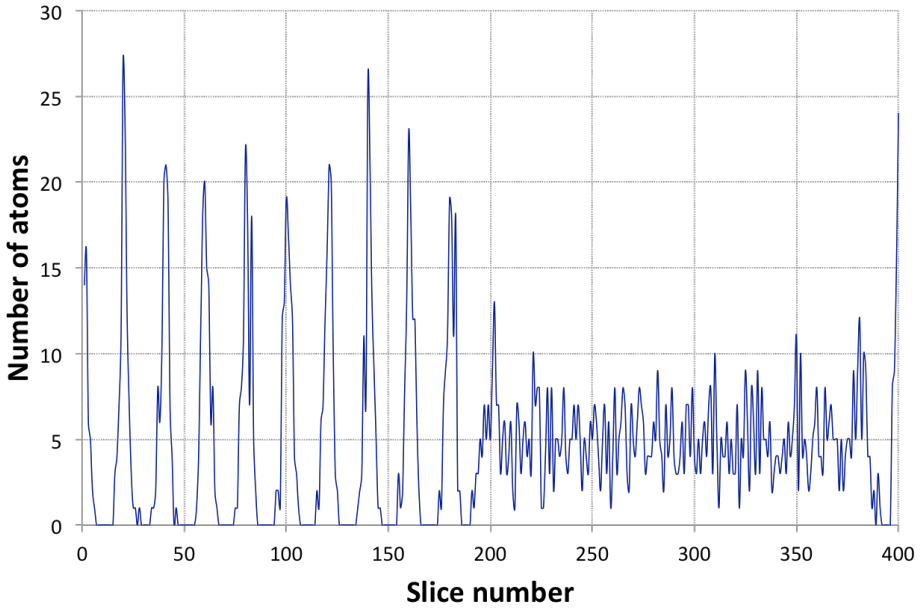

Figure 56: Number density of half frozen solid bcc K and half liquid K at T=3000 K.

The third step consisted in rethermalizing the cell close to melting temperature all the whilst taking care that it did not freeze or melt entirely. To do so the temperature was set to 600K and Figure 57 shows both liquid and solid coexist.

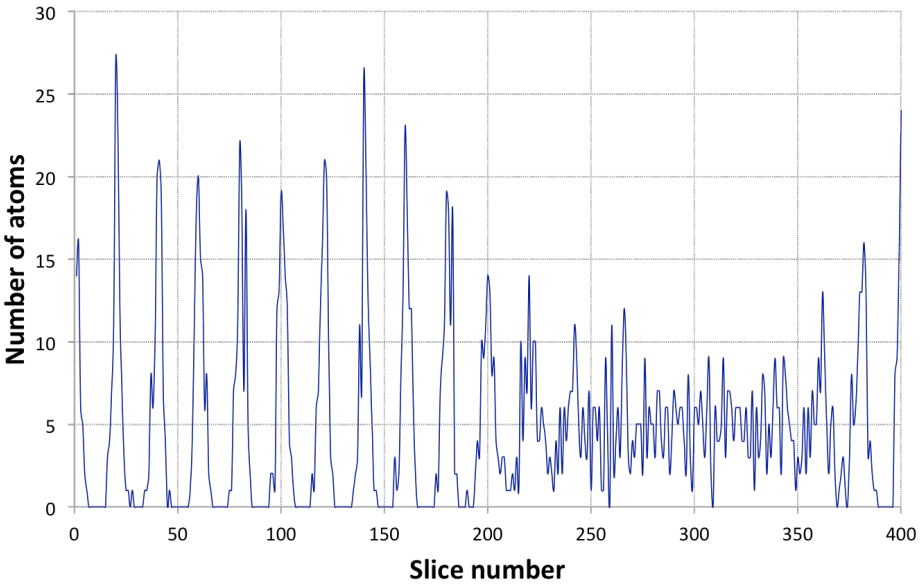

Figure 57: Number density of half solid bcc K and half liquid K at T=600 K.

The final step consisted of trial and error in order to maintain both the liquid and solid and run long enough simulations for both states to coexist (typically over 100 ps). A range of temperatures from 400K to 600K were tried to finally yield a melting temperature of 477K at 2GPa as shown in Figure 58.

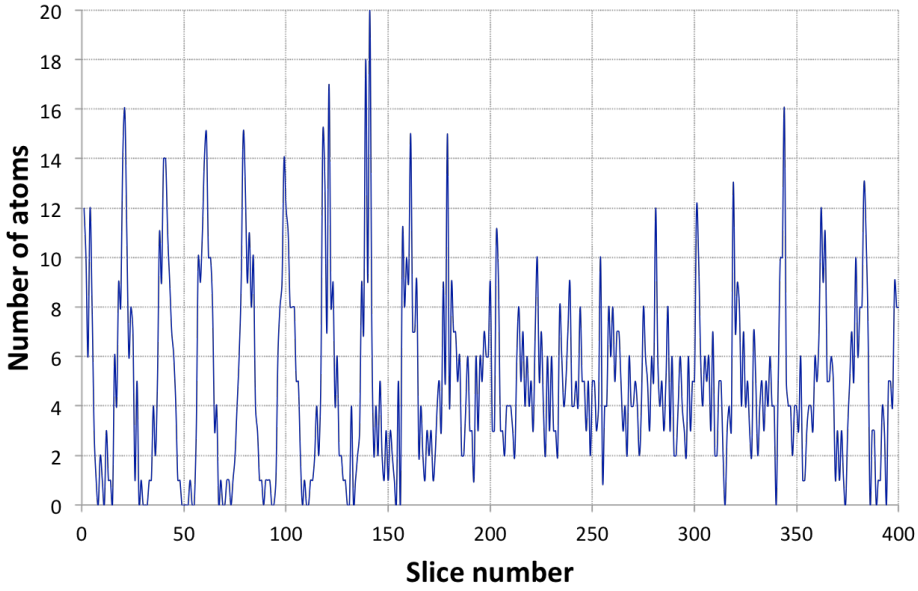

Figure 58: Number density of half solid bcc K and half liquid K at T=477 K.

This melting temperature is in very good agreement with previous experimental results - Zha and Boehler [117] found the melting temperature at 2 GPa to be 450 K as shown in Figure 22. The results from previous calculations are in excellent agreement as two previous studies [9, 17] found T_m=480 K as seen in Figure 20 and 22.

6.1.3 Inconclusive results for other phases

For the fcc phase, the same procedure as described above was used. Indeed, an AIMD run on the relaxed supercell of fcc was performed using low convergence parameters. The volume used was of 30 $Å^3$ per atom, which corresponds approximately to a pressure of about 14 GPa. At this pressure, fcc is stable and the phonon density of states shows no imaginary phonons.

Initially, the AIMD run was carried out at 300 K and the supercell remained solid. The energy profile was then fitted using the EAM model as shown in Figure 59 along with the resulting parameters in Table 14

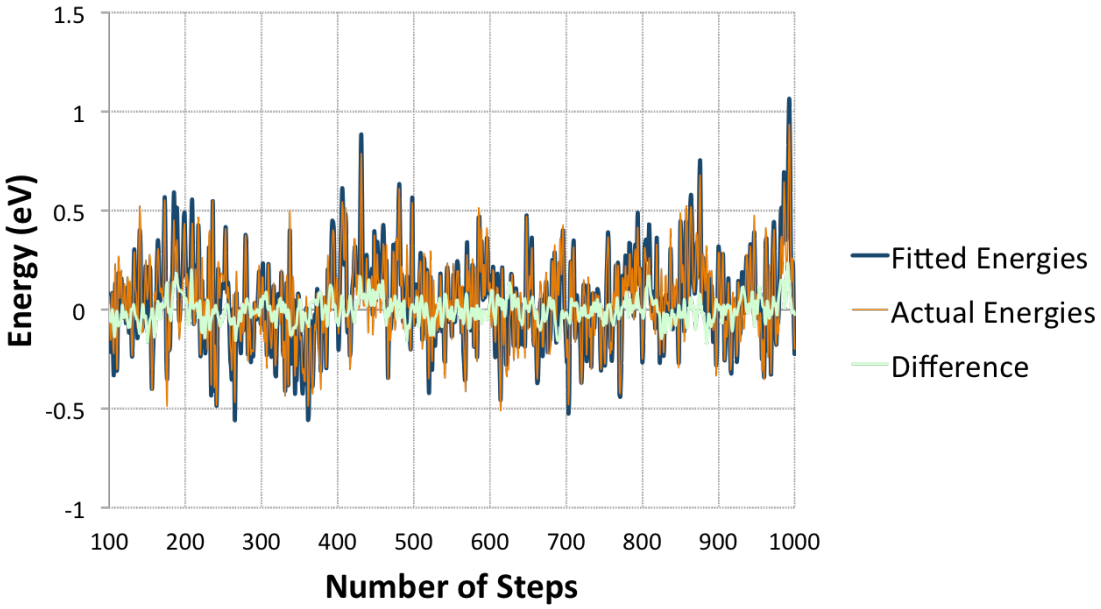

Figure 59: Fit of solid fcc at 300 K with the EAM

Table 14: Parameters of the solid fcc fit with the EAM

ϵ (eV)	1.23
a (Å)	2.87
n	3.51
m	1.41
C	1.614
χ^2	0.634E-4

As can be seen in Figure 59, the fit is not particularly good as the inter-

val difference between fitted and actual energies represents over 30% of the interval over which actual and fitted energies vary as opposed to 10% in the case of bcc.

The same procedure was applied to the other phases of K without success as the fits were considerably worse. The chosen volumes of each phase corresponded to a pressure at which the phase was stable and it was ensured no imaginary phonons were present for these volumes. For oC16, oP8 and tI4 the volumes chosen were 12 Å^3 per atom ($\sim$94 GPa), 16 Å^3 per atom ($\sim$49 GPa) and 14 Å^3 per atom ($\sim$63 GPa), respectively. The low convergence MD runs on all three phases were carried out using a planewave cutoff of 400 eV, 9 valence electrons and a smearing parameter of 0.05. For oC16, a 2x2x2 supercell was generated and calculations were performed using a 2x2x2 Gamma-centered k-points grid, For oP8, a 2x1x1 supercell was generated and calculations were performed using a 6x8x6 Gamma-centered k-points grid. Finally, for tI4, a 2x2x1 supercell was generated and calculations were performed using a 1x1x2 Gamma-centered k-points grid. Figure 60 shows the fits for each solid phase and Table 20 shows the parameters of each fit.

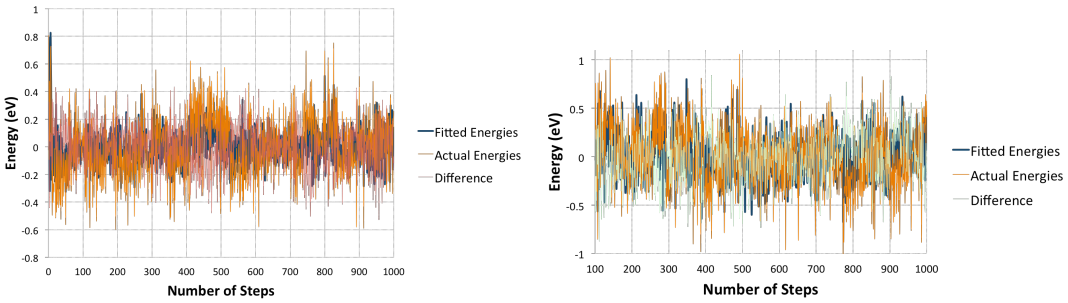

(a) oC16

(b) oP8

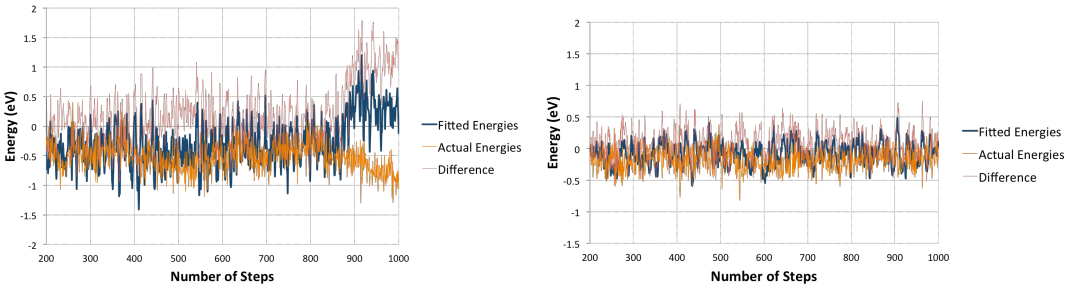

(c) tI4

(d) KIIIa

Figure 60: Fits of solid phases with the EAM

Table 15: Parameters of the fit for bcc with the EAM

Phase	ε(eV)	a(Å)	n	m	C	χ^2
oP8	2.15	2.27	4.29	1.77	1.20	0.2821E-1
tI4	5.17	2.10	2.0	2.1	-0.35	0.7026E-2
KIIIa	0.87	2.40	4.34	3.71	2.21	0.1806E-2
oC16	0.71	0.06	5.52	2.82	-1.11	0.4221E-3

In order to remediate the inadequate fits, the following was tested:

- Setting different initial values for all parameters
- Increasing the number of increments
- Fitting the liquid
- Fitting both the liquid and the solid together
- Using a different model - in this case the Stillinger-Weber was used
- Fitting the pressure as well

Nevertheless, none of these tests yielded good enough fits to use this method to determine the melting curve. This conclusion concurs with the results previously found by Belashchenko and Smirnova [51], which also find that the EAM potential could not describe well both the solid and liquid states above 5 GPa.

6.2 Direct Coexistence

As the calculations using a coexistence with a potential did not yield any results aside from the bcc phase, the direct coexistence was then employed by obtaining a large supercell (1000 atoms) of fcc and KIIIa, which was thermalized. Then, half the atoms were fixed and a very high temperature was applied (3000K) in order to melt the other half. The supercell is then rethermalized at the expected melting temperature (500K for fcc and 750K for KIIIa). The cell was then left to evolve freely for 10000 steps. Care was taken to check that the energy did not increase (decrease) which would have indicated that the cell

had melted (solidified). MP smearing was used with a smearing parameter of 0.2, a planewave cutoff of 113 eV and only the Gamma point was used with 7 valence electrons. The results shown in Figure 61 are in good agreement with previous experiments from McBride et al. [49] as shown in Figure 21, however, direct coexistence calculations require a large number of atoms and proved to be computationally too expensive. Therefore the method was not applied to other phases.

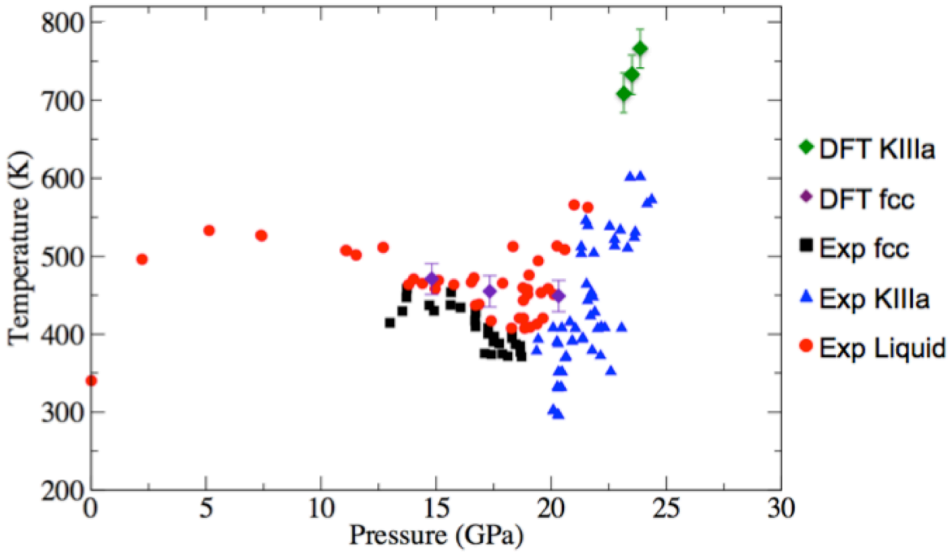

Figure 61: Temperature-pressure graph obtained with the direct coexistence where the red cirlcles represent the liquid, the blue triangles represent KIIIa and the black squares represent fcc. All three are from experimental results [49].

6.3 Z Method

6.3.1 Introduction

The Z method, which was introduced by Belonoshko et al. [107], has proven successful [118, 119, 120] in many cases to dermine melting curves. Its reliability, however, has nonetheless not yet been fully determined. Indeed, the original study [107] prescribes a large enough number of atoms and long enough simulations to achieve relevant results. Both the required simulation time and number of atoms will vary depending on the system studied. An extensive study [110] on the reliability of the Z method was carried out, which included investigating the evolution of the mean waiting time as a function of $(T_{initial} - T_{LS})$. The study reported that the Z method could only, at best, yield an upper bound to the melting temperature. The reason being, melting may not be observed should $(T_{initial} - T_{LS})$ be such that the mean waiting time be larger than the simulation time. With that in mind, the Z method was used only for the purpose of finding the upper bound of the melting temperature of Potassium. Consequently, all melting temperatures hereafter may only be considered as a starting point to use with other more reliable methods. This first step using the Z method can be useful if, as is the case for potassium, there is no previous experimental or theoretical studies of the melting temperature as other methods (e.g. coexistence) require an initial guess of the melting temperature. All Z method calculations were carried out with low convergence parameters that is, the GGA with 7 valence electrons, MP smearing with $\sigma = 0.2$ and only the Gamma point. The number of atoms will be specified when appropriate.

6.3.2 Z method for bcc and oP8

The Z method was first applied to bcc as there were previous studies on the melting of this phase [9], it could be used to assess the quality of the results yielded by the Z method. The calculations were carried out using a supercell of 216 atoms and a time step of 2 fs. A range of temperatures (1000K, 5000K, 1500K, 2500K) were tested for different simulation times as shown in Table 16.

Table 16: Temperatures and simulation times for bcc using the Z method

Initial Temperature (K)	Simulation Time (ps)
1000	50
1500	29
2500	47
5000	40

As mentioned in Part 6.3, we are expecting a drop in temperature (and increase in pressure) at a certain temperature, which would indicate the limit of superheating has been reached and the melting temperature can be readily obtained. Nevertheless, as shown in Figure 62, a first drop is observed at about half the initial temperature due to equipartition [118] but none of the runs show a second temperatures drop which could be attributed to melting which may be due to the fact that that the initial temperature is too far or too close from T_{LS} thus indicating that the simulations were not long enough.

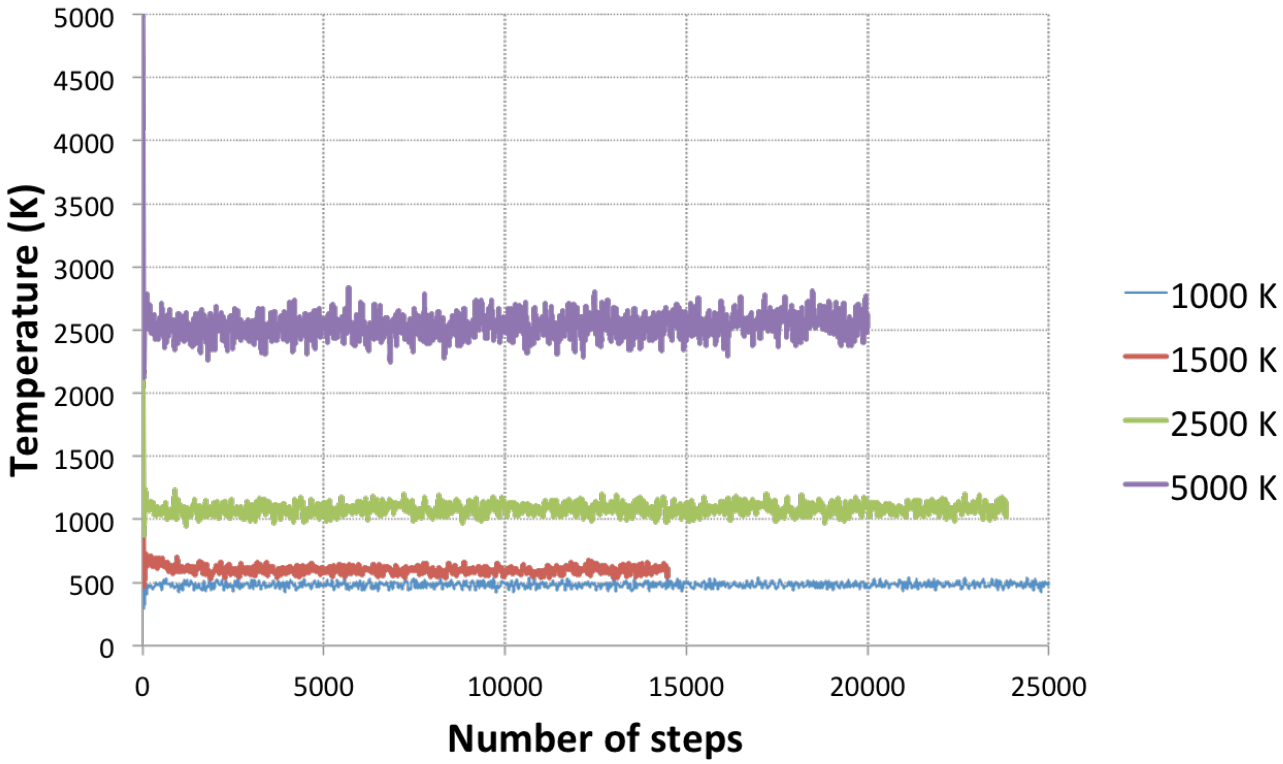

Figure 62: Temperature profiles after the Z method runs for bcc at 1000K, 1500K, 2500K and 5000K

At each temperature, both the mean squared displacement and the diffusion coefficient were used to determine whether the cell was liquid or solid and confirm melting had not occurred. The results for each temperature are shown in Figure 64.

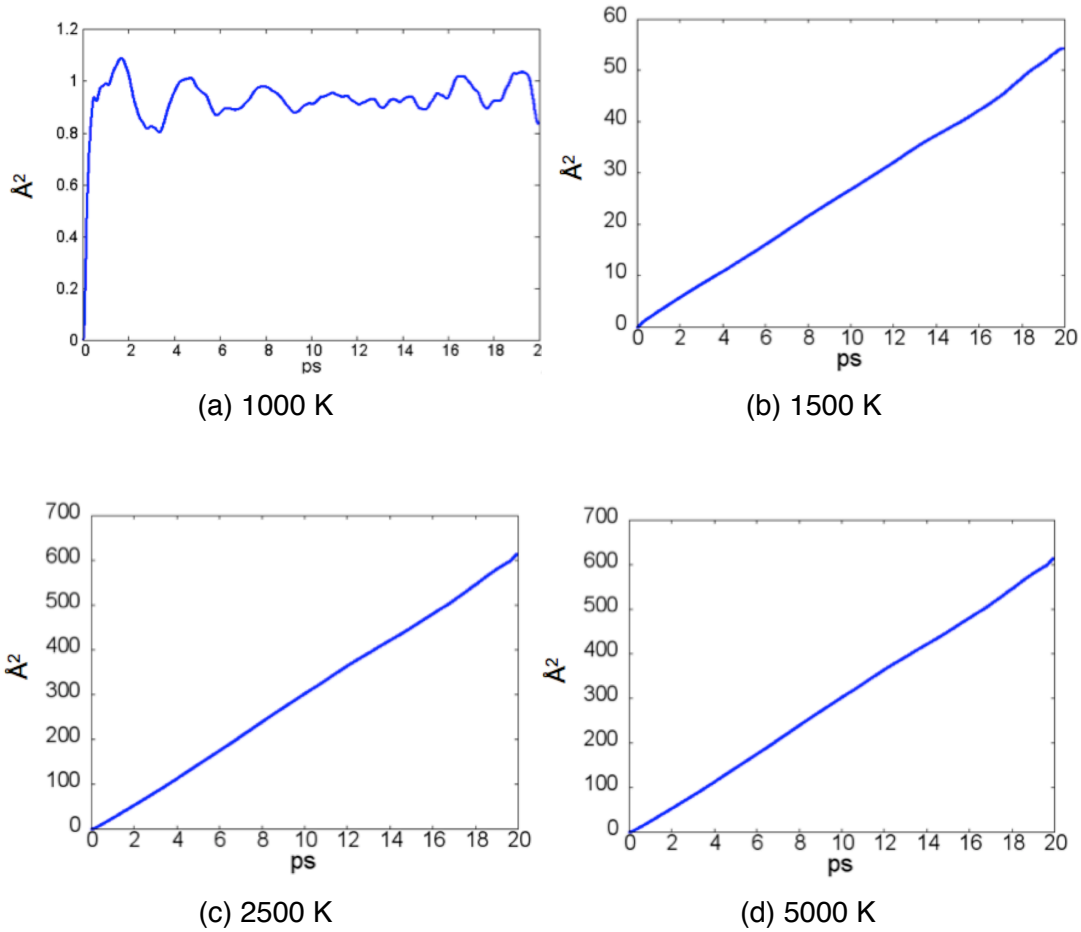

Figure 63: Mean square displacement (Å^2/ps) for bcc at 1000, 1500, 2500 and 5000 K

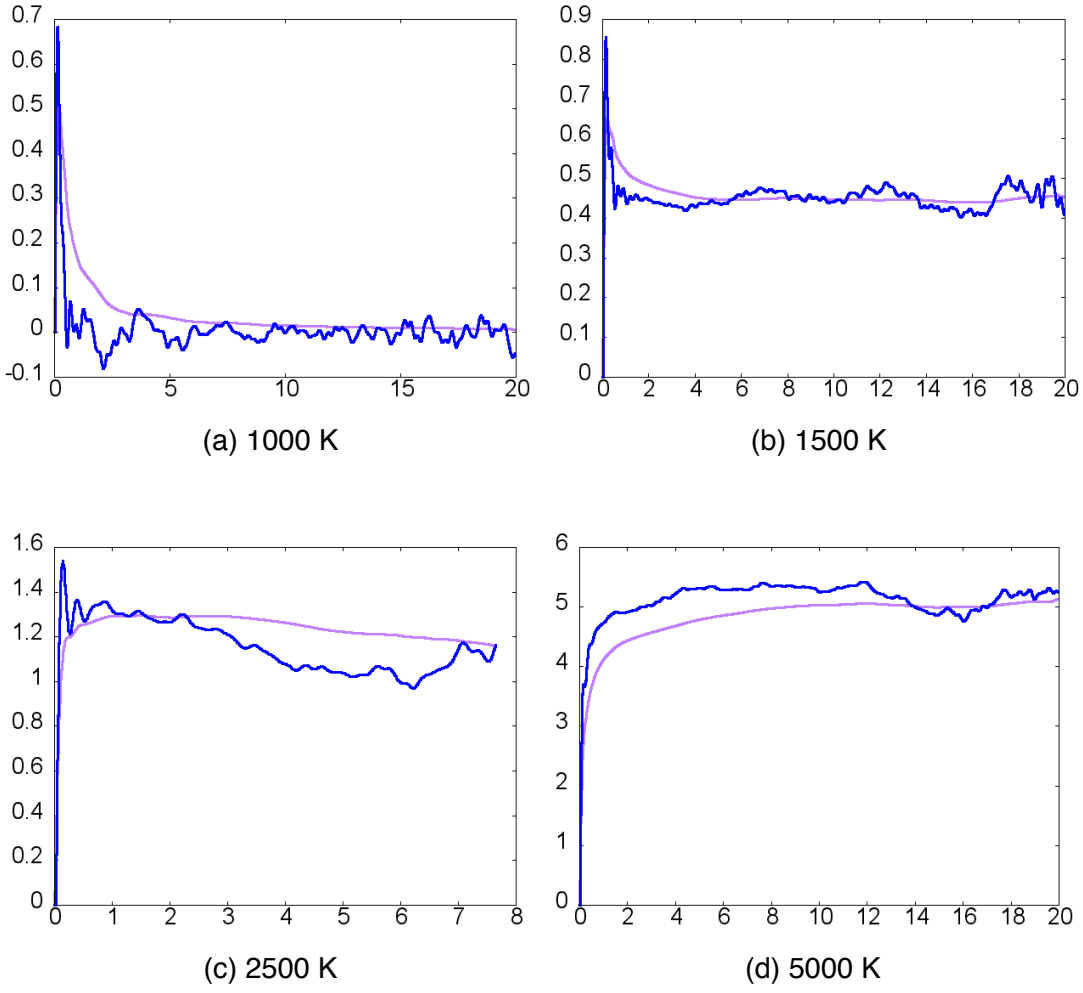

(a) 1000 K

(b) 1500 K

(c) 2500 K

(d) 5000 K

Figure 64: Diffusion coefficient for bcc at 1000, 1500, 2500 and 5000 K

Figure 64 shows that at 1000K, the cell is still solid whereas at 2500K and 5000K, it has melted. For 1500 K, the last configurations of the simulation show that the cell has melted, however, it was difficult to decide whether the beginning of the simulation was liquid or solid. This illustrates the essence of the Z method that is trial and error. As shown in Figure 65, a wide range of temperatures must be tested which will be too low, too high or inconclusive,

from which the range of temperatures can be narrowed.

Figure 65: Schematic representation of the trial and error method used for bcc

As shown in Figure 65,it was decided to run a simulation at 1300 K for 40 ps. The temperature profile at 1300 K shows a drop in temperature after 13000 steps as shown in Figure 66. Calculating both the mean square displacement and the diffusion coefficients showed that during the first 13000 steps, the cell is still solid whereas it becomes liquid after the drop, hence melting occurs.

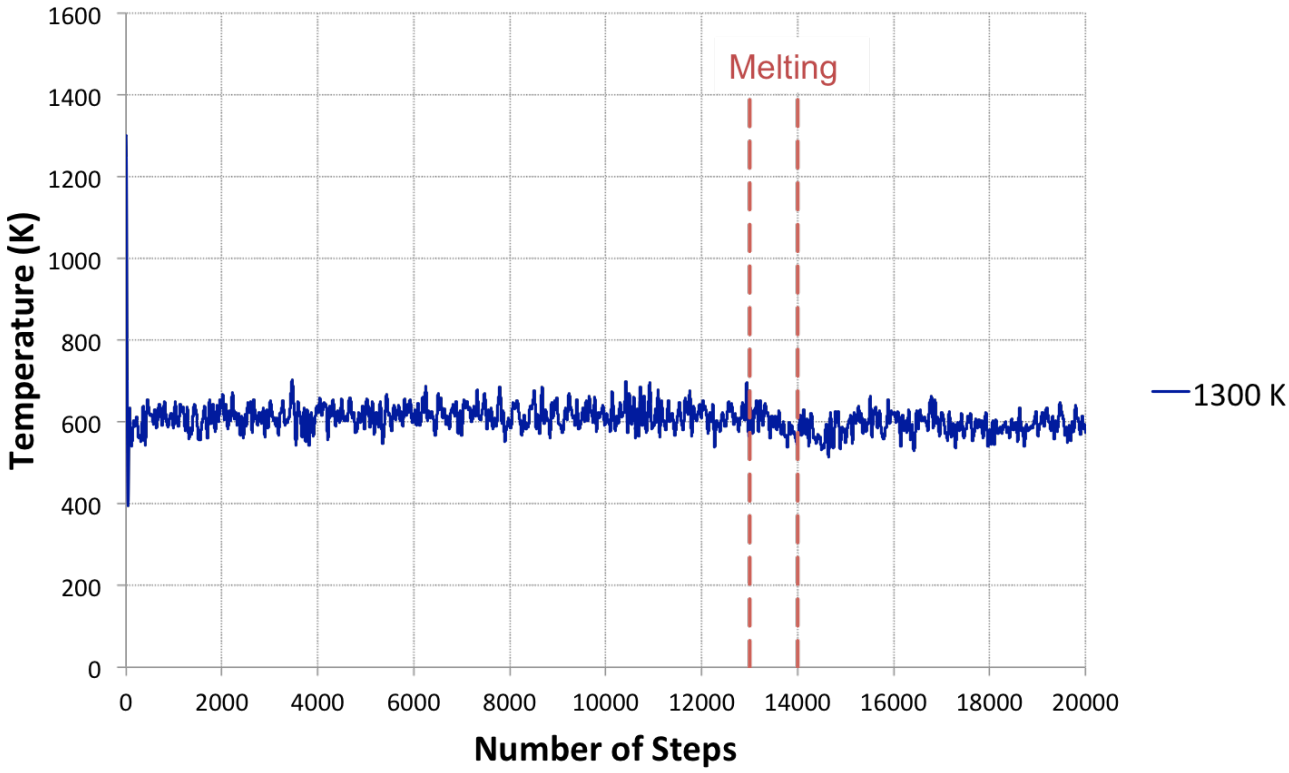

Figure 66: Temperature profile of bcc at 1300 K where a drop is observed thus exhibiting when homogeneous melting occurs

The temperature-pressure graph in Figure 67 was obtained by taking the averages of both the temperatures and pressures for 1000,1300 and 1500 K. At 1300K, the drop in temperature occurs after 13000 steps therefore averages were taken separately, once for the first 13000th steps and once for the last 7000 steps. As shown in Figure 67: $T_m = 591.8$ K at $P = 2.5$ GPa which confirms the Z method does yield an upper bound as the melting temperature at that pressure was experimentally determined to be $T = 480$K [9]. The discrepancy may also be due to the calculations being performed with low convergence parameters and thus further work could include carrying out

corrections to this method.

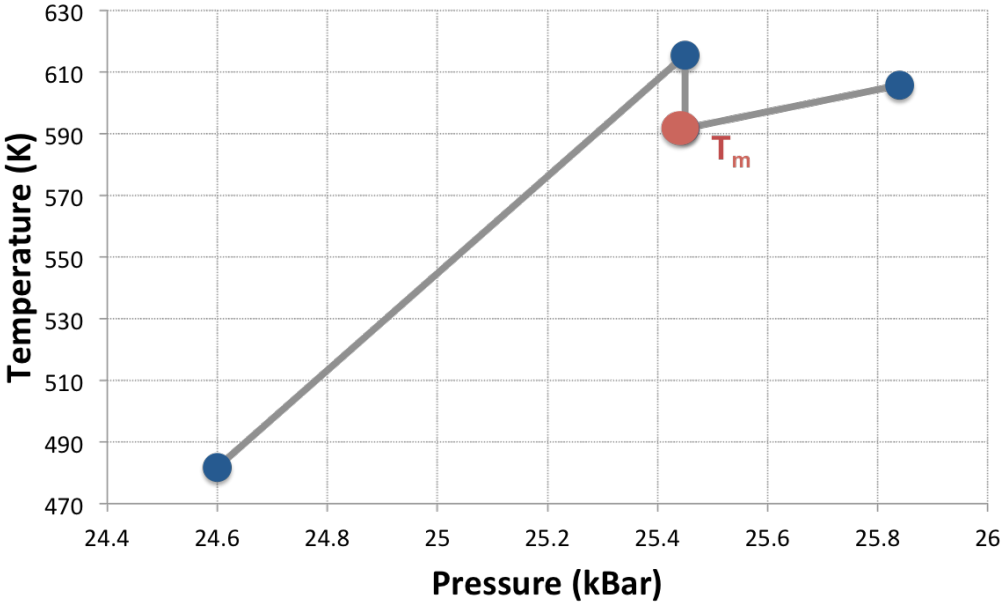

Figure 67: Temperature pressure graph for bcc obtained using the Z method. The first and last points were obtained using the average temperature and pressure of the 1000K and 1500 K runs shown in Figure **??**. The two middle points were obtained using the 1300K run by taking the average temperature and pressure before melting for one point and after melting for another point as shown in Figure **??**

The Z method was also applied to oP8 using a supercell of 256 atoms and a time step of 2 fs. The temperatures tested initially were 500, 1000K, 5000K and 10000K and the simulation times are shown in Table 21. The evolution of temperatures with time steps is shown in Figure 68.

Table 17: Temperatures and simulation times for oP8 using the Z method

Initial Temperature (K)	Simulation Time (ps)
500	14
1000	15
5000	12
10000	20

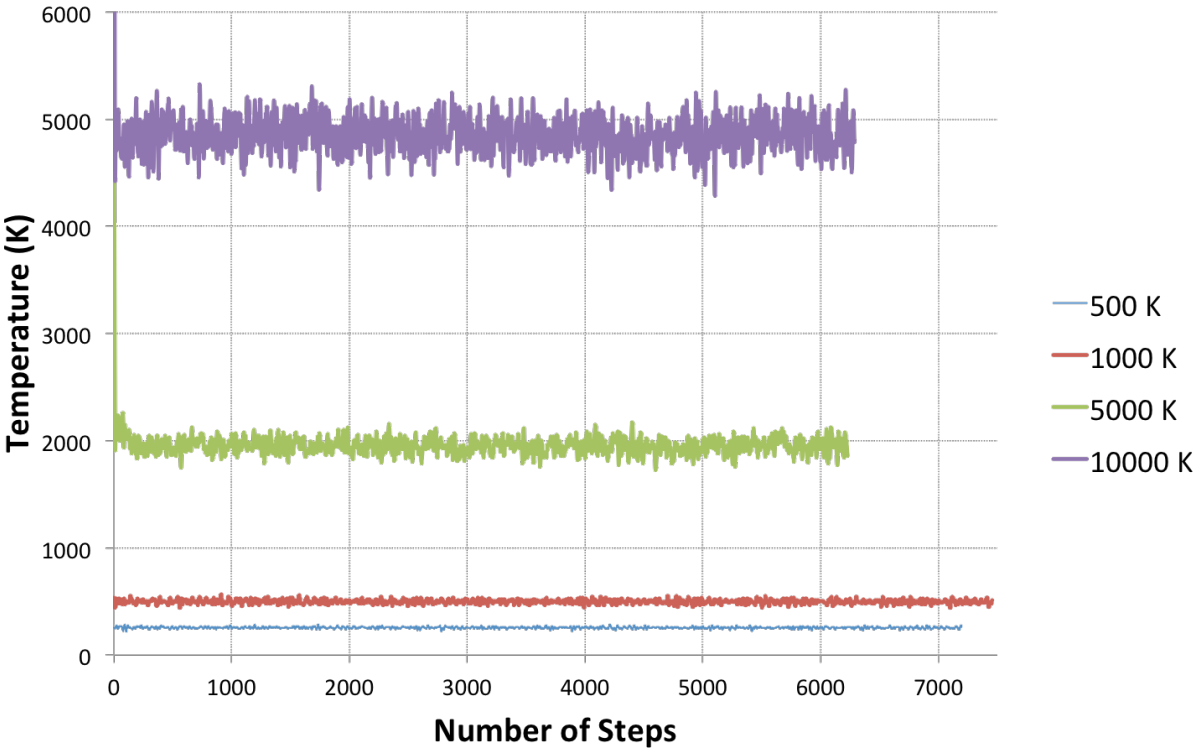

Figure 68: Temperature profiles of Z method runs for oP8 at 500K, 1000K, 5000K and 10000K

Similarly to bcc, at each temperature, both the mean squared displacement

and the diffusion coefficient were used to determine whether the cell was liquid or solid, which shows that at 500K, 1000K and 3000K, the cell is still solid whereas at 5000K and 10000K, it has melted. Consequently, as per Figure 69 the following temperatures, 3500, 4000 and 4500 K were tested for 35, 11, and 12 ps, respectively. The results are shown in Figure 70.

Figure 69: Schematic representation of the trial and error method used for oP8

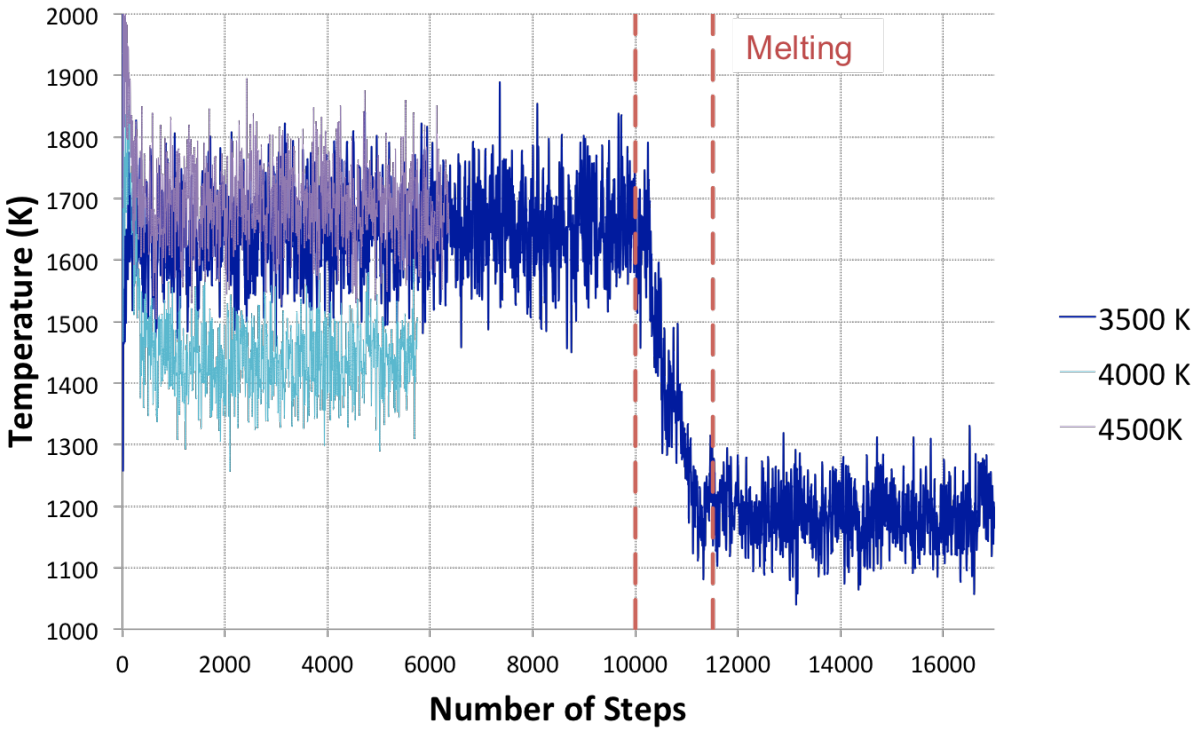

Figure 70: Temperature profiles after Z method runs for oP8 at 4500K, 4000K, 3500K

It is evident from Figure 70 there is a drop in temperature after 10000 steps when the simulation was ran at 3500K. The mean squared displacement and the diffusion coefficient for the first 10000 steps show that the cell is still solid whereas the same parameters for the last steps of the simulation show tthat after the drop the cell is clearly liquid. Hence, the temperature-pressure graph was obtained using the same method as previously explained for bcc and is shown in Figure 71, which shows $T_m = 1294$ K at $P = 60$ GPa

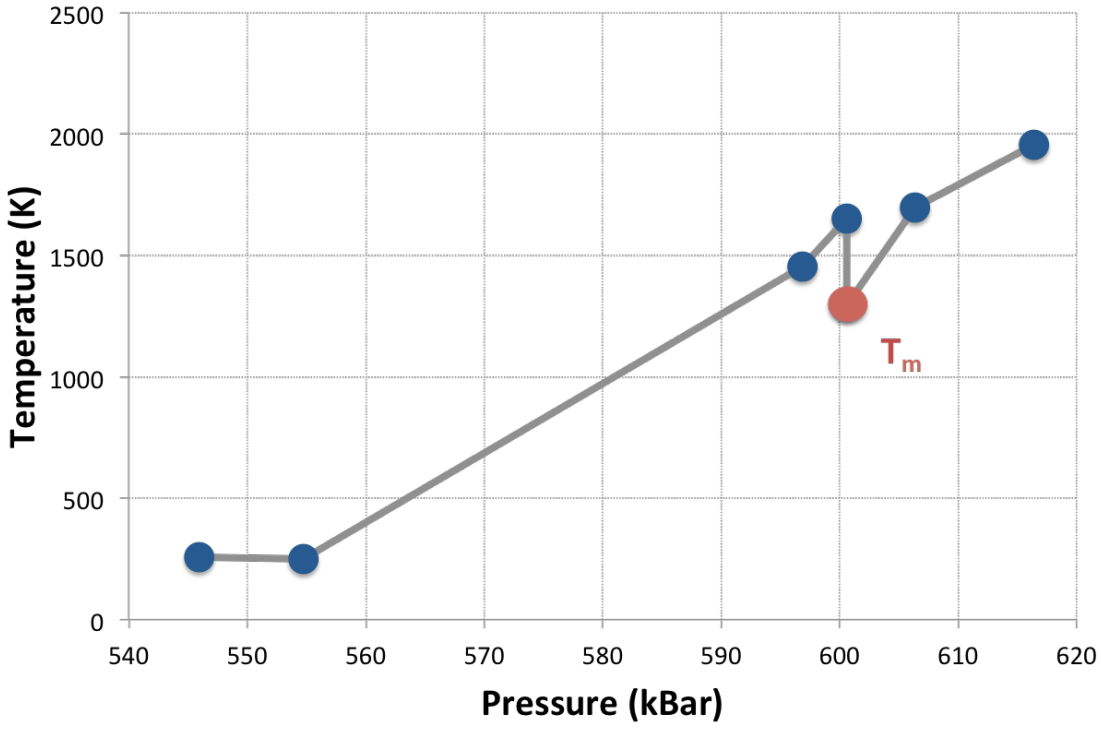

Figure 71: Temperature pressure graph for oP8 obtained using the Z method. This graph was constructed by using the average temperature and pressure of the runs at 500, 1000, 3500, 4000, 4500 and 5000 K as shown in Figures 68 and 70. For the 3500K run where melting is observed the average temperature and pressure were taken before and after melting occurs yielding two different points for this temperature.

6.3.3 Inconclusive results

The Z method was also applied to the other phases of K - fcc, KIIIa, KIIIb and oC16. The number of atoms used were 216 for fcc, 384 for KIIIa, 216 for oC16 and 768 for KIIIb with a time step of 2 fs. Apart for fcc, no previous work was done on the melting of these phases hence the same trial and error method was used as for oP8 and the results are shown in Appendix B. Table 18 shows

the simulation times of all runs.

Table 18: Temperatures and simulation times for fcc, KIII and oC16 using the Z method

Phase	Initial Temperature (K)	Simulation Time (ps)
fcc	800	55
	1000	15
	1100	19
	1200	12
	1300	19
	1500	18
	2500	35
	5000	15
KIIIa	500	6
	750	5.5
	1000	6
	2000	12
	3000	3
KIIIb	100	6.6
	500	6.6
	1000	0.6
	2500	0.6
	5000	1.2
oC16	500	60
	3000	51
	5000	34
	6000	15
	7000	15
	8000	30
	9000	15
	10000	15

Table 19 shows the conclusion drawn from the runs on these phases. Although it was not possible to obtain clear melting temperatures, it was possible

to determine an upper bound or a range of temperatures within which the melting temperature could fall in.

Table 19: Upper bounds of T_m for KIIIa, fcc and oC16

Phase	Number of atoms	Pressure (GPa)	Outcome
KIIIa	384	22	As it is unclear whether the cell is solid or liquid between 500 and 2000 K it is appropriate to expect the upper bound of the melting temperature to be 1000 K
oC16	216	96	at 6000 K the cell is solid whereas at 9000 K it is liquid, therefore the upper bound of the melting temperature should be 4500 K.
fcc	216	15	cell is solid at 1000 K but liquid at 1300 K therefore the upper bound of the melting temperature should be 650 K

6.3.4 Conclusion

Results obtained with the Z method are evidence of its volatility in terms of results. As the theoretical basis for using the Z method has not yet been estab-

lished it therefore proves quite challenging to estimate the importance of each initial parameter (e.g. temperature, number of atoms...) and the impact they will have on finding the melting point. It was also noted from the inconclusive results that some simulations were unclear as the mean square displacement and the diffusion coefficient did not show clearly phase was present, hence the difficulty of identifying the correct temperature at which simulations should be done. Finally, this study concurs with the results shown in [110] which assessed the reliability of the Z method and concluded that it could only provide an upper bound on the melting temperature and finally, that results from the Z method could incur very large errors should the initial conditions not be large enough.

7 Conclusion

The aim of this thesis was to provide an *ab initio* study of the phase diagram of potassium. Previously there had been both theoretical and experimental studies of the first two phases of potassium (bcc and fcc), both on the transition at 0 K and melting of the two phases. The post fcc phases had been observed experimentally but their enthalpies had not been determined due to their incommensurate nature. The three phases post KIIIb were also experimentally observed and their enthalpies were calculated in 2 studies but no high temperature studies were done. A summary of the findings is shown in Figure 72, where the results from the QHA, the coexistence and the Z method are shown.

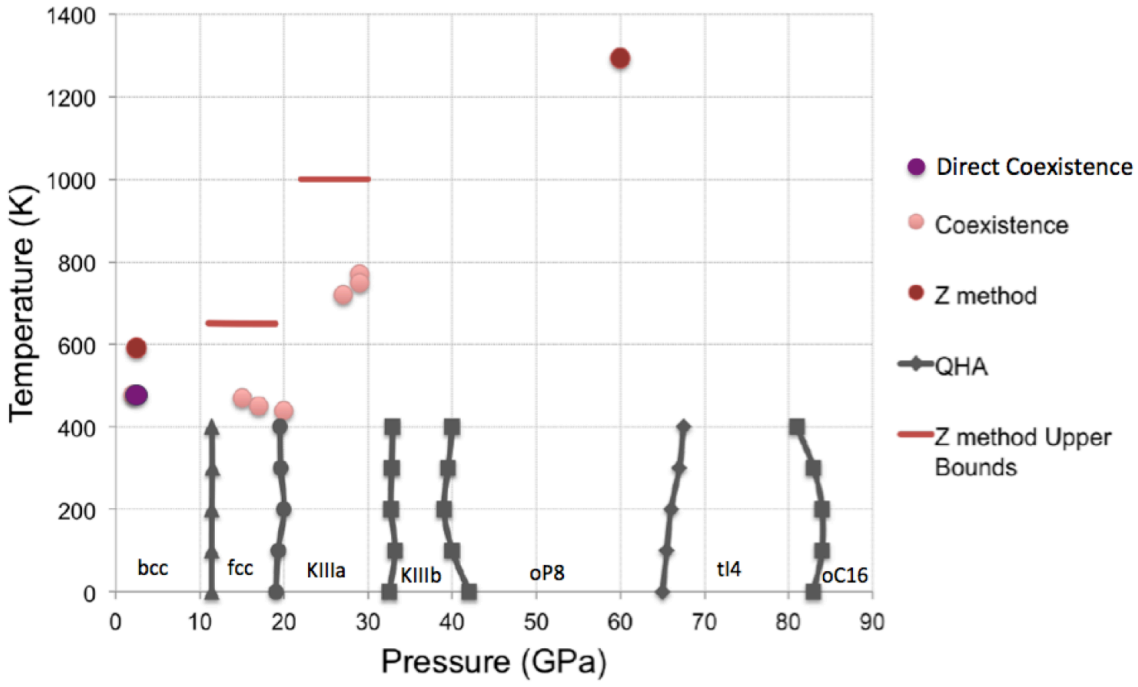

Figure 72: Full phase diagram as determined by findings in this study.

This thesis aimed to provide a full picture as the previous work was incomplete and inconsistencies arose. Static calculations were carried out on bcc and fcc in order to assess the robustness and adequacy of the method used as previous work was readily available for comparison. Results were in good agreement with previous studies which provided a good validation of the method used. Hence the enthalpies of all other phases were calculated. The transitions found at 0 K for KIIIa and KIIIb concured with what was observed experimentally. The enthalpies of oP8, tI4 and oC16 are in excellent agreement with previous calculations, however, experiments differ with those results. Given that there were only 2 experiments carried out it is difficult to determine whether theory or experiments are wrong or if the discrepancy is solely due to theoretical methods not being able to reproduce experimental results. Further work could include experimental work done in parallel with theoretical work to assess this discrepancy. Quasi-harmonic calculations were also carried out on bcc and fcc and once more the results were in accordance with previous studies. Therefore the same method was applied to all phases up to 400 K. The results showed that the quasi-harmonic contribution to the free energy differences between neighbouring phases are negligible. As no similar studies were done before, these results could not be compared. The anaharmonic contribution of all phases were also calculated in this work up to 400 K and it was found that this contribution is negligible. In order to study melting of each phase, the coexistence method using a potential was employed. Results on bcc were in excellent agreement with previous work, however, the use a potential was compromised as other phases did not present a good fit. Therefore the direct coexistence was tested, which although it proved successful proved to be too expensive computationally. Finally, the Z method was used

to determine the melting temperature of each phase, but given the unreliability and unpredictability of the method, only upper bounds to the melting temperatures were determined. Further work could use these upper bounds as starting points to determine melting using more reliable methods such as coexistence.

This study can contribute to three areas. First, from a pure chemistry standpoint, the phase diagram of K remains to be fully known both from theoretical and experimental studies. Before this study, the enthalpies of KIIIa and KIIIb had not been determined, the solid transitions at finite temperatures had not been studied, the anharmonicity of all phases were not known and melting temperatures were only known for bcc and fcc. This study has provided a study of the enthalpies of KIIIa and KIIIb, the solid transitions at finite temperature and anharmonicity. As for melting, this thesis presents an extensive comparison of three different methods to study the melting of potassium. Further work in chemistry could include new experiments to understand the source of the discrepancies between the theoretical and current experimental enthalpies. This could provide insight into experimental and theoretical shortcomings. These insights could be a benefit for the study of other materials. In order to continue work on the melting of K, the different methods used in this study provides a potential roadmap for further studies. Indeed, it is proposed to use the upper bounds on the melting temperature found using the Z method to conduct direct coexistence calculations and determine the melting temperatures accurately. This will therefore also provide more insights into the Z method which can benefit studies of other elements. Second, this study can be used by AWE in order to benchmarks computational methods and gain more insights into the behaviour of K, which may be used in some form for the preservation of nuclear warheads. Finally, in geophysics, as mentioned in the introduction,

the study of K is one of the components necessary to understand further the energy sources of the liquid outer core and hence the weakening of our magnetic field. The phase diagram of K can therefore be used to understand under which conditions K is stable and its thermodynamics. This can therefore be used to assess the abundance of K in the Earth's core and be of use to study solubility.

A Convergence

A.1 bcc and fcc

Table 20: Convergence calculations for bcc at 0K

	400 eV and 20x20x20 kpts	400 eV and 25x25x25 kpts	800eV and 20x20x20kpts
V_0 (Å^3)	73.4454	73.5266	73.3815
B_0 (GPa)	3.75334	3.72214	3.76886
χ	0.238233	0.233198	0.238858
E_0 (eV)	-1.04718	-1.04696	-1.04696

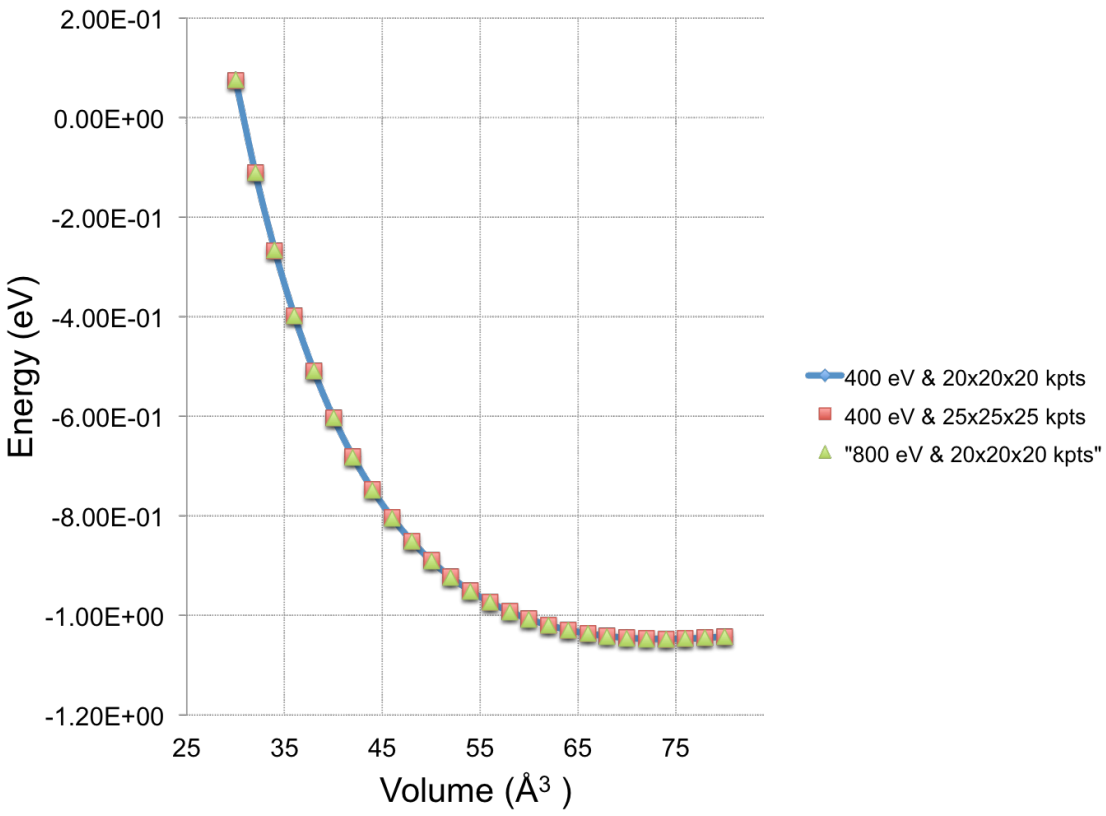

Figure 73: Convergence with respect to planewave cutoff and k-points for bcc

A.2 Host-guest incommensurate phase

Table 21: Temperatures and simulation times for fcc, KIII and oC16 using the Z method

Phase	Volume (Å^3 / atom)	K-Points	Planewave Cutoff (eV)	Energy (eV)
KIIIa	19	2x2x2	400	1.627
	19	4x4x4	400	1.623
	19	2x2x2	600	1.627
	18	2x2x2	400	1.863
	18	4x4x4	400	1.859
	18	2x2x2	600	1.863
	17	2x2x2	400	2.132
	17	4x4x4	400	2.128
	17	2x2x2	600	2.132

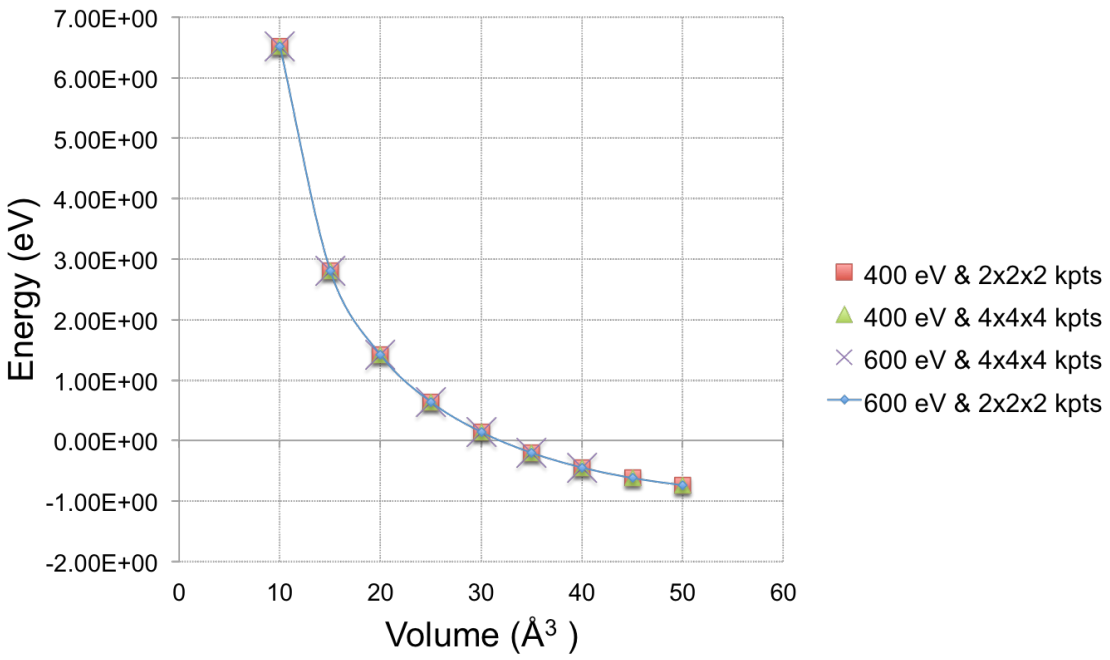

Figure 74: Convergence with respect to planewave cutoff and k-points for KIIIb

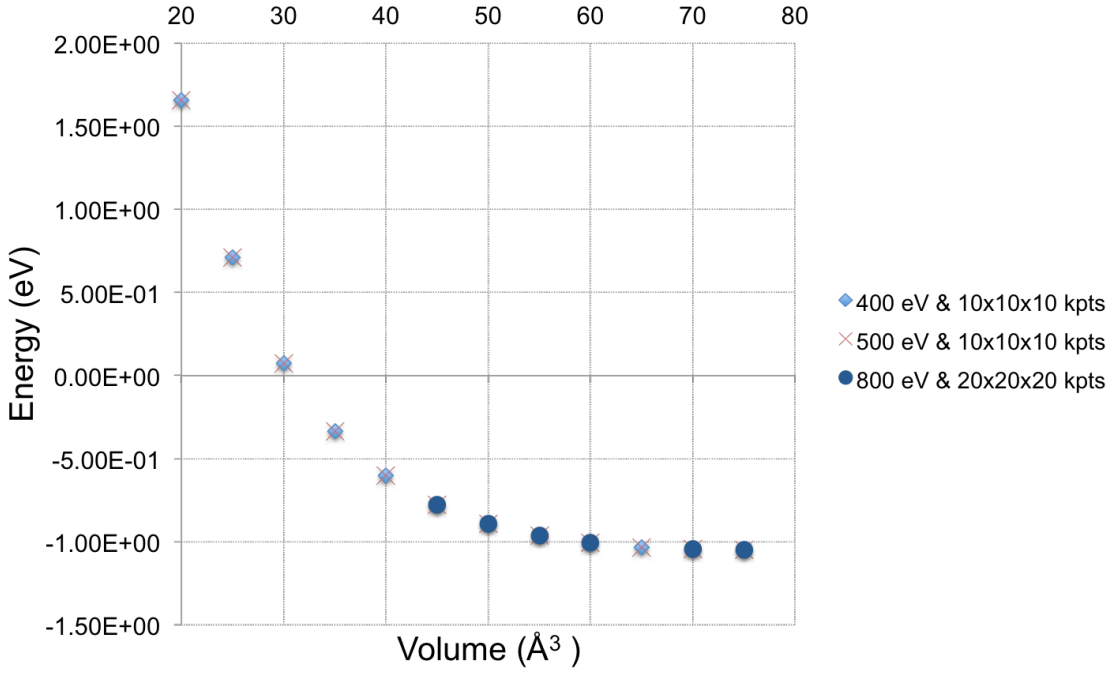

Figure 75: Convergence with respect to planewave cutoff and k-points for cI16

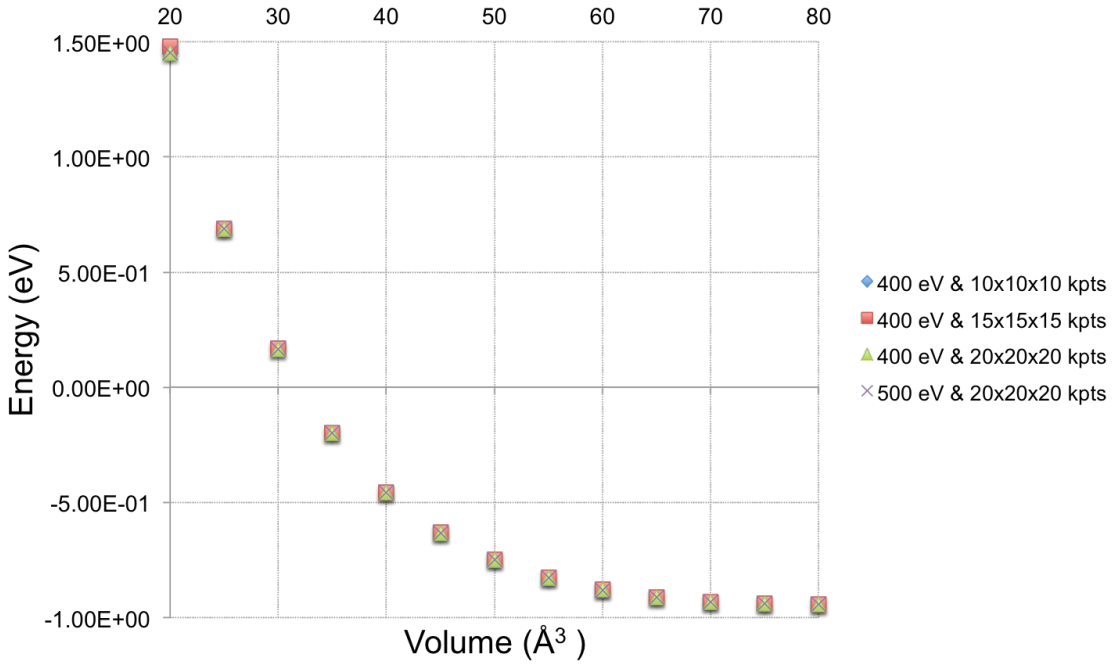

Figure 76: Convergence with respect to planewave cutoff and k-points for sc

A.3 oP8, tI4 and oC16

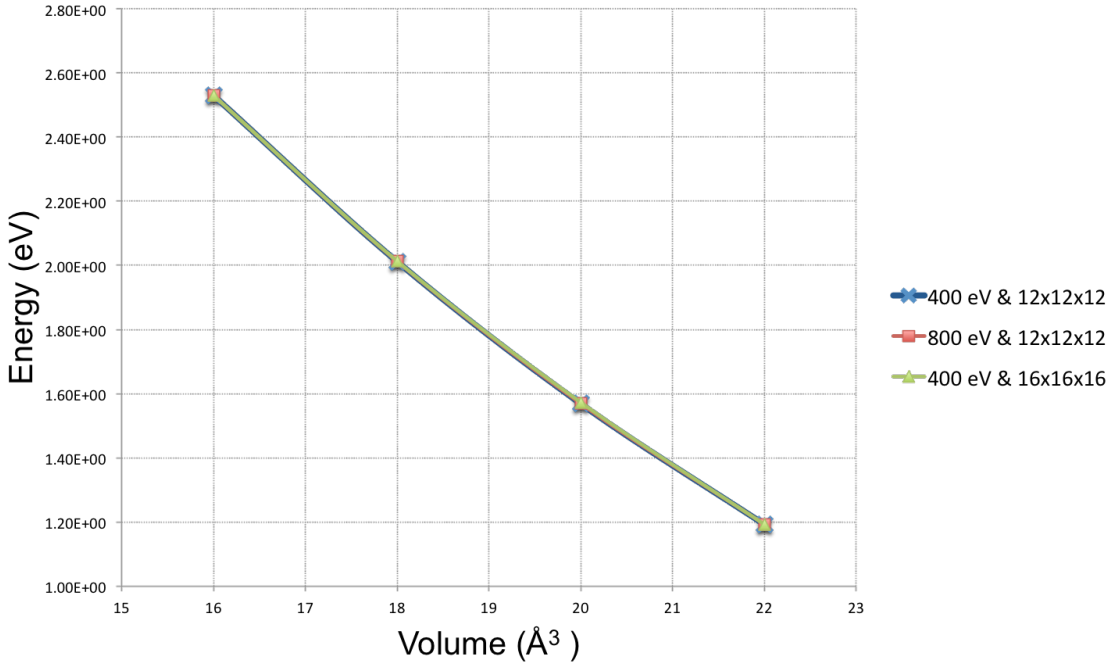

Figure 77: Convergence with respect to planewave cutoff and k-points for oC16

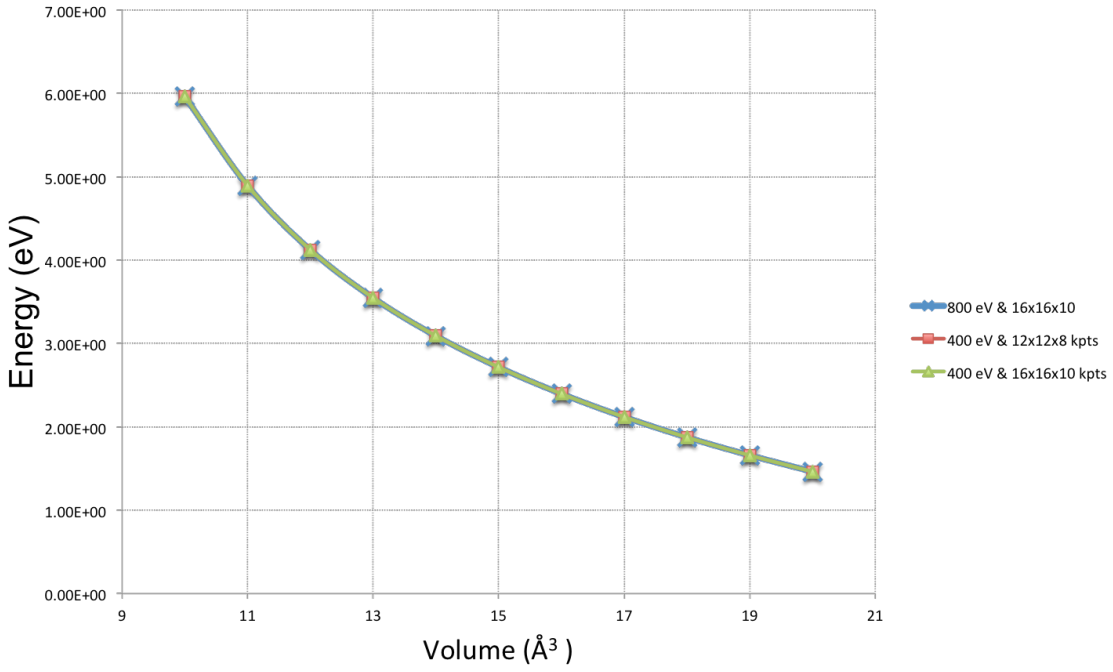

Figure 78: Convergence with respect to planewave cutoff and k-points for tI4

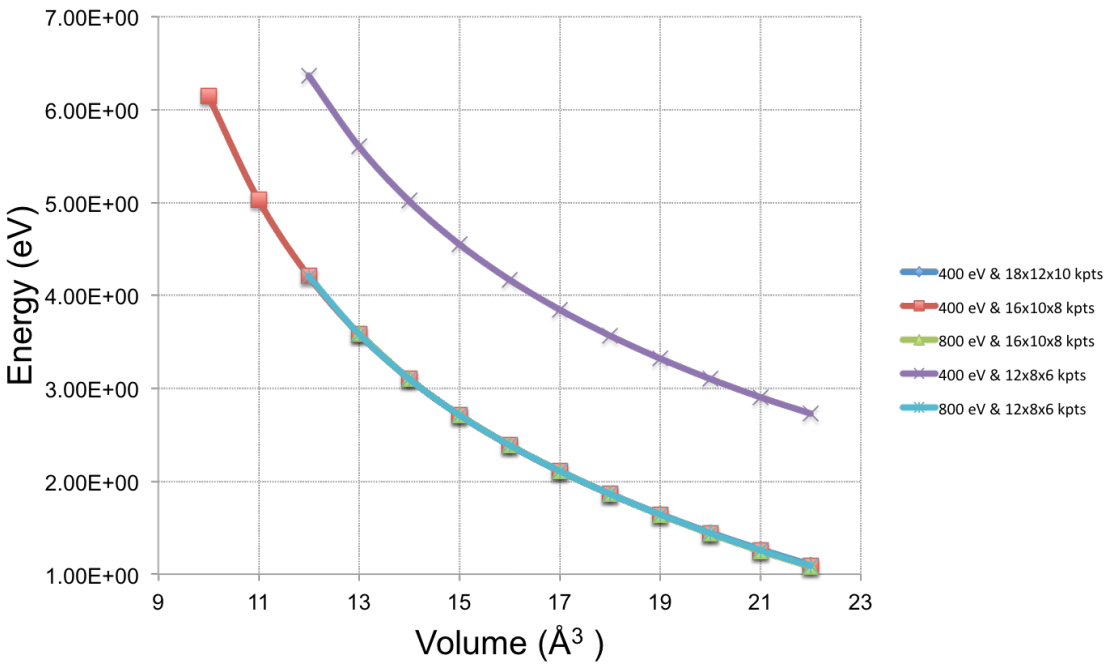

Figure 79: Convergence with respect to planewave cutoff and k-points for oP8

B Z method

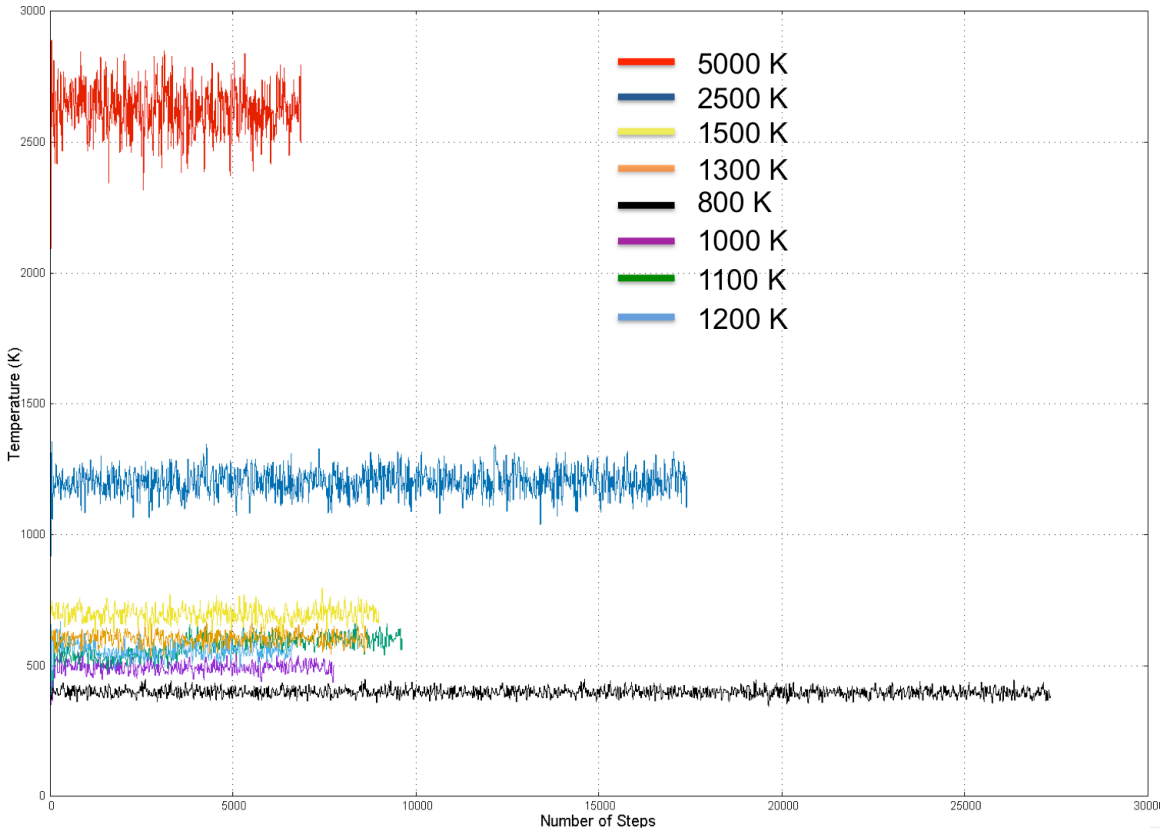

Figure 80: Temperature profiles after Z method runs for fcc at 800, 1000, 1100, 1200, 1300, 1500, 2500 and 5000 K

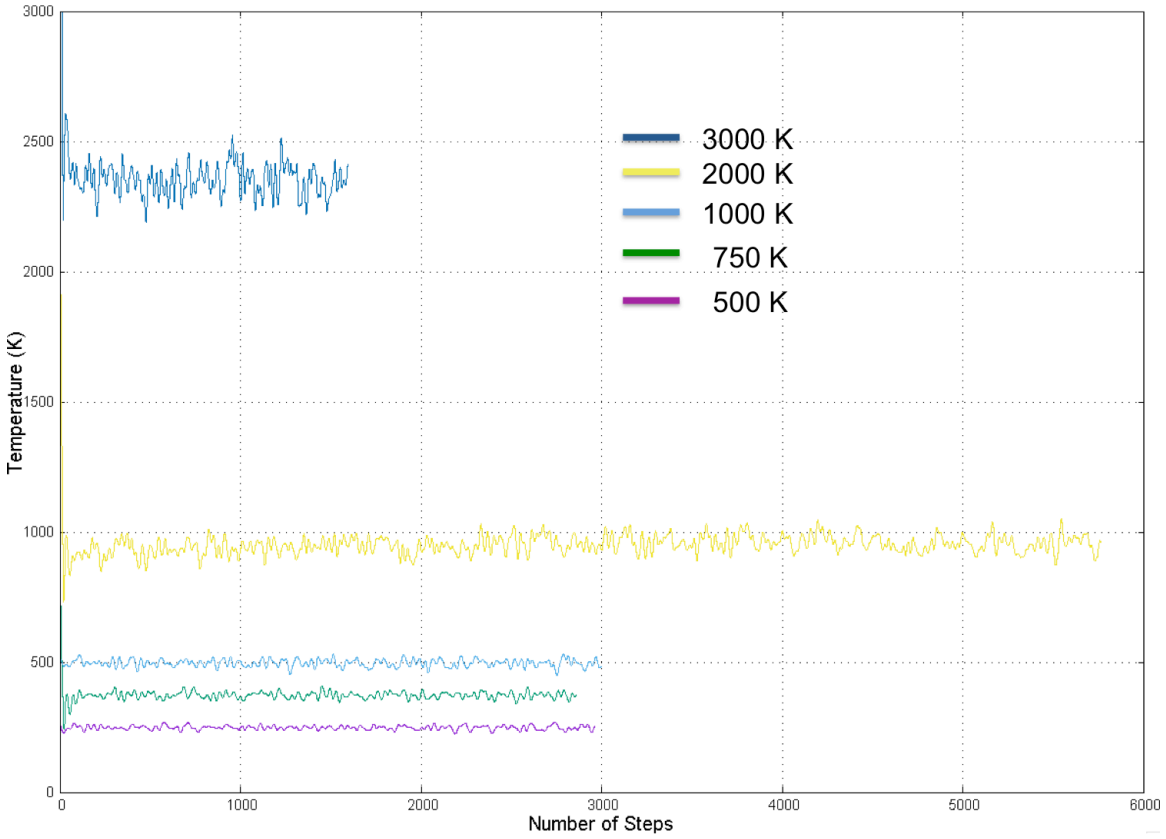

Figure 81: Temperature profiles after Z method runs for KIIIa at 500, 750, 1000, 1500, 2000 and 3000 K

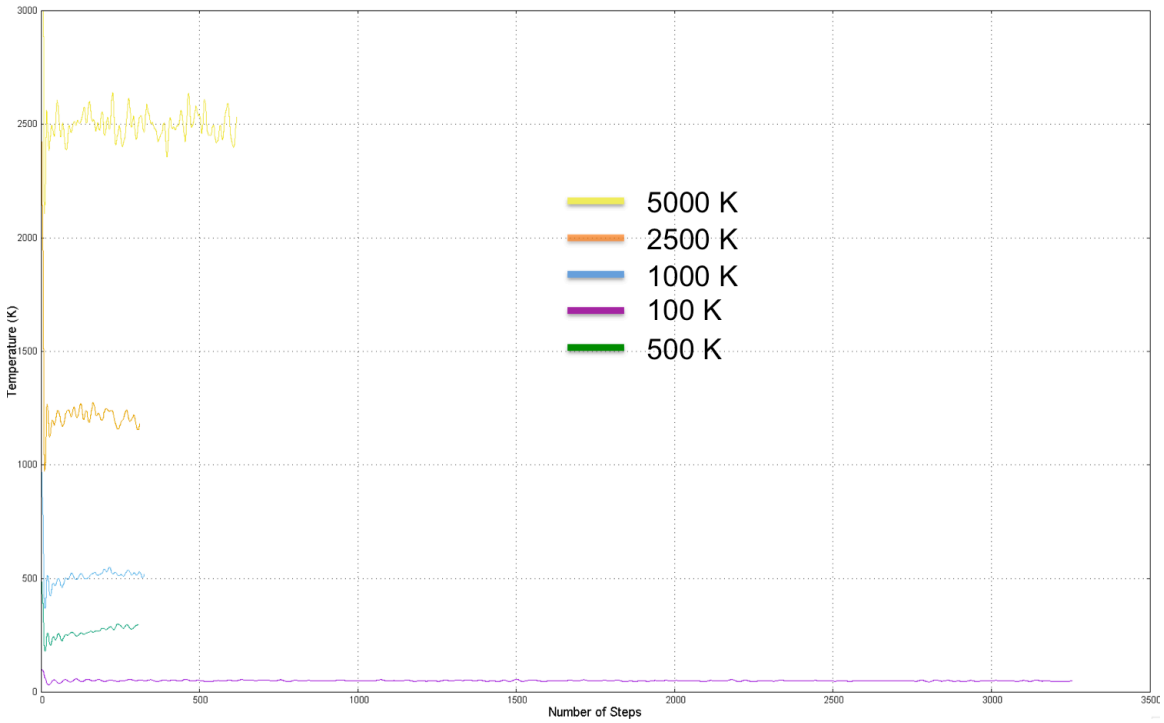

Figure 82: Temperature profiles after Z method runs for KIIIb at 100, 500, 1000, 2500, 5000 K

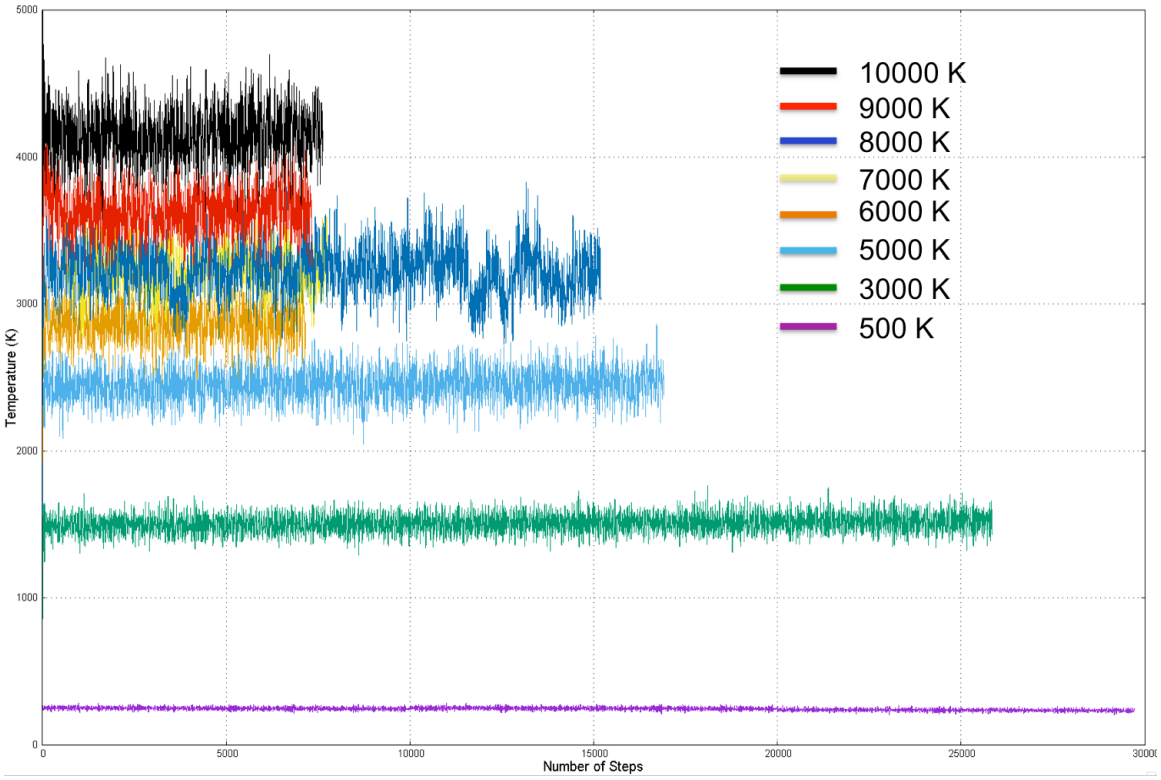

Figure 83: Temperature profiles after Z method runs for oC16 at 500, 3000, 5000, 6000, 7000, 8000, 9000 and 10000 K

References

[1] M Halka and B. Nordstrom. *Alkali and Alkaline Earth Metals*. Facts on File, 2010.

[2] E. Ohtani S. Kamada T. Sakamaki M. Miyahara Y. Ito Watanabe, K. The abundance of potassium in the earth's core. *Phys. Ear. Plan. Int.*, 237, 2014.

[3] K.K.M. Lee, G. Steinle-Neumann, and R. Jeanloz. Ab initio high-pressure alloying of iron and potassium: Implications for the earth's core. *Geoph. Res. Lett.*, 31:L11603, 2004.

[4] G. Steinle-Neumann S. Akber-Knutson Lee, K.K.M. Ab initio predictions of potassium partitioning between fe and al-bearing mgsio3 perovskite and post-perovskite. *Phys. Ear. Plan. Int.*, 174, 2009.

[5] F.S. Ham. Energy bands of alkali metals.ii. fermi surface. *Phys. Rev.*, 128:2524, 1962.

[6] M. I. McMahon, R. J. Nelmes, U. Schwarz, and K. Syassen. Composite incommensurate k-iii and a commensurate form: Study of a high-pressure phase of potassium. *Phys. Rev. B*, 74:140102, 2006.

[7] O. Degtyareva and V.F. Degtyareva. Potassiun under pressure: Electronic origin of complex structures. *Arxiv.org*, 2013.

[8] H. Olijnyk and W.B. Holzapfel. Phase transitions in k and rb under pressure. *Physics Letters A*, 99:381, 1983.

[9] E E McBride, O Narygina, G W Stinton, and M I McMahon. Melting of potassium to 22 gpa. *Journal of Physics: Conference Series*, 377: 012040, 2012.

[10] Markus Winzenick, Viswanalhan Vijayakumar, and Wilfried B. Holzapfel. High-pressure x-ray diffraction on potassium and rubidium up to 50 gpa. *Phys. Rev. B*, 50:12381, 1994.

[11] M.I. McMahon and R. J. Nelmes. High-pressure structures and phase transformations in elemental metals. *Chem. Soc. Rev.*, 35:943, 2006.

[12] Y. Xie, Y. Ma, T. Cui, Y. Li, J. Qiu, and G.T Zou. Origin of bcc to fcc phase transition under pressure in alkali metals. *New Journal of Physics*, 10: 063022, 2008.

[13] Schwarz K Sliwko V L, Mohn P and Blaha P. The fcc-bcc structural transition: I. a band theoretical study for li, k, rb, ca, sr, and the transition metals ti and v. *J. Phys. Condens. Matter*, 8:799, 1996.

[14] J-H. Kang, S-H. Lee, and M-H. Kang. Structural properties of alkali metals (li, na and k) in the generalized gradient approximation. *Journal of the Korean Physical Society*, 33:76, 1998.

[15] M.M. Dacorogna and M.L. Cohen. First-principles study of the structural properties of alkali metals. *Phys. Rev. B*, 34:4996, 1986.

[16] M. Sigalas, N.C. Bacalis, D.A. Papaconstantopoulos, M.J. Mehl, and A.C. Switendick. Total energy calculations of solid h, li, na, k, rb and cs. *Phys. Rev. B*, 42:11637, 1990.

[17] M. I. Katsnelson, G. V. Sinko, N. A. Smirnov, A. V. Trefilov, and K. Yu. Khromov. Structure, elastic moduli, and thermodynamics of sodium and potassium at ultrahigh pressures. *Phys. Rev. B*, 61:14420, 2000.

[18] S. Yu. Savrasov and D. Yu. Savrasov. Full-potential linear-muffin-tin-orbital method for calculating total energies and forces. *Phys. Rev. B*, 46:12181, 1992.

[19] J.P. Perdew, J. A. Chevary, S. H. Vosko, K.A. Jackson, M.R. Pederson, D. J. Singh, and C. Fiolhais. Atoms, molecules, solids, and surfaces: Applications of the generalized gradient approximation for exchange and correlation. *Phys. Rev. B*, 46:6671, 1992.

[20] M. Alouani, N.E. Christensen, and K. Syassen. Calculated ground-state and optical properties of potassium under pressure. *Phys. Rev. B*, 39: 8096, 1989.

[21] P. Hohenberg and W. Kohn. Inhomogeneous electron gas. *Phys. Rev.*, 136:864, 1964.

[22] P.E. Blöchl. Projector augmented-wave method. *Phys. Rev. B*, 50: 17943, 1994.

[23] V.F. Degtyareva. Simple metals at high pressures: the fermi sphere-brillouin zone interaction modeligh pressures: the fermi sphere-brillouin zone interaction model. *Phys - Usp*, 49:369, 2006.

[24] E.C. Bain. The nature of martensite. *Trans. Amer. Inst. Min. Metall. Eng.*, 70:25, 1924.

[25] J. P. Perdew and A. Zunger. Self-interaction correction to density-functional approximations for many-electron systems. *Phys. Rev. B*, 23:5048, 1981.

[26] O.K. Andersen. Linear methods in band theory. *Phys. Rev. B*, 12:3060, 1975.

[27] Yu Xie, John S. Tse, Tian Cui, Artem R. Oganov, Zhi He, Yanming Ma, and Guangtian Zou. Electronic and phonon instabilities in face-centered-cubic alkali metals under pressure studied using ab initio calculations. *Phys. Rev. B*, 75:064102, 2007.

[28] A. Sanna, C. Franchini, A. Floris, G. Profeta, N. N. Lathiotakis, M. Lüders, M. A. L. Marques, E. K. U. Gross, A. Continenza, and S. Massidda. ab initio prediction of pressure-induced superconductivity in potassium. *Phys. Rev. B*, 73:144512, 2006.

[29] M. Lüders, M. A. L. Marques, N. N. Lathiotakis, A. Floris, G. Profeta, L. Fast, A. Continenza, S. Massidda, and E. K. U. Gross. Ab initio theory of superconductivity. i. density functional formalism and approximate functionals. *Phys. Rev. B*, 72:024545, 2005.

[30] L. Shi and D.A. Papaconstantopoulos. Theoretical predictions of superconductivity in alkali metals under high pressure. *Phys. Rev. B*, 73: 184516, 2006.

[31] J.J. Hopfield. Angular momentum and transition-metal superconductivity. *Phys. Rev.*, 186:443, 1969.

[32] W.L. McMillan. Transition temperature of strong-coupled superconductors. *Phys. Rev.*, 167:331, 1968.

[33] O. Degtyareva. Crystal structure of simple metals at high pressure. *High Pressure Research*, 30:343, 2010.

[34] K. Takemura and K. Syassen. High-pressure equation of state of rubidium. *Solid State Commun.*, 44:1161, 1982.

[35] V.F. Degtyareva and I.S. Smirnova. Briz: a vizualization program for the brillouin zone - fermi sphere configuration. *Z. Kristallogr.*, 222:718, 2007.

[36] L. F. Lundegaard, G. W. Stinton, M. Zelazny, C. L. Guillaume, J. E. Proctor, I. Loa, E. Gregoryanz, R. J. Nelmes, and M. I. McMahon. Observation of a reentrant phase transition in incommensurate potassium. *Phys. Rev. B*, 88:054106, 2013.

[37] M. Marques, G. J. Ackland, L. F. Lundegaard, G. Stinton, R. J. Nelmes, M. I. McMahon, and J. Contreras-Garcia. Potassium under pressure: A pseudobinary ionic compound. *Phys. Rev. Lett.*, 103:115501, 2009.

[38] L. F. Lundegaard, M. Marques, G. Stinton, G. J. Ackland, R. J. Nelmes, and M. I. McMahon. Observation of the $op8$ crystal structure in potassium at high pressure. *Phys. Rev. B*, 80:020101, 2009.

[39] G.A. Adebayo. Ab initio calculations of optical properties of li and k at high pressures. *Journal of Physics and Chemistry of Solids*, 74:1221, 2013.

[40] Y. Ma, A.R. Oganov, and Y. Xie. High-pressure structures of lithium, potassium, and rubidium predicted by an *ab initio* evolutionary algorithm. *Phys. Rev. B*, 78:014102, 2008.

[41] A.R. Oganov and W. Glass. Crystal structure prediction using ab initio evolutionary techniques: Principles and applications. *J. Chem. Phys.*, 124:244704, 2006.

[42] A. Lazicki, A.F. Goncharov, V.V. Struzhkin, R.E. Cohen, Z. Liu, E. Gregoryanz, C. Guillaume, H.K. Mao, and R.J. Hemley. Anomalous optical and electronic properties of dense sodium. *Proc. Natl. Acad. Sci. U.S.A*, 106:6525, 2009.

[43] C-S. Zha and R. Boehler. Melting of sodium and potassium in a diamond anvil cell. *Phys. Rev. B*, 31:3199, 1985.

[44] R. Boehler. Melting temperature, adiabats, and grüneisen parameter of lithium, sodium and potassium versus pressure. *Phys. Rev. B*, 27:6754, 1983.

[45] H.D. Luedemann and Kennedy G.C. Melting curves of lithium, sodium, potassium, and rubidium to 80 kilobars. *J. Geophys. Res.*, 73:2795, 1968.

[46] D.A. Young and M. Ross. Theoretical high-pressure equations of state and phase diagrams of the alkali metals. *Phys. Rev. B*, 29:682, 1984.

[47] V V Kechin. Thermodynamically based melting-curve equation. *Journal of Physics: Condensed Matter*, 7(3):531, 1995.

[48] R. Boehler and C-S. Zha. Systematics in the melting behavior of the alkali metals from {DAC} measurements. *Physica B+C*, 139-140:233, 1986.

[49] E. E. McBride, K. A. Munro, G. W. Stinton, R. J. Husband, R. Briggs, H.-P. Liermann, and M. I. McMahon. One-dimensional chain melting in incommensurate potassium. *Phys. Rev. B*, 91:144111, 2015.

[50] Y.P.Varshni. Temperature dependence of the energy gap in semiconductors. *Physica*, 34:149, 1967.

[51] D.K. Belashchenko and D.E. Smirnova. Modeling the molecular dynamics of liquid metals at high pressures: Liquid potassium. *Russ. J. Phys. Chem*, 85:1908, 2011.

[52] D.K. Belashchenko. The use of the embedded atom model for liquid metals: Liquid potassium. *Russ. J. Phys. Chem*, 83:260, 2009.

[53] D. K. Belashchenko. Embedded atom model application to liquid metals: Liquid rubidium. *Russian Journal of Physical Chemistry*, 80:1567--1577, 2006.

[54] Z. Naturforsch J. Rohlin, A. Lodding. Selbstdiffusion in geschmolzenem kaliummetall. *Phys. Sci.*, 17a, 1962.

[55] D. K. Belashchenko and O. I. Ostrovskii. A molecular dynamics study of nickel crystallization at strong supercoolings. *Russ. J. Phys. Chem. A*, 82:364, 2008.

[56] N.I. Gidopoulos J. Kohanoff. *Handbook of Molecular Physics and Quantum Chemistry*. John Wiley and Sons, 2003.

[57] B.J. Berne J. Cao. Born-oppenheimer approximation for path integrals with an application to electron solvation in polarizable fluids. *Journal of Chemical Physics*, 99, 1993.

[58] T. Tsuneda. *Density Functional Theory in Quantum Chemistry*. Springer, 2014.

[59] D.R. Hartree. The wave mechanics of an atom with a non-coulomb central field. *Math. Proc. Cam. Phi. Soc.*, 24, 1928.

[60] V. Fock. Approximation method for the solution of the quantum mechanical multibody problems. *Z. Phys.*, 61, 1930.

[61] M.C. Holthausen W. Koch. *A Chemist's Guide to Density Functional Theory*. Wiley, 2001.

[62] K. Capelle. A bird's eye view of density functional theory. *Brazilian Journal of Physics*, 36, 2006.

[63] W. Kohn and L. J. Sham. Self-consistent equations including exchange and correlation effects. *Phys. Rev.*, 140:A1133--A1138, 1965.

[64] N.D. Mermin. Thermal properties of the inhomogeneous electron gas. *Phys. Rev. A.*, 23, 1965.

[65] Y. Weitao Parr, R.G. *Density-Functional Theory of Atoms and Molecules*. Oxford University Press, 1995.

[66] N.W. Ashcroft and N.D. Mermin. *Solid State Physics*. Saunders College, 1976.

[67] J. Hinze E.S. Sachs. Frozen core approximation, a pseudopotential method tested on six states of nah. *Journal of Chemical Physics*, 62, 1975.

[68] D. R. Hamann, M. Schlüter, and C. Chiang. Norm-conserving pseudopotentials. *Phys. Rev. Lett.*, 43:1494, 1979.

[69] G. Kresse and D. Joubert. From ultrasoft pseudopotentials to the projector augmented-wave method. *Phys. Rev. B*, 59:1758, 1999.

[70] David Vanderbilt. Soft self-consistent pseudopotentials in a generalized eigenvalue formalism. *Phys. Rev. B*, 41:7892--7895, 1990.

[71] J. C. Slater. Wave functions in a periodic potential. *Phys. Rev.*, 51: 846--851, 1937.

[72] P. E. Blöchl. Projector augmented-wave method. *Phys. Rev. B*, 50: 17953, 1994.

[73] K. Burke. The abc of dft. Department of Chemistry, University of California, 2007.

[74] D.M. Ceperley and B.J. Alder. Ground state of the electron gas by stochastic method. *Phys. Rev. Lett. 45, 566*, 1980.

[75] D.G. Truhlar J.L. Bao, L. Gagliardi. Self-interaction error in density functional theory: An appraisal. *J. Phy. Chem. Lett.*, 9, 2018.

[76] J. Dufty S.B. Trickey V.V. Karasiev, T. Sjostrom. Local spin-density approximation exchange-correlation free-energy functional. *Phys. Rev. Lett.*, 112, 2014.

[77] A.D. Becke. Density functional exchange energy approximation with correct asymptotic behaviour. *Phys. Rev. A.*, 38:3098, 1988.

[78] J. P. Perdew, K. Burke, and M. Ernzerhof. Generalized gradient approximation made simple. *Phys. Rev. Lett.*, 77:3865, 1996.

[79] M.A.L. Marques. *A primer in density functional theory*. Springer, 2006.

[80] A. Michaelides J. Klimes, D.R. Bowler. Van der waals density functionals applied to solids. *Phys. Rev. B*, 83, 2011.

[81] Jiří Klimeš, David R Bowler, and Angelos Michaelides. Chemical accuracy for the van der waals density functional. *Journal of Physics: Condensed Matter*, 22(2):022201, 2010.

[82] Hendrik J. Monkhorst and James D. Pack. Special points for brillouin-zone integrations. *Phys. Rev. B*, 13:5188, 1976.

[83] G. Kresse and J. Furthmüller. Efficiency of ab-initio total energy calculations for metals and semiconductors using a plane-wave basis set. *Computational Materials Science*, 6:15, 1996.

[84] Peter E. Blöchl, O. Jepsen, and O. K. Andersen. Improved tetrahedron method for brillouin-zone integrations. *Phys. Rev. B*, 49:16223--16233, 1994.

[85] A.T. Paxton M. Methfessel. High-precision sampling for brillouin zone integration in metals. *Phys. Rev. B*, 40, 1989.

[86] G. Kresse and J. Furthmüller. Efficient iterative schemes for *ab initio*

total-energy calculations using a plane-wave basis set. *Phys. Rev. B*, 54:11169, 1996.

[87] G. Kresse, M.Marsman, and J. Furthmüller. VASP the Guide.

[88] G.J. Ackland. Calculation of free energies from ab initio calculation. *Journ. of Phys. Cond. Matt.*, 14:2975, 2002.

[89] E. Isaev S. Baroni, P. Giannozzi. Thermal properties of materials from ab initio quasi-harmonic phonons. *Reviews in Miner. and Geochem.*, 71, 2009.

[90] D. Alfé. PHON. *Computer Phys. Comm.*, 180:2622, 2009.

[91] K. Parlinski, Z. Q. Li, and Y. Kawazoe. First-principles determination of the soft mode in cubic zro$_2$. *Phys. Rev. Lett.*, 78:4063--4066, 1997.

[92] K. Kunc and Richard M. Martin. Ab initio force constants of gaas. *Phys. Rev. Lett.*, 48:406--409, Feb 1982.

[93] R.P. Feynman. Forces in molecules. *Phys. Rev.*, 56, 1939.

[94] G.D. Price D Alfè and M.J. Gillan. Thermodynamics of hexagonal-close-packed iron under earth's core conditions. *Phys. Rev. B*, 64:045123, 2001.

[95] R. D. Skeel. What makes molecular dynamics work? *J. Sci. Comput.*, 31, 2009.

[96] L. Verlet. Computer experiments on classical fluids. *Phys. Rev.*, 159, 1967.

[97] H.C. Andersen. Molecular dynamics simulations at constant pressure and/or temperature. *Journal of Chemical Physics*, 72, 1980.

[98] D Alfè, L Vočadlo, G D Price, and M J Gillan. Melting curve of materials: theory versus experiments. *Journal of Physics: Condensed Matter*, 16: S973, 2004.

[99] Daan Frenkel and Berend Smit. *Understanding Molecular Simulation*. Academic Press, Inc., Orlando, FL, USA, 2nd edition, 2001. ISBN 0122673514.

[100] D. Alfè J. Brodholt L. Vočadlo M, J. Gillan and G.D. Price. First-principles modelling of earth and planetary materials at high pressures and temperatures. *Rep. Prog. Phys.*, 69:2365, 2006.

[101] D. Alfè. Melting Curve of MgO from First-Principles Simulations. *Physical Review Letters*, 94:235701, 2005.

[102] Murray S. Daw, Stephen M. Foiles, and Michael I. Baskes. The embedded-atom method: a review of theory and applications. *Materials Science Reports*, 9(7):251 -- 310, 1993.

[103] Frank H. Stillinger and Thomas A. Weber. Computer simulation of local order in condensed phases of silicon. *Phys. Rev. B*, 31:5262--5271, 1985.

[104] S. Taioli C. Cazorla, M.J. Gillan and D. Alfè. Ab initio melting curve of molybdenum by the phase coexistence method. *J. Chem. Phys.*, 126 (194502), 2007.

[105] M.J. Gillan D. Alfè and G.D Price. Complementary approaches to the ab initio calculation of melting properties. *Journal of Chemical Physics*, 116(14), 2002.

[106] G.D. Price L. Vocadlo, D. Alfè and M.J. Gillan. Ab initio melting curve of copper by the phase coexistence approach. *J. Chem. Phys.*, 120:2872, 2004.

[107] A. B. Belonoshko, L. Burakovsky, S. P. Chen, B. Johansson, A. S. Mikhaylushkin, D. L. Preston, S. I. Simak, and D. C. Swift. Molybdenum at high pressure and temperature: Melting from another solid phase. *Phys. Rev. Lett.*, 100:135701, Apr 2008.

[108] F. Gonzalez-Cataldo, S. Davis, and G. Gutierrez. Z method calculations to determine the melting curve of silica at high pressures. *Journal of Physics: Conference Series*, 720:012032, 2016.

[109] D. Li, P. Zhang, and J. Yan. Quantum molecular dynamics simulations of lithium mlting using z-method. *Arxiv.org*, 2010.

[110] C. Cazorla Alfè D. and M.J. Gillan. The kinetics of homogeneous melting beyond the limit of superheating. *The Journal of Chemical Physics*, 135: 024102, 2011.

[111] K. Takemura and K. Syassen. High-pressure phase transitions in potassium and phase relations among heavy alkali metals. *Phys. Rev. B*, 28: 1193, 1983.

[112] Yanming Ma, Mikhail Eremets, Artem R. Oganov, Yu Xie, Ivan Tro-

jan, Sergey Medvedev, Andriy O. Lyakhov, Mario Valle, and Vitali Prakapenka. Transparent dense sodium. *Nature*, 458:182--185, 2009.

[113] Chris J. Pickard and R. J. Needs. Predicted pressure-induced s-band ferromagnetism in alkali metals. *Phys. Rev. Lett.*, 107, 2011.

[114] R. A. Cowley, A. D. B. Woods, and G. Dolling. Crystal dynamics of potassium. i. pseudopotential analysis of phonon dispersion curves at 9°k. *Phys. Rev.*, 150:487, 1966.

[115] G. Fabbris, J. Lim, L. S. I. Veiga, D. Haskel, and J. S. Schilling. Electronic and structural ground state of heavy alkali metals at high pressure. *Phys. Rev. B*, 91, 2015.

[116] H. Flyvbjerg and H.G. Petersen. Error estimates on averages of correlated data. *J. Chem. Phys.*, 91, 1989.

[117] Chang-Sheng Zha and Reinhard Boehler. Melting of sodium and potassium in a diamond anvil cell. *Phys. Rev. B*, 31:3199, 1985.

[118] A.B. Belonoshko and A. Rosengren. High-pressure melting curve of platinum from ab initio z method. *Phys. Rev. B*, 85:174104, 2012.

[119] A. Zaoui B. K. Benazzouz and A. B. Belonoshko. Determination of the melting temperature of kaolinite by means of the z-method. *American Mineralogist*, 98:1181, 2013.

[120] D.L. Preston L. Burakovsky, S.P. Chen and D.G. Sheppard. Z methodology for phase diagram studies: platinum and tantalum as examples. *Journal of Physics*, 500:162001, 2014.